DISSERTATIONES
CHIMICAE
UNIVERSITATIS
TARTUENSIS
238

KENNETH TUUL

Evaluating lithium-ion pouch cells and hydrogen storage materials under extreme conditions using advanced techniques

DISSERTATIONES CHIMICAE UNIVERSITATIS TARTUENSIS
238

DISSERTATIONES CHIMICAE UNIVERSITATIS TARTUENSIS
238

KENNETH TUUL

Evaluating lithium-ion pouch cells and hydrogen storage materials under extreme conditions using advanced techniques

UNIVERSITY OF TARTU
Press
1632

Institute of Chemistry, Faculty of Science and Technology, University of Tartu, Estonia

The dissertation was accepted for the commencement of the degree of Doctor of Philosophy in Chemistry on June 10th, 2025, by the Council of the Institute of Chemistry, University of Tartu.

Supervisors: Associate Professor Rasmus Palm, PhD
University of Tartu, Estonia

Professor Enn Lust, PhD
University of Tartu, Estonia

Professor Emeritus Jeff R. Dahn, PhD
Dalhousie University, Canada

Opponent: Associate Professor Johannes Wandt, PhD
University of Agder, Norway

Commencement: August 26th, 2025, at 14:15
Ravila 14A-1020, Tartu (Chemicum) and Microsoft Teams

REPUBLIC OF ESTONIA
MINISTRY OF EDUCATION
AND RESEARCH

Natural Sciences and Engineering
Research Council of Canada

Conseil de recherches en sciences
naturelles et en génie du Canada

Canada

ISSN 1406-0299 (print)
ISBN 978-9916-27-921-2 (print)

ISSN 2806-2159 (pdf)
ISBN 978-9916-27-922-9 (pdf)

University of Tartu Press
www.tyk.ee

Dedicated to Svante Arrhenius for his contributions
to the study of reaction kinetics and physical chemistry
that are essential to the topics in this thesis.

TABLE OF CONTENTS

1. LIST OF ORIGINAL PUBLICATIONS

The thesis consists of seven original publications listed below. They are referred to in the text using Roman numerals I–VI.

I **K. Tuul**, R. Palm, Influence of Nanoconfinement on the Hydrogen Release Processes from Sodium Alanate, Reactions 2 (2021) 1–9. https://doi.org/10.3390/reactions2010001.

II R. Palm, **K. Tuul**, F. Elson, E. Nocerino, O.K. Forslund, T.C. Hansen, J. Aruväli, M. Månsson, In situ neutron diffraction of $NaAlD_4$/carbon black composites during decomposition/deuteration cycles and the effect of carbon on phase segregation, International Journal of Hydrogen Energy 47 (2022) 34195–34204. https://doi.org/10.1016/j.ijhydene.2022.08.019.

III **K. Tuul**, R. Palm, J. Aruväli, E. Lust, Dehydrogenation and low-pressure hydrogenation properties of $NaAlH_4$ confined in mesoporous carbon black for hydrogen storage, International Journal of Hydrogen Energy 48 (2023) 19646–19656. https://doi.org/10.1016/j.ijhydene.2023.01.358.

IV **K. Tuul**, S. Martin Maher, C. Floras, W. Black, T. Taskovic, S. Chisholm, A. Clarke, E. Lust, J.R. Dahn, Exceptional Performance of Li-ion Battery Cells with Liquid Electrolyte at 100 °C, J. Electrochem. Soc. 171 (2024) 040510. https://doi.org/10.1149/1945-7111/ad36e7.

V **K. Tuul**, W. Black, C. Floras, T. Taskovic, S. Martin Maher, A. Adamson, J. Harlow, M.B. Johnson, D. Rathore, S. Chisholm, S. Azam, R. Palm, J.R. Dahn, Limitations of Li-Ion Pouch Cells for Accelerated Testing and Long-Lifetime Cells, J. Electrochem. Soc. 172 (2025) 020519. https://doi.org/10.1149/1945-7111/adb217.

VI **K. Tuul**, T. Taskovic, S. Martin Maher, C. Floras, M. Tulloch, R. Palm, J.R. Dahn, Cell Chemistry Considerations for Long-Lived Li-Ion Cells at High Temperatures. Manuscript.

Author's contribution:

Publication I: Formal analysis, writing – review & editing

Publication II: Methodology, validation, formal analysis, investigation, writing – review & editing

Publication III: Conceptualization, methodology, validation, formal analysis, investigation, writing – original draft, writing – review & editing, visualization

Publication IV: Conceptualization, methodology, formal analysis, investigation, writing – original draft, writing – review & editing, visualization

Publication V: Formal analysis, investigation, writing – original draft, writing – review & editing, visualization

Publication VI: Conceptualization, formal analysis, investigation, writing – original draft, writing – review & editing, visualization

2. ABBREVIATIONS AND SYMBOLS

μXRF – micro X-ray fluorescence spectrometry

A – Li-ion battery degradation rate, also known as the proportionality constant

AG – artificial graphite

AGA – artificial graphite A

AGC – artificial graphite B

BET – Brunauer-Emmett-Teller (theory of gas adsorption)

CCCV – constant current, constant voltage

CE – coulombic efficiency

CIE – coulombic inefficiency (1 – CE)

DEC – diethyl carbonate

Delta V – voltage hysteresis

DMC – dimethyl carbonate

DMOHC – dimethyl-2,5-dioxahexane carboxylate (dimethyl 2,5-dioxahexanedioate)

DTD – ethylene sulfate (1,3,2-dioxathiolane 2,2-dioxide)

E_a – activation energy

EC – ethylene carbonate

EMC – ethyl methyl carbonate

EV – electric vehicle

f – discharge capacity fade

GoF – goodness of fit

LFP – $LiFePO_4$

LiFSI - lithium bis(fluorosulfonyl)imide

LiTFSI - lithium bis(trifluoromethanesulfonyl)imide

n – amount of substance in moles

NCxx – ball-milled $NaAlH_4$ and carbon black composite with "xx" wt% of $NaAlH_4$, e.g., NC60 is a $NaAlH_4$/carbon black composite with 60 wt% of $NaAlH_4$

NMC - $LiNi_xMn_yCo_{1-x-y}O_2$ positive electrode material

NPD – neutron powder diffraction

occ_D – deuterium isotope occupancy

occ_H – hydrogen isotope occupancy
p – the equilibrium pressure of the adsorbate gas
p/p_0 – relative pressure
p_0 – the saturation vapor pressure of the adsorbate gas

p_{D2} – deuterium pressure

PES – prop-1-ene-1,3-sultone

$p_{H2,dehydro}$ – hydrogen pressure during dehydrogenation

$p_{H2,hydro}$ - hydrogen pressure during hydrogenation

PXRD – powder X-ray diffraction

$Q(t)$ – capacity at time t

Q_0 – initial capacity

Q_c – charge capacity

Q_d – discharge capacity

R – universal gas constant

S_{BET} – specific surface area determined via the BET theory

SC – single crystal

SEI – solid-electrolyte interphase

T – temperature

t – time

$t_{dehydro}$ – dehydrogenation time

$T_{dehydro}$ – temperature of dehydrogenation

THF – tetrahydrofuran

T_{hydro} – temperature of hydrogenation

t_{hydro} – time of hydrogenation

T_{max} – temperature of maximum H_2 release

TPD – temperature-programmed dehydrogenation

TTSPi – tris(trimethylsilyl) phosphite

UCV – upper cut-off voltage

UHPC – ultra-high precision coulometry

VC – vinylene carbonate

V_{tot} – total pore volume

β – temperature ramp rate

Δc – charge endpoint capacity slippage

Δd – discharge endpoint capacity slippage

$\Delta m_{\text{balance}}$ – in an *ex-situ* gas volume measurement, it is the difference between the mass measurement before and after cycling

ΔT – temperature ramp rate

ΔV – voltage hysteresis

ΔVol – change in volume of a pouch cell due to gas evolution

ρ_{water} – density of deionized water at 20 °C (0.998 g mL^{-1})

γ – Arrhenius equation pre-exponential factor, also known as the frequency factor

3. INTRODUCTION

Since 2022, the Russian invasion of Ukraine and the instability of the global energy market, combined with the intense growth of energy demand, have created an impetus for further energy independence and renewable energy solutions. In the EU, this has given rise to the REPowerEU plan to eliminate dependence on natural gas from Russia before 2030. This is in addition to the Fit for 55 package, which is the implementation network for the EU Green Deal.[1] Fit for 55 aims to reduce greenhouse gas emissions by 55% by 2030, reaching full climate neutrality by 2050.[2] Reliable, scalable, and efficient energy storage solutions are necessary to integrate the rising shares of renewables. They balance supply and demand daily and seasonally, enable peak shaving, back-up energy storage, and the use of renewable energy for mobile solutions.[1]

Battery manufacturing is set to increase four to six times from current levels by 2030.[1] Li-ion batteries dominate the energy storage market due to their high energy density, efficiency, and technological and supply chain maturity. They exhibit rapid response times and high cycling capabilities while remaining easy to recharge and portable.[3–5] However, they are not considered suitable for long-duration energy storage due to the self-discharge and the amounts of energy required. Hydrogen is considered more suitable for long-duration and seasonal energy storage.[5–7] Li-ion batteries also face increasing concerns around raw material availability, sustainability, and ethical sourcing. The supply chain for critical inputs like lithium, cobalt, and nickel is concentrated in a few countries, raising concerns about environmental and social impacts.[8,9] Moreover, their degradation over time, especially under extreme conditions and demanding cycling, limits their operational lifespan. Limited lifespans result in production being directed towards the replacement of existing energy storage capacity rather than increasing it. Thus, research addressing longevity and recyclability is critical.[10]

The Fit for 55 package aims to shift from fossil natural gas to renewable and low-carbon gases, including hydrogen.[11] There are many funding schemes to support the transition to green energy and support regions that are affected by it, such as the Just Transition Fund.[12] In terms of energy storage, the electrolysis of water during renewable energy overproduction is another way of balancing the grid. Hydrogen is a flexible energy source that can provide multiple services in both power supply and industrial processes.[13] It is beneficial for long-duration and seasonal storage. Its ability to store large amounts of energy over extended periods makes it valuable for addressing the variability of renewable energy and improving grid flexibility. Industrial uses include fertilizer production, other chemical industries, and metallurgy. Thus, the electrolytic production of hydrogen using renewables and subsequent storage allows for saving excess renewable energy for later use, which is critical to decarbonize hard-to-abate sectors.[14] Although hydrogen storage can supplement increased storage capacity, it faces significant issues relating to efficiency, safety, and cost. Current H_2 storage technologies involve liquefaction and high-pressure compression, which have

low round-trip efficiencies and low volumetric energy densities and require cryogenic liquids or dangerously high pressures. Hydrogen embrittlement is also a major issue. This means novel hydrogen storage materials, such as hydrides or adsorbents, are necessary.[15] All things considered, a combination of batteries and hydrogen storage is necessary to cover all the aspects of integrating renewable energy, exemplified by Toshiba's H_2One™ hydrogen-based autonomous energy supply system. The latter combines a Li-ion battery, electrolyzer, hydrogen storage tank, and fuel cell all in one system.[16,17] Therefore, research and development in both fields are critical.

This thesis is composed of seven publications that fall into two distinct topics.

1. Synthesizing a complex metal hydride-based hydrogen storage material, characterizing it, and preparing it for and studying it by *in-situ* neutron diffraction (I–III). The goal was to lower the required operating pressures and temperatures and understand the mechanisms and limitations of the H_2 storage system.
2. Developing a Li-ion pouch cell with liquid electrolyte that is operable in a wide temperature range and especially at highly elevated temperatures (≤ 100 °C) for the creation of a lifetime estimating model for long-lifetime cells (IV–VI).

In addition to featuring energy storage materials, the overarching themes for both topics are the extreme environmental conditions involved and the use of advanced characterization methods. The extreme conditions entail high temperatures (60–100 °C) for Li-ion batteries and high temperatures and high pressures (≤ 190 °C, ≤ 160 bar) for hydrogen storage materials. The advanced methods used involve *in-situ* neutron powder diffraction for hydrogen storage materials and ultra-high precision coulometry combined with accelerated elevated temperature testing for Li-ion batteries. Though these methods have specific requirements for instrumentation and may be expensive, as when using a neutron source, they are founded in direct analysis of experimental data, rather than modelling. There is considerable information retrieved directly from the measurement that enables the determination of the processes and mechanisms guiding the investigated systems, which allows for further improvement of the systems towards higher efficiency and longer lifetime.

Under the topic of hydrogen storage, the effects of nanostructuring sodium alanate ($NaAlH_4$) are discussed (I), followed by the synthesis and laboratory characterization of a $NaAlH_4$/carbon black composite material (III), which is finally prepared and studied *in situ* via neutron powder diffraction (II). The aim of these studies was to lower the operating temperature and pressure using a mesoporous carbon material. Lower operating temperatures and pressures would make the hydrogen storage system more viable for commercial applications. For this, insight into what goes on during dehydrogenation/hydrogenation cycling was gathered specifically thanks to *in-situ* neutron diffraction.

The topic of Li-ion batteries discusses the optimization of the positive electrode material, electrolyte salt, solvents, and additives (IV, VI) to enable cells that could be cycled for extended periods at temperatures up to 100 °C (IV). Combining ultra-high precision coulometry data from a wide temperature range

with accelerated cycling testing allows the development of a lifetime model that could predict Li-ion cell lifetimes into decades (IV). Limitations of the pouch cell format used for the development of these cells and advantages of the metal cylindrical cell format for long-lifetime cells are also presented (V).

This thesis aims to demonstrate how these advanced, yet straightforward, characterization methods can be powerful tools in the successful development of energy storage materials, specifically in the development of long-lifetime Li-ion cells and effective hydrogen storage materials.

4. LITERATURE OVERVIEW

4.1. Hydrogen storage

4.1.1. Sodium aluminium hydride ($NaAlH_4$) for solid state H_2 storage

Hydrogen (H_2) is a clean energy carrier that can be produced from renewable sources and has zero emissions upon utilization. It has high specific energy: 33 kWh kg^{-1} compared to 13 kWh kg^{-1} for gasoline. However, its energy density is inherently low – 0.0813 g L^{-1} at 25 °C and 1 bar – and though compression and liquefaction can slightly improve on this, they come at the cost of energy losses during those processes. Liquid hydrogen at −253 °C has an energy density of 2.35 kWh L^{-1}, and compressed hydrogen at 700 bar has approximately 1.6 kWh L^{-1}, not accounting for the weight and volume of the storage system. For comparison, gasoline's energy density is 9.8 kWh L^{-1}.[18–23] Therefore, traditional gas-phase storage technologies face limitations in achieving the long-term objectives of the hydrogen economy due to safety and economic constraints. Solid-state storage materials offer a more promising path due to enhanced safety, a compact structure, and increased H_2 storage density.[18]

Any H_2 storage material should have the following characteristics:[18]

- high H_2 content,
- fast hydrogen uptake and release kinetics,
- high safety in terms of flammability and reactivity,
- low cost of materials,
- durability and stability in terms of degradation over repeated cycles and long-term storage conditions,
- close to ambient operating conditions, as opposed to high temperatures and H_2 pressures,
- high efficiency in terms of required energy input for storing and releasing hydrogen.

Metal hydrides offer benefits such as cost-effectiveness, safety, high hydrogen storage capacity, and possible operation at low pressures and temperatures, with the highest energy densities and specific energies under mild conditions exhibited by complex metal hydrides. These include borohydrides, alanates, and nitrides.[18]

The advantages of alanates are the low price and abundance of the component compounds, low weight, non-toxicity, and that no volatile gases besides hydrogen are formed. Most alanates possess high gravimetric hydrogen densities, but high thermodynamic and kinetic barriers remain obstacles to viable widespread applications.[24,25] Sodium aluminum hydride or sodium alanate ($NaAlH_4$) is an extensively studied low-density material (1.24 g cm^{-3})[26] that could be used for reversible hydrogen storage.[18,25,27,28] $NaAlH_4$ has a relatively high hydrogen content: 7.47 wt%. Although a promising material, the main limiting factor is its high

kinetic barrier, although high temperatures required for decomposition and formation and poor reversibility are also issues.[24,29,30] It has been shown that Ti and other transition metal based catalysts can greatly enhance the dehydrogenation and hydrogenation of $NaAlH_4$, but repeatability over several cycles is limited, especially when it comes to hydrogenation.[18,24,25,27]

$NaAlH_4$ decomposes in three stages.

$$NaAlH_4(s) \rightleftarrows \frac{1}{3}NaAlH_6 + \frac{2}{3}Al(s) + H_2 \uparrow \quad \text{(R1)}$$

$$\frac{1}{3}Na_3AlH_6(s) \rightleftarrows NaH(s) + \frac{1}{3}Al(s) + \frac{1}{2}H_2 \uparrow \quad \text{(R2)}$$

$$NaH(s) \rightarrow Na(l) + \frac{1}{2}H_2 \uparrow \quad \text{(R3)}$$

The first two stages (R1 and R2) are reversible and release a total of 5.6 wt% of H_2, with 3.7 wt% attributed to R1 and 1.9 wt% attributed to R2. This is 75% of the total H_2 content in the material.[19,24,30] Figure 1 shows the rate of hydrogen evolution against temperature for $NaAlH_4$. R1 is a prolonged process starting between 145–183 °C. This is mostly from the surface and defect sites. Kinetic hindrances are eliminated to a large degree at the melting point of 183 °C. R2 begins around 240 °C, and it is indistinguishable from R1 in bulk alanate. The irreversible R3 occurs at > 300 °C as NaH is thermally very stable.[19,24,30,31] However, the equilibrium pressure calculated from the enthalpy values (ΔH is 37 kJ mol^{-1} and 47 kJ mol^{-1}, respectively) is 1 bar for R1 and R2 at 30 °C and 100 °C, respectively.[27] This means that though these processes are kinetically hindered below the melting point in the bulk material, severely reduced H_2 release temperatures can be achieved.

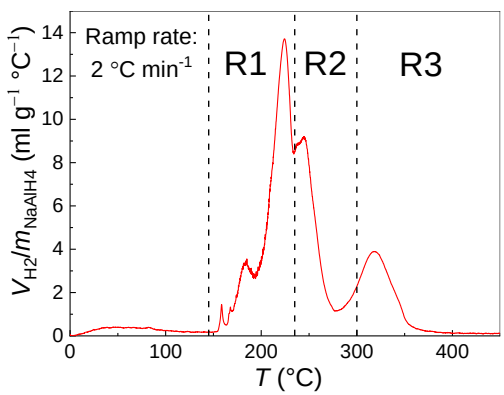

Figure 1. The temperature dependence of the differential volume of released H_2 normalized with the mass of $NaAlH_4$. The temperatures where $NaAlH_4$'s decomposition reactions take place are marked R1-R3.

Though theoretically, R1 and R2 are reversible, in practice, they remain irreversible in bulk alanate. One of the main causes is the spatial separation of the NaH and Al phases or the accumulation of Al into larger particles after repeated cycling.[29] In general, with catalysts, nanoscaling, and nanoconfinement, kinetics, thermodynamics, and reversibility can be improved.[18,25,27,28,31–46]

4.1.2. Strategies to improve $NaAlH_4$ characteristics for H_2 storage

This work will combine two approaches to help lower the required temperatures and H_2 pressures for dehydrogenation and hydrogenation of $NaAlH_4$. These are nanostructuring and nanoconfinement.

Nanostructuring, i.e., reducing the particle size until one dimension is < 100 nm, has emerged as one promising strategy to improve the kinetic and thermodynamic properties of $NaAlH_4$.[18,25,27,28] These changes stem from increased surface-to-volume ratios, increased surface area and activity, and shortened diffusion distances.[47] Ball milling has been shown to be an effective way of reducing particle size[18,27,28,47,48], but is also useful for doping[37–40,48–50] or creating mixed hydride systems[41,48] that have alternative dehydrogenation pathways. The ball milling process also creates highly reactive surfaces, and the higher density of grain boundaries facilitates hydrogen diffusion. Thus, the overall kinetics of dehydrogenation and hydrogenation are increased.[47]

Nanoconfinement of $NaAlH_4$ within a porous scaffold material prevents phase segregation and helps maintain particle size. By inhibiting the aggregation of separate phases, it eliminates the need for their diffusion during hydrogenation to reform the pristine hydride. Additionally, confinement prevents denser phases from settling at the bottom of the storage tank.[47,51] Scaffold materials have several vital functions: they facilitate nanoparticle formation, inhibit sintering, and improve the alanate's overall thermodynamic and kinetic properties and the system's durability, i.e., maintaining the system's properties over several cycles. The scaffold/nanomaterial interface influences the final hydrogen storage properties of the composite.[25,28,31,32,34,42,43,47,52]

Porous carbon materials are low-cost, tunable, chemically inert, have high thermal stability in an inert atmosphere, are lightweight, and have high thermal conductivity. The decrease in the mass fraction of the alanate and the increase in volume with the use of a carbon material are well compensated by the system's increased performance, i.e., the enhancement of the capability to store hydrogen reversibly.[51] The effects of carbon materials on sodium alanate's hydrogen storage properties have been studied in the past.[25,27,28,30,47] Specifically, $NaAlH_4$ composites ball milled together with carbon aerogel have been investigated and described by Pinkerton.[42] Even at low aerogel loadings, the kinetics and reversibility of R2 improved, with hydrogenation occurring at 19.8 bar H_2 and 140 °C. Another carbon material of interest is carbon black, which consists of near-spherical nanoparticles typically fused into larger aggregates, that tend to agglomerate further into even larger particles.[53]

4.1.3. Neutron diffraction for the study of H_2 storage materials

Significant advancements have been made in addressing sodium alanate's kinetic, reversibility, and temperature limitations. A thorough understanding of complex hydride chemistry is essential for the rational design of systems that enable the applicability of sodium alanate and all other hydrides. This encompasses insights into their structure, thermolysis pathways, H_2 evolution mechanisms, ion dynamics with temperature, and chemical bonding characteristics. Neutron diffraction and other scattering methods have been crucial in enhancing our comprehension of complex hydrides and continue to be vital tools for researchers.[54]

Neutron powder diffraction (NPD) is a powerful tool for the analysis of crystalline materials. The basic principles of NPD align with powder X-ray diffraction (PXRD). However, since scattering takes place from the nucleus, not the electron cloud, as in the case of PXRD, it has higher sensitivity to light elements and can even distinguish isotopes. Therefore, NPD excels in the study of H_2 storage materials and is complementary to PXRD.[54,55]

The coherent neutron scattering cross section influences diffraction peak intensity. Incoherent scattering cross sections produce broad background features independent of the scattering angle that can obscure weak diffraction peaks. The substantial incoherent cross-section for H complicates diffraction experiments. H exhibits a coherent scattering cross section of 1.8 barns (1 barn = 10^{-28} m^2) and a large incoherent cross section of 80.3 barns. The addition of a neutron to H significantly alters its coherent and incoherent scattering cross sections: 5.6 and 2.05 barns, respectively. As deuterium (D) displays a reduced incoherent scattering cross section, it is wise to substitute H for D for structural analysis based on neutron scattering experiments. Unlie diffuse electron clouds, atomic nuclei act as point scatterers. Consequently, neutron scattering form factors remain stable across measurement angles.[54] Replacement of H atoms with D atoms in $NaAlH_4$ is achievable in multiple ways.[56–58] Isotope exchange is possible in a D_2 pressurized environment, especially if the material is previously dehydrogenated. This can be further driven by high temperatures and the small particle size of the $NaAlH_4$ material.

Neutrons are also able to penetrate the material deeply, enabling *operando* studies of bulk materials *in situ*. This allows the investigation during dehydrogenation/dedeuteration and hydrogenation/deuteration, revealing structural and chemical changes. This helps determine intermediate reaction products, phase transformations, and reaction rates.[55] Therefore, neutron scattering methods are particularly applicable and necessary for investigating H_2 storage materials.

There are a variety of studies investigating the *in-situ* dehydrogenation and hydrogenation behavior of complex metal hydrides using X-ray and neutron techniques.[54,59–67] However, there is still significant research to be done investigating systems where $NaAlH_4$ is confined in porous carbons. There, the behavior and interactions of $NaAlH_4$ and the carbon remain to be elucidated. There are indications that the carbon scaffold material may substantially alter the reaction pathways, dependent on the chemical composition of the scaffold

itself.[54,66–68] Post-dehydrogenation small-angle X-ray scattering indicates the preferential filling of accessible mesopores, where nanoparticles are formed.[68] Small-angle neutron scattering has demonstrated that $NaAlD_4$ particles nano-confined within porous scaffolds maintain their size distribution and exhibit remarkably stabilized morphology.[69] Finally, a synchrotron PXRD and NPD study analysed the hydrogenation of Ti-doped $NaAlH_4$. They confirmed that Al initially reacts with NaH to form Na_3AlH_6, with the onset of $NaAlH_4$/$NaAlD_4$ formation occurring before the total consumption of NaH/NaD. This concurrent process is in contrast with the traditionally assumed sequential decomposition reactions.[63]

4.2. Li-ion batteries

4.2.1. The motivation for long lifetimes

There are many aspects of Li-ion batteries that can be optimized and improved: energy density, specific energy, power and rate capabilities, safety, lifetime, and cost. In general, improving one aspect, e.g., increasing energy density via increasing the operating voltage, comes at the expense of another, e.g., lifetime. In the past, energy density has been prioritized over other characteristics. However, when considering, for example, electric vehicles (EVs), the daily need for most users is < 100 km, which makes up 25–50% of an EV's range.[70,71] Therefore, most of the battery's capacity remains unused. Since higher voltages, i.e., operating a battery at its maximum capacity, reduce lifetime due to an increase in parasitic reactions,[72–74] many automakers recommend[75–77] keeping the battery pack between 20–80% capacity during everyday use. Even though this increases battery longevity,[78] automakers only warranty their batteries for less than a decade,[79,80] even though they likely still retain more than 80% of their original capacity. This is traditionally considered the end of life, though batteries may remain operable far beyond the 80% capacity mark. These batteries could be used in second-life applications to satisfy demand and provide economic benefits.[81,82] Moreover, there are already examples of non-EV battery warranties > 10 years.[83–85]

Considering the necessity of swift integration of renewable energy sources,[86] the significance of battery longevity becomes more evident.[10] On the one hand, the demand for more battery storage capacity and, thus, production, is ever-growing. On the other hand, the accessibility of raw materials and limits to production capacity set constraints on how quickly battery capacity can be grown. If battery lifetimes are very limited, more production capacity must be directed towards replacing obsolete batteries in all applications, rather than expanding global storage capacity. Increased longevity of Li-ion cells postpones the need to replace obsolete batteries, enabling increased total capacity production, but also reducing the costs of building and maintaining these systems.[10]

These long lifetimes give rise to a new issue. With modern batteries having longer and longer lifetimes, how does one predict their lifetime? This returns us to the question of extending the warranties for battery packs. If the lifetime of a Li-ion battery cell is in the order of decades, one cannot simply test a cell until its

end of life. This is because the development cycle of products is far shorter, for example, 3 years for an EV. Therefore, accelerated testing methods must be utilized, and regardless of the exact methodology, a lifetime model is required.[87]

A long lifetime Li-ion cell is required to develop and validate this model. This requires significant optimization of all components of the cell: from electrode materials to form factor. The aim is to reduce degradation modes to a minimum, until only active Li loss remains. With a single degradation mode, one not only has an excellent long lifetime cell, but can also begin to construct a model around it. As one of the main goals of this thesis is the development of such a cell, the rationale behind the cell development is explained in the following chapter.

4.2.2. Construction of a long-lifetime Li-ion cell

Cells containing $Li[Ni_xMn_yCo_{1-x-y}]O_2$ (NMC) positive electrodes are typically reserved for high-energy cells, as the materials exhibit higher specific energies and average operating voltages.[88,89] The increase in operating voltage can lead to more oxidizing conditions, limiting lifetime and reducing stability, creating safety concerns in the charged state.[73,74,90–96] Furthermore, the use and acquisition of Ni and particularly Co come at a considerable expense and ethical complications.[97–100]

The higher voltage utilized in the NMC cells introduces numerous potential degradation modes: irreversible phase transitions,[89,101–104] electrolyte oxidation,[103,105,106] and particle cracking.[107–109] These can significantly reduce cell lifetime. However, it has been shown recently that by limiting the upper cutoff voltage (UCV), NMC cells can exhibit excellent lifetimes while still maintaining energy densities higher than $LiFePO_4$ (LFP) cells.[74,91] This, as discussed previously, is due to the fact that electrolyte oxidation on the positive electrode is limited at lower voltages. Secondly, microcracking due to volume changes of polycrystalline NMC materials is also inhibited.[110–112] This can be even further avoided by combining low voltages with single-crystal materials.[10,113–115]

Artificial graphite remains a key negative electrode material. Though small particle sizes and large surface areas enable better rate capability, they also offer more surface area for active Li loss via solid-electrolyte interphase (SEI) growth. Therefore, one has to choose a graphite material with minimal electrochemically active surface area to prolong lifetime.[116,117]

Ethylene carbonate (EC), diethyl carbonate (DEC), ethyl methyl carbonate (EMC), and dimethyl carbonate (DMC) remain some of the most common commercial electrolyte solvents.[118] Even though a model system is needed, ideally, it would be as close as possible to a real commercial cell, and carbonate-based solvents have already been optimized after decades of research.[119] Different variations provide an electrolyte more optimized for high rate, long lifetime, high temperature, or low temperature. NMC cells with the more novel and exotic dimethyl-2,5-dioxahexane carboxylate (DMOHC) in combination with DEC and lithium bis(fluorosulfonyl)imide (LiFSI) as salt operating at low voltages have shown incredible capacity retention and minimal gassing while cycling at 85 °C.[115,120]

Lithium hexafluorophosphate ($LiPF_6$) is the most common salt used in Li-ion battery electrolytes.[121] However, it has been shown to decompose at temperatures > 70 °C;[122,123] therefore, using the more temperature-stable LiFSI would be preferred, as accelerated testing requires testing at temperatures up to 100 °C.[124] A concern with salts, such as LiFSI or lithium bis(trifluoromethanesulfonyl)imide (LiTFSI) is that they may cause corrosion of the Al current collector.[123,125,126] This should, however, be mitigated by low voltages and can also possibly be mitigated by blending LiFSI with $LiPF_6$.[126,127]

Small amounts of electrolyte additives can have a big impact on cell lifetime and performance. Vinylene carbonate (VC) is one of the most common additives used to help passivate the graphite electrode. Other additives, such as ethylene sulfate (DTD), prop-1-ene-1,3-sultone (PES), and tris(trimethylsilyl) phosphite (TTSPi), are known for improving positive electrode stability, gas production limiting, and lifetime extending abilities, respectively.[128–133]

Lastly, pouch cells are a convenient form factor for electrolyte development, being easy to produce and handle. On a commercial scale, they benefit from higher specific energy as the laminate pouch bag is lighter than a sealed metal can. However, sealed metal cans, such as the cylindrical 18650 form factor, benefit from a more robust container that can hold a more tightly wound electrode, increasing energy density, and are more resistant to rupture due to excessive gas production.[134]

4.2.3. Predicting the lifetime of Li-ion cells

The main tool for estimating or predicting the lifetimes of Li-ion cells is accelerated lifetime investigation. The goal is to identify and quantify ageing in a short period of time. One way of doing this is by increasing the precision of measurement without accelerating the degradation mechanisms. Therefore, one can quickly detect the smallest degradation. Another strategy is to accelerate the ageing mechanisms to make the degradation faster. This can be done, for example, by increasing the temperature or the applied current.[87] This work takes the approach of combining these two strategies and using accelerated testing, mainly increasing the temperature, and high precision measurements to measure characteristics required for lifetime estimation.

The high precision measurement is ultra-high precision coulometry (UHPC), which enables the assessment of ageing behavior within a month.[135] During a UHPC experiment, the current source output is accurately and precisely monitored, high-precision and temperature-controlled components are utilized, and data sampling rates are increased. Coulombic inefficiency (CIE), charge endpoint capacity slippage (slippage, Δc), and capacity fade (fade, $f = \Delta d - \Delta c$) are the three most important characteristics obtained from a UHPC measurement.[136–138]

Figure 2 prepared by Claire Floras illustrates the meaning of these metrics.[139]

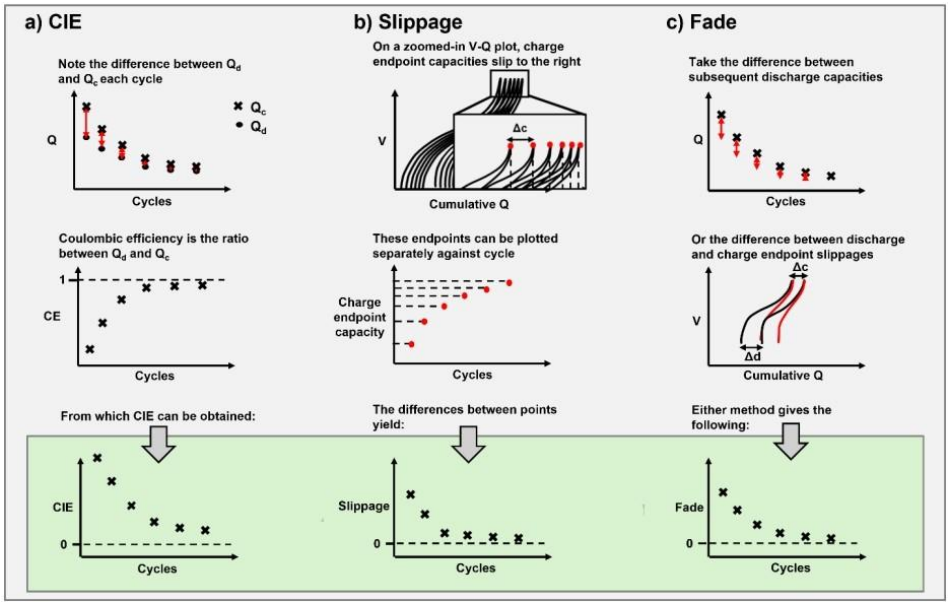

Figure 2. Illustrations of how to calculate a) coulombic inefficiency (CIE), b) charge endpoint capacity slippage (slippage), c) capacity fade (fade) from capacity and voltage data obtained from UHPC. This is a modified version of a figure by MSc Claire Floras from Ref.139. Used with permission.

Coulombic efficiency (CE) is defined as the ratio of discharge capacity to the preceding charge capacity:

$$\mathrm{CE} = \frac{Q_\mathrm{d}}{Q_\mathrm{c}}. \tag{1}$$

If CE were exactly 1, then that would imply that no parasitic reactions are occurring, and a battery could cycle indefinitely. However, this is never the case as even in a well-designed Li-ion cell, there are always some parasitic reactions taking place. Primarily, there will always be some active Li lost into the SEI that passivates the negative electrode, resulting in incremental capacity loss.[140,141] Hence, even in the best-performing Li-ion cell, CE can only be very close to unity (~1.00000). Measuring CE very accurately can help estimate how many cycles a cell can perform before reaching end-of-life, which is typically defined as 80% of its original discharge capacity. However, since batteries have a very high CE (> 0.997), one has to measure it at least to the precision of 0.0001. A UHPC instrument measures CE to the precision of 0.00001.[135]

CIE is a better metric to analyze UHPC data, as it is the sum of parasitic reactions attributed to the positive electrode – slippage – and those attributed to the negative electrode – fade. CIE is defined as:

$$\mathrm{CIE} = 1 - \mathrm{CE} = 1 - \frac{Q_\mathrm{d}}{Q_\mathrm{c}}. \tag{2}$$

CIE is related to slippage and fade via the following equation:[136]

$$\mathrm{CIE} = \frac{f}{Q_\mathrm{c}} + \frac{\Delta c}{Q_\mathrm{c}}. \tag{3}$$

$\frac{f}{Q_\mathrm{c}}$ is referred to as fractional capacity fade and $\frac{\Delta c}{Q_\mathrm{c}}$ as fractional charge endpoint slippage. As at the low constant currents used (C/20), time, *t*, is the primary contributor to CIE, then these values are often normalized to the time required for one full cycle:[137]

$$\frac{\mathrm{CIE}}{t} = \frac{f}{Q_\mathrm{c} t} + \frac{\Delta c}{Q_\mathrm{c} t}. \tag{4}$$

These very high-precision measurements enable the estimation of how many cycles it takes to reach 80% capacity. Furthermore, they allow for the deconvolution of reactions on either electrode separately and give insight into both reactions that consume Li inventory and those that do not. However, UHPC alone has its limitations. CE is affected by C-rate, and the low C-rates used give no information on the cell's internal resistance. Therefore, CE measurements are good for ranking based on lifetimes but insufficient for lifetime predictions. The insights gained about the processes taking place at each electrode are valuable, but direct extrapolation has its limitations.[87]

Another way of accelerating ageing is cycling at elevated temperatures.[142] If the primary degradation mode of the cell is Li-inventory loss, caused by chemical reactions on the negative electrode expending active Li into the SEI, the temperature dependence of these processes can be approximated by the Arrhenius equation:[143,144]

$$A = \gamma e^{\frac{-E_\mathrm{a}}{RT}}, \tag{5}$$

where A is the reaction rate (in our case, the degradation rate), γ is the pre-exponential factor (frequency factor), E_a is the activation energy, R is the universal gas constant, and T is the absolute temperature. Using elevated temperatures can reduce the required cycling time to reach 80% capacity from years to mere months. The elevated temperatures enable the manifestation of degradation modes that may go unnoticed when cycling at room temperature.[142] However, there are major challenges in transferring high-temperature testing results to low-temperature lifetimes. Firstly, the goal is to exacerbate and accelerate degradation modes present in the cell at lower temperatures, not introduce new ones. New

degradation modes or the disproportionate and intense acceleration of degradation modes irrelevant at lower temperatures can skew any extrapolation of results to lower temperatures.[87]

Secondly, the question remains on how to extrapolate high temperature data to lower temperatures or even already measured data into the future. SEI growth during lifetime testing is considered similar to thin film oxide growth on a metal surface. That is, they follow the parabolic growth law, which describes diffusion-limited processes. As Li inventory loss into the SEI is considered the primary degradation mode in well-optimized cells, and is the main one considered in the context of this work, then discharge capacity loss also follows the parabolic law: [145–151,140,152]

$$\frac{Q(t)}{Q_0} = 1 - A\sqrt[2]{t}, \tag{6}$$

where $Q(t)$ is the capacity at any given time, Q_0 is the starting capacity, $\frac{Q(t)}{Q_0}$ is thus the fractional capacity as a function of time, A is the degradation rate or proportionality constant, and t is the cycling time. The parabolic growth law in this case is also sometimes referred to as the square root time model. From this follows, firstly, that if one knows the A value at a given temperature, the lifetime of the cell can be extrapolated from these results. Secondly, if the A values at two different temperatures and the amount of time it takes to reach a given fractional capacity value at one of those temperatures, one can calculate the time it takes to reach that same fractional capacity value at the other temperature:

$$1 - A_1\sqrt[2]{t_1} = 1 - A_2\sqrt[2]{t_2}, \tag{7}$$

$$t_2 = \left(\frac{A_1}{A_2}\right)^2 t_1. \tag{8}$$

Equation 8 is the first step in developing a model that can estimate Li-ion cell lifetimes into decades with reasonable accuracy.

There is a plethora of studies showing data aligning well with Eq. 6,[147,148,153] where the Arrhenius behavior of the degradation rate is also explored.[91,116,149–152,154–158] By eliminating as many degradation mechanisms as possible, with active Li loss being the primary one, a verifiable model descriptive of the internal processes of the cell can be developed. By cycling the cells in a wide temperature range between 20 and 100 °C and using UHPC, the benefits of both accelerated testing and high precision measurements can be combined. The high-temperature UHPC data allows the detection and quantification of processes that may typically take years of room-temperature testing to observe, within a month. By establishing a relation between temperature and UHPC metrics, which can be applied to higher rate accelerated testing performed at elevated temperatures,

more real-life use cases can be simulated. This enables the interpretation of accelerated testing results from elevated temperatures into room temperature lifetimes, giving more accurate lifetime predictions. This has the potential to be applied to battery warranties and enabling more second-life use cases.

5. EXPERIMENTAL

5.1. Hydrogen storage material synthesis

The $NaAlH_4$ (90%, Sigma-Aldrich, Germany) was purified with the recrystallization method performed in an MBraun LABmaster sp glovebox (MBraun, Germany), filled with argon (Ar, 5.0, Linde, UK). For recrystallization, bulk $NaAlH_4$ was dissolved in tetrahydrofuran, THF (anhydrous, ≥ 99.9%, Sigma-Aldrich, Germany), at ambient temperature (~20 °C), resulting in a 0.05 g_{NaAlH4} mL^{-1}_{THF} solution. The solution was filtered through a glass microfiber filter (GF/B, Whatman) to remove any insoluble impurities. The THF was removed via the Buchi R-215 Rotavapor System, which includes the B-491 Heating Bath, V-710 vacuum pump, and V-855 vacuum controller (Buchi, Switzerland). The $NaAlH_4$ solution in THF was held at 26 kPa and 50 °C until most of the THF had evaporated. Then the sample was maintained at ambient temperature and < 0.1 kPa for 15 h to remove any remaining THF.

5.1.1. Solution impregnation

$NaAlH_4$ was deposited on a high surface area, microporous, and high porosity, dry carbon material RP-20 (Kuraray, Japan) through the solution impregnation method. A 0.05 g_{NaAlH4} mL^{-1}_{THF} solution was used for all samples. Samples with 5, 60, and 100 wt% of deposited $NaAlH_4$ were synthesized to yield the nano-confined, bulk-deposited, and bulk $NaAlH_4$, respectively, and are denominated as such. In the case of the bulk $NaAlH_4$ sample, recrystallization is performed at identical conditions, but without the carbon support material. All syntheses, sample storage, and sample preparation for further analysis were performed in an Ar-filled (5.0, Linde) glovebox (MBraun LABmaster sp, Germany).

5.1.2. Ball-milling

An appropriate ratio of the mesoporous carbon black Vulcan XC72R (Cabot, USA) and the recrystallized $NaAlH_4$ was weighed in a glovebox and placed into a ZrO_2 grinding bowl containing 10 mm ZrO_2 grinding balls. The carbon black had been dried at 150 °C and 10 kPa using a Vaciotem TV vacuum oven (J.P Selecta, Spain) before it was transferred into the glovebox. The ball-to-mass ratio was roughly 75:1. The system was hermetically sealed with a clamp in an Ar environment. The materials were ground in a PULVERISETTE 6 classic line planetary mono mill (Fritsch, Germany) for 40 min, allowing 10 min cooling breaks every 5 min. $NaAlH_4$/carbon black composites with 50, 60, 70, 80, and 90 wt% of $NaAlH_4$ were synthesized. The composites are designated as NCxx, where "xx" is the $NaAlH_4$ content in wt% (e.g., NC50 is a $NaAlH_4$/carbon black composite with 50 wt% $NaAlH_4$).

5.2. Temperature-programmed dehydrogenation (TPD)

The temperature-programmed dehydrogenation (TPD) experiment enables kinetic and quantitative data about the H_2 evolution process to be obtained.[31] The temperature is linearly raised during the experiment while a steady stream of inert carrier gas flows through the powder sample.[159] When the activation energy is exceeded, the hydride decomposes, releasing H_2 into the flowing gas, which then carries it into the detector. The AutoChem 2950 HP chemisorption analyzer (Micromeritics, USA) utilizes a thermal conductivity detector to measure gas concentrations. When analyzing H_2 (187 mW m^{-1} K^{-1} at 300 K), N_2 (26 mW m^{-1} K^{-1} at 300 K) is used as the carrier gas.[160] The measured signal is proportional to the concentration of the detected gas. For calculations, a calibration constant is used to convert the thermal conductivity data into values that directly represent the concentration of evolved H_2. To obtain this constant, calibration measurements, where fixed and known amounts of H_2 are injected into the N_2 stream, were performed. From the measured data, both the rate and quantity of evolved H_2 can be calculated, giving a thorough overview of the material's H_2 storage properties.

The constant carrier gas flow used was 50 mL min^{-1} N_2 (6.0, Linde). The sample was transported hermetically sealed to the instrument and was supported on quartz wool inside the sample holder. Measurements were performed on ~10 mg of the sample. Before the measurements, the sample was flushed with Ar, and the temperature was stabilized at 0 °C. Before and after the temperature ramp routine, the thermal conductivity signal was measured for 2 h for stabilization of the system and background subtraction. Measurements were performed from 0 °C to 600 °C with a temperature ramp rate (ΔT or β) between 0.5 and 10 °C min^{-1}, with 2 °C min^{-1} used for most characterizations.

5.3. Gas sorption

All materials were characterized using the N_2 sorption method utilizing the ASAP 2020 (Micromeritics, USA) surface area and porosity analyzer. The samples were prepared in an Ar-filled glovebox. Pure carbon black was degassed at 300 °C and vacuum of at least 1.3×10^{-6} bar or lower for 12 h. The composite materials were degassed at ambient temperatures and under pressures of 3.3×10^{-6} bar or lower for 24 h. The composites were degassed at lower temperatures to avoid the melting and decomposition of $NaAlH_4$. The BET theory[161] was used to calculate the specific surface area (S_{BET}). The total pore volume (V_{tot}) was calculated from the adsorbed amount at $p/p_0 = 0.95$, which estimates the total pore volume of pores with widths ≤ 40 nm.

5.4. Powder X-ray diffraction (PXRD)

The Vulcan XC72R, $NaAlH_4$, and $NaAlH_4$/Vulcan XC72R composites were characterized using the PXRD method. The measurements were performed with a D8 Advance (Bruker, USA) diffractometer using a low-background airtight

specimen holder. The samples were prepared in an Ar-filled glovebox. Ni-filtered Cu Kα radiation was used, and the diffractogram was measured with a LynxEye detector. Measurements were done in the 2θ range of 13–80° with a step of 0.016°. The collected data were analyzed with the Diffrac Suite EVA software package and the PDF4+ 2020 database.[162] The crystallite sizes were estimated using TOPAS 6 software and the Double-Voigt method.[163]

5.5. Dehydrogenation/hydrogenation cycling

The dehydrogenation/hydrogenation cycling experiments were performed with the iSorb HP1 (Quantachrome, USA) high-pressure gas sorption system. 300–400 mg of composite material was placed into an autoclave and attached to the machine. All sample preparation and handling were performed in an Ar-filled glovebox. Dehydrogenation, under high temperature and low H_2 pressure, and hydrogenation, under high temperature and high H_2 pressure, cycles were performed. The dehydrogenation procedure began with the depressurization of the autoclave. Then, the composite was dosed to $p_{H2,dehydro}$, and the temperature was ramped to $T_{dehydro}$, at a rate of 10 °C min^{-1}. The amount of hydrogen evolved from the sample was calculated from the measured pressure change. After dehydrogenation for a fixed time, $t_{dehydro}$, the sample was evacuated, dosed to $p_{H2,hydro}$, and the temperature was set to T_{hydro} at a ramp rate of 10 °C min^{-1}. The sample was held under pressure for t_{hydro}. Post-cycled composites were characterized by TPD and PXRD.

5.6. Deuteration and neutron powder diffraction (NPD)

Deuteration of the milled samples was performed with the iSorb HP1 high-pressure gas sorption system. 1.64 g of sample was held under vacuum at 170 °C for 24 h, and then D_2 gas pressure of 160 bar was applied for 72 h. Based on the D vs H occupancies obtained from refinement of NPD data, a ≥ 90% replacement of H with D was achieved. All sample preparation, manipulation, and storage steps were performed under Ar atmosphere.

In-situ NPD measurements were performed on the D20 instrument at ILL, France.[164] Incident neutrons with a wavelength of 1.54 Å were obtained from the (115) reflection of a Ge monochromator at 90°. Cylindrical sample holders with an inner diameter of 6 mm were used. Diffraction patterns of empty sample holders were measured in the temperature range from 27 °C to 177 °C under vacuum conditions, in order to subtract the background and to assign the diffraction peaks caused by the sample cell. The $NaAlD_4$/carbon black sample was prepared in an inert gas-filled glovebox. The sample and sample stick gas line were hermetically sealed for transportation from the glovebox to the instrument and during the connection to the gas handling system. Four heating, D_2 pressurization (with multiple concurrent dosing steps), and cooling cycles were performed. Diffractograms were obtained over 10 min and 5 min in the case of

isothermal conditions and temperature ramp conditions, respectively. The raw scattering data is available in the ILL data repository.[165]

The diffraction pattern of the empty sample cell was subtracted from all measurements, yielding a pattern consisting of $NaAlD_4$/carbon black and the incoherent background signal caused by the applied D_2 pressure (p_{D2}). As the equilibrated temperatures were not equivalent between the applied routine and the empty sample cell measurements, the signal subtraction was not perfect, and four 2θ regions were excluded from further analysis, between 44 and 45.5°, between 63 and 66.5°, between 98 and 100°, and between 115 and 118°. The carbon black additive causes wide diffraction peaks at all experimental conditions. In addition, some of the diffraction peaks from different crystalline phases overlap, and after the first dedeuteration/deuteration cycle, the diffraction peak intensities decrease considerably. This makes the determination of crystalline composition difficult. Thus, refinement of *in-situ* NPD data was performed at all experimental temperatures and D_2 gas pressure conditions applied to obtain quantitative crystalline phase compositions.

The Topas software package was used for the applied refinement routines.[166] Sequential fitting routines were applied for the batch refinement of multiple diffractograms in one go. H-based equivalent crystalline structures obtained from the Materials Project[167] and works by Gross et al[168] and Ke and Tanaka[169] taken as a basis for the refinement of $NaAlD_4$, Na_3AlD_6, NaD, and Al structures. The H and D isotope occupancy, occ, was fitted based on the assumption that $occ_H + occ_D = 1$ for each site. Neutron scattering from the isotopes, H and D, could be separated based on the divergent coherent neutron scattering cross-section (1.758 barn for H vs 5.592 barn for D) and the ratio of coherent/incoherent neutron scattering cross-sections (0.02 for H vs 2.73 for D).[54] The spherical harmonics preferred orientation correction was applied to the refinement of the carbon crystal structure. This was done to account for the anisotropic crystalline ordering, i.e., different length scales of crystalline ordering for intra- and inter-layer graphitic structures.

Initially, refinement was performed with all possible crystalline phases present. Certain crystalline phases were eliminated based on the high uncertainty of the refined wt% in comparison to the obtained value and based on the divergence of lattice parameters of the refined structure in comparison to the original structure. The goodness of fits (GoF) for all refinements was below 1.65. The weighted profile R-factors were between 6.8 and 13.5, and the expected R-factors were between 4.1 and 10.8, yielding the aforementioned GoF values.

The amount of D_2 released during the decomposition/deuteration cycles applied during the NPD measurements was calculated from the *in-situ* pressure readings. The free volumes in the gas handling system used for the calculation were determined beforehand with He, and the temperatures of different zones were measured *in situ* during the experiment.

5.7. Pouch cells and electrolyte

Machine-made 402035-sized pouch cells supplied by LiFUN Technology (Zhuzhou, Hunan Province, China) were received vacuum-sealed without electrolyte. These pouch cells have an extended gas bag, allowing visual examination of whether gas is produced and estimation of the amount of gas produced according to how much the gas bag has expanded. The positive electrode materials were commercially supplied single-crystal (SC) $Li[Ni_{0.5}Mn_{0.3}Co_{0.2}]O_2$ (NMC532) paired with the negative electrode material "artificial graphite A" (AGA), polycrystalline $Li[Ni_{0.83}Mn_{0.06}Co_{0.11}]O_2$ (Ni83) paired with "artificial graphite C" (AGC), and SC $Li[Ni_{0.6}Mn_{0.4}Co_{0.0}]O_2$ (NMC640) paired with AGC. The graphite materials have been discussed previously.[116,117] The NMC532/AGA cells were balanced to 3.8 V with a nominal capacity of 160 mAh, the Ni83/AGC cells were balanced to 4.06 V with a nominal capacity of 240 mAh, and the NMC640/AGC cells were balanced to 4.05 or 4.1 V with a nominal capacity of 240 mAh.

The cells were cut open in an Ar-filled glovebox and dried under a dynamic vacuum at 120 °C for 14 h. Cells were filled in the glovebox with ~0.63 g (0.55 mL) of electrolyte in the case of the NMC532 cells and ~1 g (0.85 mL) of electrolyte in the case of the Ni83 and NMC640 cells. Then, they were vacuum sealed at 0.1 bar absolute pressure (MSK—115 A, MTI Corp). The solvents used were ethylene carbonate (EC), dimethyl carbonate (DMC), ethyl methyl carbonate (EMC), diethyl carbonate (DEC), and dimethyl-2,5-dioxahexane carboxylate (DMOHC). They were used in various solvent blends (w/w): DMOHC:DEC (1:4), EC:DEC (1:1), EC:DEC (1:2), EC:DEC (1:4), EC:DMC (3:7), and EC:EMC (3:7).

The additives used were vinylene carbonate (VC), ethylene sulfate (DTD), prop-1-ene-1,3-sultone (PES), and tris(trimethylsilyl) phosphite (TTSPi). The combinations used were:

1) 2 wt% VC + 1 wt% DTD,
2) 2 wt% VC + 1 wt% DTD + 0.5 wt% PES,
3) 3 wt% VC + 1 wt% DTD + 0.5 wt% PES,
4) 4 wt% VC + 1 wt% DTD + 0.5 wt% PES,
5) 2 wt% VC + 0.5 wt% PES,
6) 3 wt% VC + 0.5 wt% PES,
7) 4 wt% VC + 0.5 wt% PES,
8) 2 wt% PES,
9) 2 wt% PES + 1 wt% DTD,
10) 2 wt% PES + 1 wt% DTD + 1 wt% TTSPi

The salts used were 1 M lithium bis(fluorosulfonyl)imide (LiFSI), 0.4 M LiFSI + 0.4 M lithium bis(trifluoromethanesulfonyl)imide (LiTFSI), 0.5 M LiFSI + 0.5 M LiTFSI, or 0.9 M LiFSI + 0.1 M lithium hexafluorophosphate ($LiPF_6$). All electrolyte components were obtained "battery grade" from Capchem (Shenzhen, Guangdong, China) and their structures are shown in Figure 3.

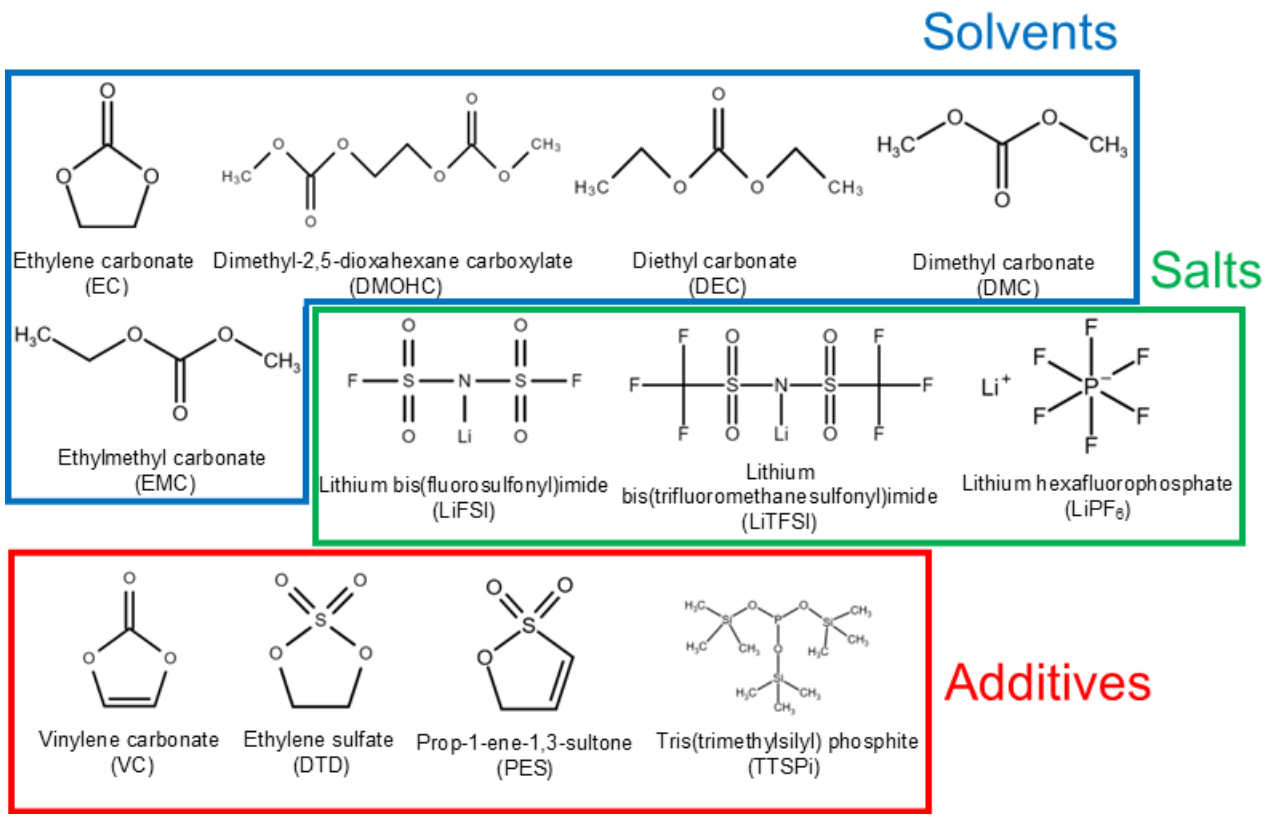

Figure 3. Electrolyte components used in this thesis.

The cells were held at 1.5 V for 24 h to ensure proper wetting of the electrode stack. The cells were formed on a Maccor 4000 series charger at C/20 up to their respective UCVs, 3.8, 3.9, 4.0, or 4.1 V at 40 °C. After formation, cells were again cut open in an Ar-filled glovebox and re-sealed with the vacuum sealer to remove any formation gases.

5.8. Electrolyte loss measurements

Cells were weighed in ambient conditions on an analytical balance (Shimadzu AYW200D) prior to and after cycling to measure any solvent loss due to permeation through the seals of the pouch cells at high temperatures. An experiment to specifically measure electrolyte loss was conducted by filling dry pouch cells and empty 18650 cylindrical cans with electrolyte as described in chapters 5.7. and 5.12. Then, their masses were recorded, and the cells and cans were placed into temperature boxes at 70 °C, 85 °C, and 100 °C. The cells and cans were removed from the temperature boxes at regular intervals, and their masses were recorded. The changes in mass correspond to solvent loss.

5.9. *Ex-situ* gas volume measurements

The gas volume in a pouch cell was measured using Archimedes' principle.[170] The pouch cell was suspended from a hook connected to the bottom of an analytical balance (Shimadzu AYW200D). The cell was then submerged in deionized water (18 MΩ cm), and the mass was recorded. The change in mass can be used to calculate the volume change caused by gas evolution:

$$\Delta Vol = \frac{-\Delta m_{\text{balance}}}{\rho_{\text{water}}}, \tag{9}$$

where $\Delta m_{\text{balance}}$ is the difference of the mass measurement before and after cycling, and ρ_{water} is the density of deionized water at 20 °C (0.998 g mL^{-1}).

5.10. Long-term cycling and ultra-high precision coulometry (UHPC)

Long-term constant current constant voltage (CCCV) cycling was conducted on Neware cyclers (Shenzhen, China) or Novonix ultra-high precision cyclers (Nova Scotia, Canada). Cells were cycled at 85 °C or 100 °C from 3.0 V to 3.8, 3.9, 4.0, or 4.1 V. All cycling was done at C/3 with C/20 capacity check-up cycles after every 50 cycles at 85 °C and 25 cycles at 100 °C.

UHPC experiments using Novonix cyclers were conducted at 10.0, 20.0, 40.0, 55.0, 70.0, 85.0, and 100.0 ± 0.1 °C with a current corresponding to C/20 from 3.0 to 3.9 or 4.0 V.

5.11. Scanning micro X-ray fluorescence spectrometry (μXRF)

After cycling experiments, the pouch cells were discharged to 2.5 V and disassembled. μXRF measurements were performed to quantify Mn and Al deposited on the negative electrode. The calibration method for quantification has been reported previously.[171] The negative electrode from the disassembled cell was unrolled and dried under the fume hood for 12 h. A piece of the electrode was cut and mounted on a polyacrylic plate. An electrode from a pristine unfilled cell was prepared in a similar manner to measure the background signal and establish a baseline. The Bruker M4 Tornado spectrometer (Bruker, USA) used a Rh tube, 50 kV and 600 μA, an Al200Ti200 filter, a 20 μm X-ray spot size, a 100 μm scanning step, and a 10 ms scan time per pixel when analyzing Ni and Mn. When Al was analyzed, no filter was used, and the tube current was 300 μA.

5.12. Cylindrical cells and electrolyte

Machine-made, 18650-sized cylindrical cells supplied by LiFUN Technology (Zhuzhou, Hunan Province, China) were received in vacuum-sealed bags without headers and electrolyte. The electrode chemistry and chemically inactive components of the cell (e.g., separator) were the same as in the SC NMC640/AGC pouch cell format. The cells were balanced to 4.05 V with a nominal capacity of about 2100 mAh. The headers were spot welded to the cathode tab, the electrolyte was filled (4.5 ml (5.3 g)), and the headers were crimped in place.

The electrolyte used was EC:DEC (1:1) 1 M LiFSI with 2 wt% VC + 1 wt% DTD, and the formation process was the same as for the pouch cells, except for skipping the post-formation degassing step.

5.13. Torr-sealing of cells

In order to hinder solvent permeation, the seals of the pouch and cylindrical cells were covered with commercially supplied Torr Seal® – a high-temperature and high-vacuum epoxy resin marketed by Agilent (Lexington, MA, USA). Figure 4 shows pouch and 18650 cylindrical cells before and after Torr-sealing. Only the crimp seal of the 18650 cells was covered with Torr Seal.

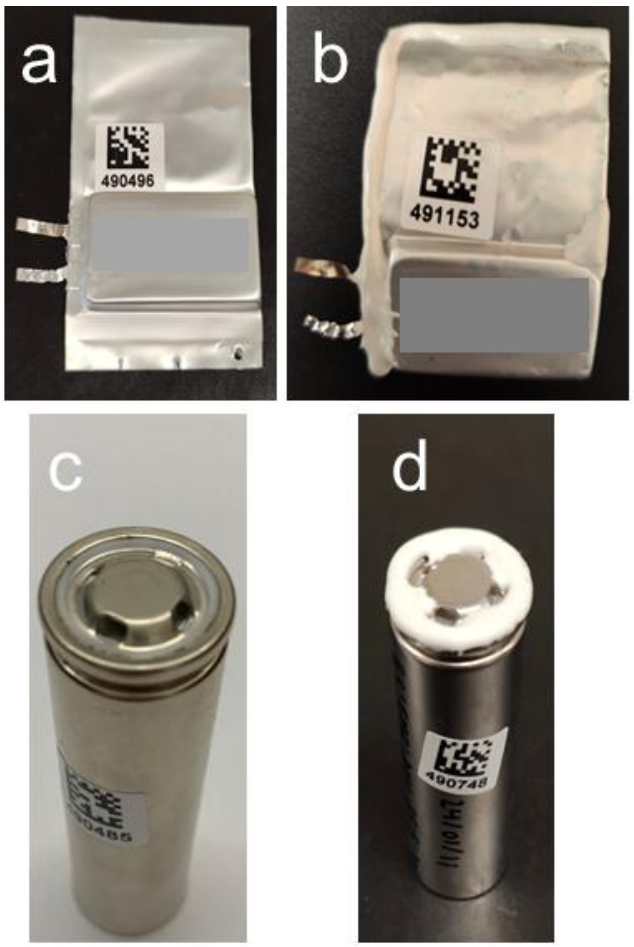

Figure 4. Photos of the front view of a typical pouch cell (a), same view as panel a) of a Torr-sealed pouch cell (b), top view of a typical 18650 cylindrical cell (c), same view as panel c) of a Torr-sealed 18650 cylindrical cell (d).[V]

6. RESULTS AND DISCUSSION

6.1. Hydrogen storage

6.1.1. Influence of nanostructuring on the dehydrogenation properties of $NaAlH_4$

The analysis presented in this chapter is based on publications I and III.

Figure 5 shows the distinct H_2 release curves exhibited by bulk, bulk-deposited, and nanoconfined $NaAlH_4$. The carbon scaffold material used, RP-20, is a microporous carbon.[31] Therefore, the $NaAlH_4$ can be deposited into the porous structure as nanoparticles or onto the surface of the carbon as a thin film. In the case of bulk $NaAlH_4$, a low amount of H_2 is released just below the melting temperature of 183 °C and is most likely from the surface layer and defect sites of the material. At 200 °C, H_2 release increases considerably via R1 and R2. The final decomposition step begins at 280 °C, with the material having completely decomposed by 375 °C.

The bulk-deposited material has very limited H_2 release < 90 °C. The exact temperature depends on the temperature ramp rate and the source of the constant rate H_2 evolution is likely highly polycrystalline or nanosized alanate particles. A high amount of H_2 is released in a narrow temperature range starting at 165 °C, followed by a slightly reduced rate up to 200 °C. After that, there is a constant low H_2 release up to ~375 °C. These correspond to R1 from the surface, R1 and R2 from bulk, and R3.

The nanoconfined material starts to release H_2 already at ambient conditions and H_2 is released in a wide range, mostly < 200 °C. The curve shape is very dependent on the temperature ramp rate. A low additional H_2 release at > 400 °C is likely from the decomposition of NaH.

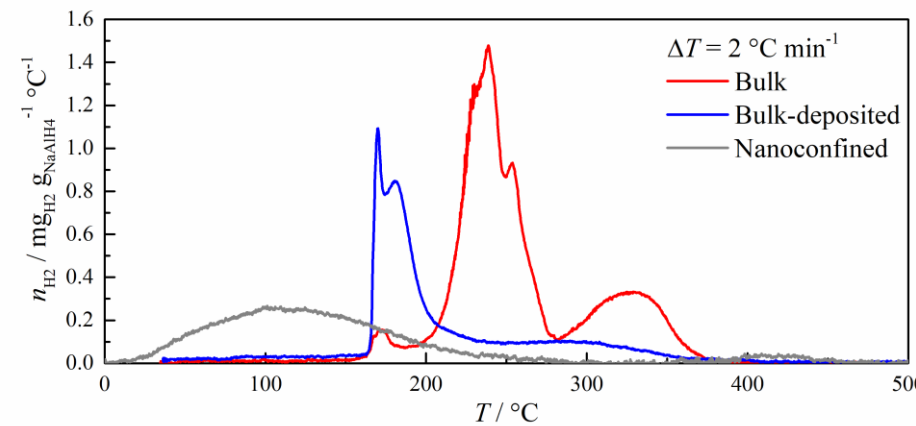

Figure 5. Hydrogen release curves of bulk (red), bulk-deposited (blue), and nanoconfined (grey) $NaAlH_4$ measured at a constant temperature ramp rate of 2 °C min^{-1}.[I]

The corresponding H_2 release efficiencies (released H_2 compared to theoretical H_2 content) for bulk, bulk-deposited, and nanoconfined materials are ~100%, ~66%, and ~40%, respectively. The decrease in efficiencies is likely caused by the decomposition of $NaAlH_4$ during synthesis or the loss of nanoconfined material at storage conditions (~21 °C and Ar gas environment).

The H_2 release curves were fitted with a combination of gaussian and bigaussian peak functions to help deconvolute the different release processes taking place. The bigaussian profile is caused by the kinetic limitation of a decomposition step. Initially, the increase in the released H_2 amount is quick. After reaching a maximum H_2 release at T_{max}, it will continue over a wide temperature range as the process is kinetically hindered. Figure 6 shows an example of the fit.

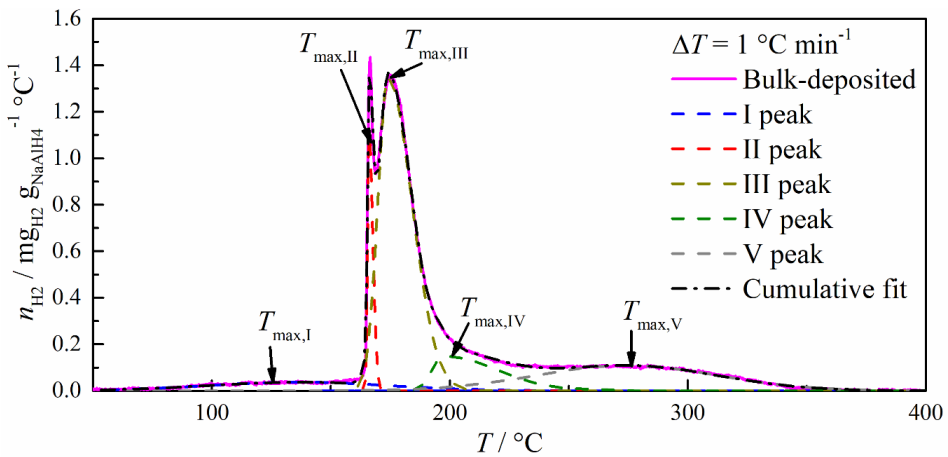

Figure 6. Hydrogen release curve from bulk-deposited measured during a temperature ramp rate of 1 °C min^{-1} with the corresponding hydrogen release peak fits.[I]

The Kissinger method allows for the calculation of the activation energy, E_a, of a first-order reaction by measuring the H_2 release curves at different temperature ramp rates.[172] The equation is:

$$\ln\frac{\beta}{T_{max}^2} = \ln\frac{\gamma R}{E_a} - \frac{E_a}{RT_{max}}, \tag{10}$$

where β is the temperature ramp rate (referred to as ΔT in the figures), R is the ideal gas constant, and γ is the Arrhenius pre-exponential factor. Figure 7 plots $\ln\frac{\beta}{T_{max}^2}$ against $\frac{1}{T_{max}}$. The slope will yield $-\frac{E_a}{R}$ and thus, E_a can be calculated.

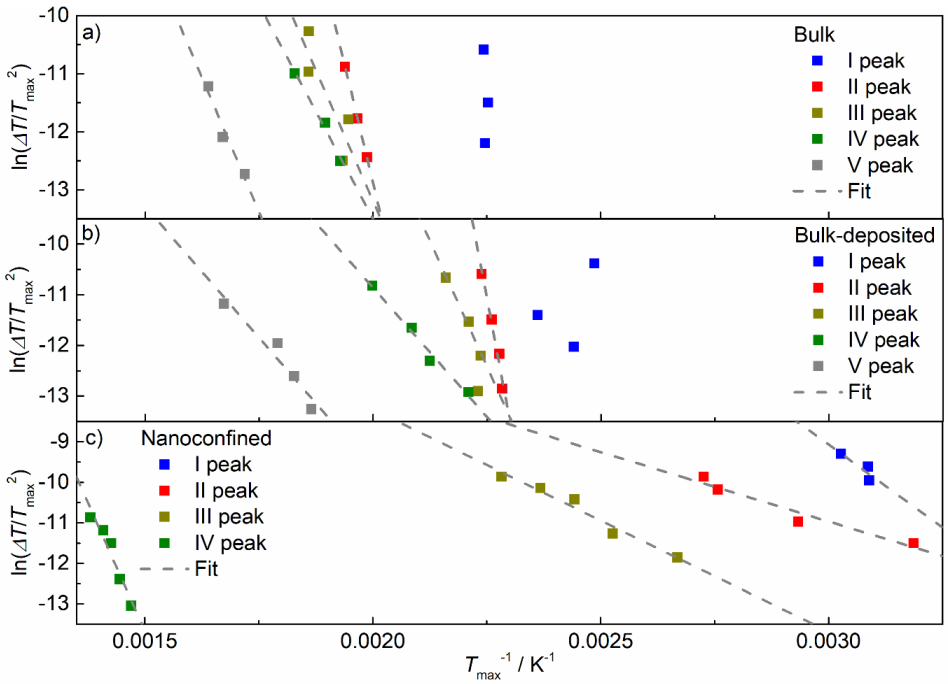

Figure 7. Kissinger equation plots of (a) bulk, (b) bulk-deposited, and (c) nanoconfined $NaAlH_4$ and the corresponding fits to the T_{max} of H_2 release processes obtained from fitting the H_2 release curves with gaussian and bigaussian peak functions. The fit values for each peak at a different temperature ramp rate are denoted with a colored square: blue for the I peak, red for the II peak, olive for the III peak, green for the IV peak, and grey for the V peak.[I]

From these experiments, it is evident that the addition of a porous carbon material reduces the temperature for H_2 evolution in all cases, but the remarkable reduction of activation energies is achieved with nanoconfinement of $NaAlH_4$. In addition to reducing the E_a for R1 and R2 by at least a factor of two, the E_a for R3 was even slightly increased, inhibiting the final irreversible decomposition step. The latter is another benefit for real-life applications, as it increases the material's longevity.

Though initial analysis was performed on a microporous carbon material, further research utilized a mesoporous carbon black. The mesoporosity of the material is considered more accessible for the $NaAlH_4$, especially when methods other than solution impregnation are used. Furthermore, carbon blacks are inherently nanoparticulate, enabling thin films to form on the surfaces and nanoparticles to form in the interparticulate voids. Figure 8 shows gas adsorption measurement results of ball-milled $NaAlH_4$/carbon black composites. It demonstrates a significant reduction of surface area and pore volume due to the ball milling synthesis. This, together with the fact that the isotherm of the pure Vulcan XC72R carbon black is type IV, indicating mesoporosity, while the composite is type II,

which is indicative of nonporous or microporous material,[173] indicates that pore filling has taken place during the ball milling process.

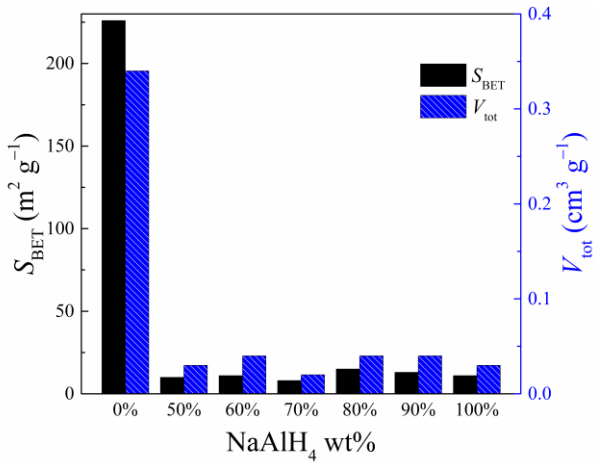

Figure 8. N_2 gas sorption measurement results for $NaAlH_4$/Vulcan XC72R composites with different $NaAlH_4$ wt%. The left y-axis with solid black columns describes the specific surface area calculated according to the BET adsorption theory (S_{BET}), and the right y-axis with striped, blue columns represents the total pore volume (V_{tot}) calculated from the adsorbed amount of N_2 at $p/p_0 = 0.95$.[III]

Figure 9 presents PXRD data for pristine ball-milled $NaAlH_4$ and the composite materials. A crystalline Al phase is observed in composites with ≤ 80 wt% $NaAlH_4$, whereas only $NaAlH_4$ reflections are detected in the NC90 composite and the ball-milled alanate. The intensities of the Al diffraction peaks decrease with increasing $NaAlH_4$ content, indicating that the amount of separate crystalline Al is lower in composites with higher $NaAlH_4$ loading. This suggests that at lower $NaAlH_4$ wt%, nanoscaling is more effective and the influence of the scaffold material is more pronounced, leading to partial decomposition of $NaAlH_4$ during ball milling or even under ambient conditions.

In addition, the absence of diffraction peaks for intermediate phases such as Na_3AlH_6 and NaH further supports this: the smallest $NaAlH_4$ particles likely decompose into polycrystalline or amorphous products that do not yield distinct diffraction peaks. However, the presence of sharp $NaAlH_4$ peaks indicates that a fraction of the material remains in the form of particles of considerable size. Furthermore, the existence of Al peaks shows that the Al resulting from decomposition is not strictly confined and forms larger crystalline particles.

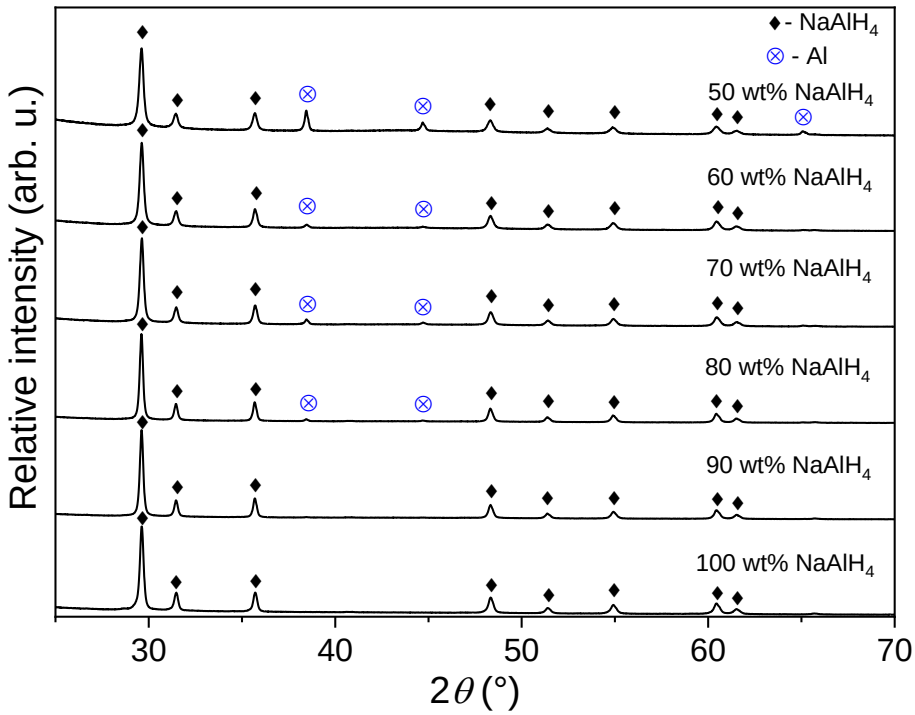

Figure 9. PXRD diffractograms of $NaAlH_4$/Vulcan XC72R ball-milled composites and pristine ball-milled $NaAlH_4$. $NaAlH_4$ diffraction peaks are marked with a black diamond, and Al peaks are marked with a blue circle with a superimposed x. The diffractograms have been shifted vertically for easier comparison, and only the most informative 2θ range from 25° to 70° is presented.[III]

Figure 10 shows the TPD results from pristine $NaAlH_4$, ball-milled $NaAlH_4$, NC50, and NC90. Ball milling significantly reduces the dehydrogenation temperature of the alanate. While limited hydrogen release begins at ambient temperatures, it remains kinetically hindered below approximately 135 °C. A more substantial release is observed around 150 °C. However, these early peaks correspond to very small amounts of H_2. Compared to pristine $NaAlH_4$, the hydrogen evolution peaks in the milled samples occur at lower temperatures but exhibit similar peak widths, suggesting that ball milling reduces particle size, which in turn lowers the dehydrogenation temperature. Notably, a significant portion of $NaAlH_4$ decomposes during the milling process itself, resulting in a lower overall H_2 yield relative to the bulk material.

The incorporation of porous carbons further enhances dehydrogenation performance of $NaAlH_4$. The addition of a small amount of carbon in NC90 mitigates alanate decomposition during milling compared to bulk alanate. This suggests that the carbon scaffolding stabilizes freshly milled particles or aids in dissipating the impact energy from the milling process. NC90 demonstrates a dehydrogenation maximum 25 °C lower than bulk alanate and lacks the three

distinct dehydrogenation peaks (corresponding to R1-R3) typically observed in bulk alanate. Instead, the first two peaks – corresponding to the reversible decomposition reactions R1 and R2 – merge into a single process. The NC50 composite shows even more pronounced changes, with dehydrogenation initiating at near-ambient temperatures. The most significant hydrogen release occurs in the temperature ranges of 100–190 °C for NC50 and 145–235 °C for NC90. This contrasts with the higher dehydrogenation temperature range of bulk alanate, 165–275 °C, where the first two reactions have clearly defined peak maxima, unlike the composites.

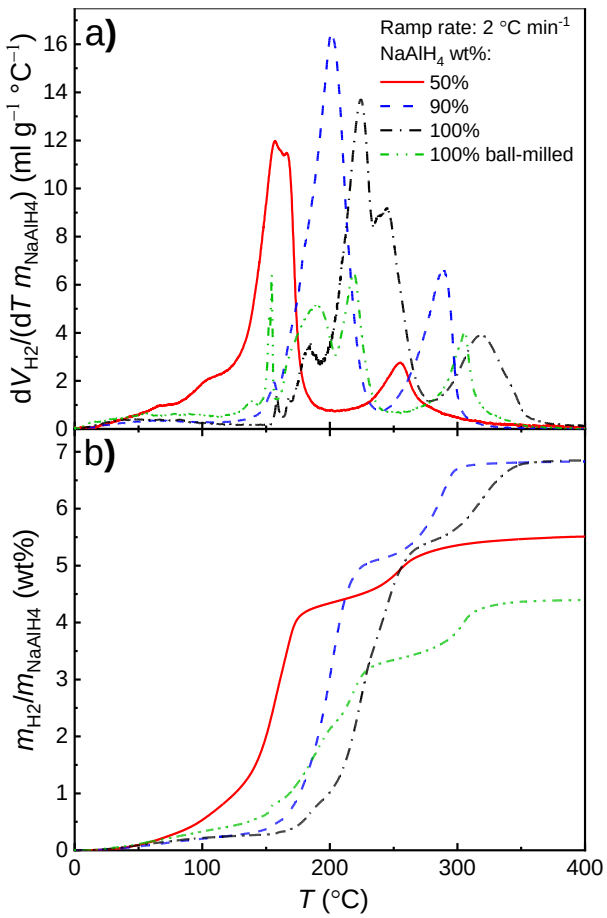

Figure 10. a) Differential volume and b) cumulative mass of released hydrogen normalized to the mass of $NaAlH_4$. Pristine $NaAlH_4$ (dash-dot black line), ball-milled $NaAlH_4$ (dash-dot-dot green line), lowest, and highest wt% composites – NC50 (solid red line) and NC90 (dashed blue line) – are brought for comparison. Only TPD results at ≤ 400 °C are shown for better readability; almost no release of hydrogen was detected at ≥ 350 °C for all composites.[III]

A clear relationship exists between alanate weight percentage and dehydrogenation temperature. The temperature of the first hydrogen release peak maximum decreases from 201 °C to 157 °C as $NaAlH_4$ loading drops from 90 to 50 wt%. This indicates that the $NaAlH_4$ particle size has significantly decreased due to the applied ball milling process. Enhanced nanoscaling and catalytic effects of the scaffold carbon may occur if alanate is deposited as a thin layer on spherical carbon black nanoparticles. The alteration in dehydrogenation temperature and the shape of the TPD curve relative to bulk alanate suggest intermixing and covering of carbon particles during milling, including some filling of interparticulate pores. The scaffolding effects of porous carbon intensify at lower $NaAlH_4$ weight percentages. Notably, intense dehydrogenation begins at approximately 100 °C. The effective hydrogen release is diminished for composites with lower $NaAlH_4$ weight percentages. This indicates that decomposition conditions have been reduced to ambient temperatures, with some material decomposing during milling and storage.

6.1.2 Influence of nanostructuring on the dehydrogenation/hydrogenation cycling of $NaAlH_4$

The effects of nanostructuring on the dehydrogenation/hydrogenation cycling performance of the composite materials were studied in publication III.

Figure 11 shows the results of dehydrogenation/hydrogenation cycling for ball-milled $NaAlH_4$/carbon black composites. It demonstrates that the composites can be hydrogenated at 60 bar, enabling NC50 to be cycled 10 times when the operating temperature is held at 150 °C. The H_2 storage capacity degraded to half of the initially released H_2 over those 10 cycles. The largest drop in H_2 storage capacity was after the first cycle, and the first two reversible reactions (R1 and R2) were both engaged until cycle 7.

When the operating temperature was raised to 190 °C for NC60, the H_2 efficiency for the first cycle was greater, as the material was heated past the melting point of $NaAlH_4$, removing kinetic barriers. However, the loss of efficiency after the first cycle was also much more significant, reaching a stable plateau lower than the one for NC50 after the very first cycle.

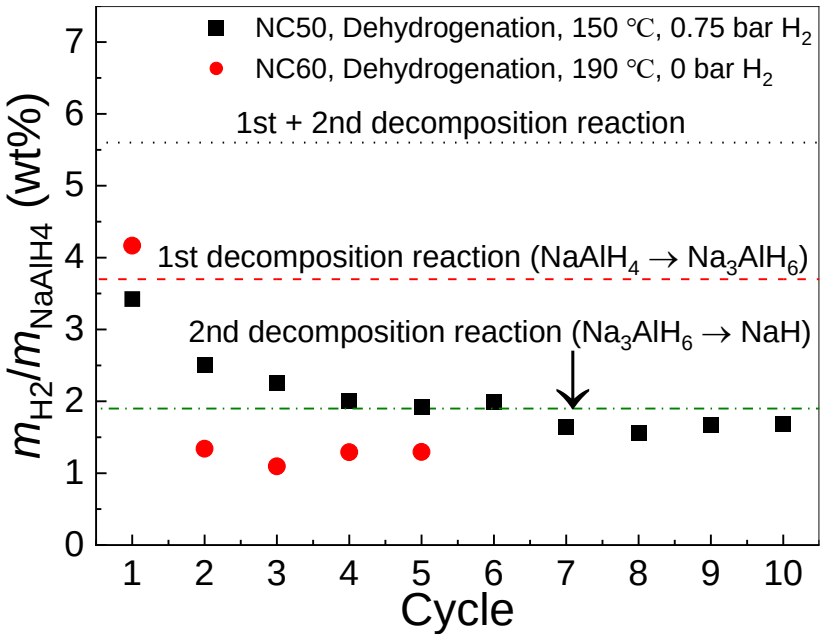

Figure 11. Amount of H_2 released during dehydrogenation of NC50 (black squares) for 4 h at 150 °C, and NC60 (red circles) for 4 h at 190 °C. Materials were hydrogenated under 60 bar of H_2 pressure for 10 h at 150 °C for NC50 and 190 °C for NC60.[III]

Figure 12 shows the post-cycling TPD analysis for the composite materials. The TPD curves of the NC50 samples cycled at 150 °C exhibit a reduction in the total quantity of H_2 effectively stored within the composite after cycling. An initial release of 5.5 wt% of H_2 was observed from the pristine, uncycled composite. Following one cycle, a release of 4.6 wt% of H_2 was recorded, whereas after 10 cycles, 3 wt% of H_2 was attained. During the cycling experiment, the H_2 evolved stabilized at approximately 1.7 wt%, signifying that a portion of H_2 from R1 and R2 (~0.8 wt%) was not released (the irreversible R3 corresponds to merely 1.8 wt%). This phenomenon suggests that the dehydrogenation process is kinetically hindered under these testing conditions.

Notably, the scaffolded material has preserved its principal dehydrogenation peak at 165 °C even after the completion of 10 cycles. However, the intensity of H_2 evolution is markedly diminished across all applied temperature ranges. The observed decline in H_2 capacity is presumably attributable to the material that was not nanoconfined, whereas the confined particles have successfully retained their properties, as evidenced by the consistent shape of the H_2 evolution curve. The observed shift of H_2 evolution towards elevated temperatures may arise from the irreversibility of the initial R1 under the applied hydrogenation conditions.

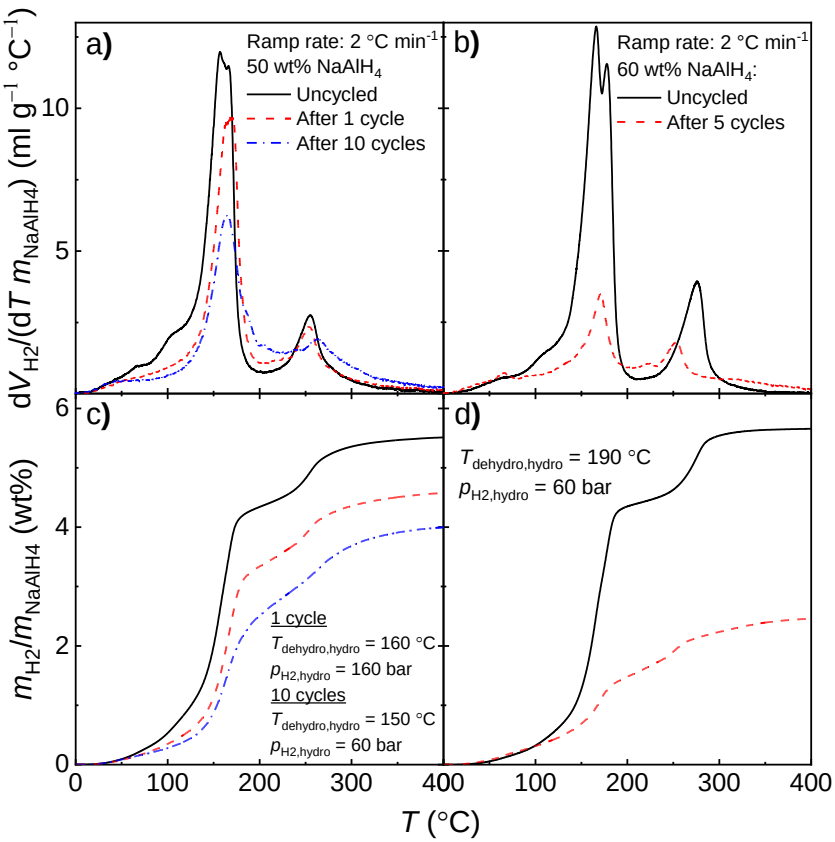

Figure 12. a), b) Differential volume and c), d) cumulative mass of released hydrogen normalized to the mass of $NaAlH_4$. Results of NC50 (a and c) are presented before cycling (uncycled, solid black line), after 1 cycle (dashed red line), and after 10 cycles (dash-dot blue line). Results of NC60 (b and d) are presented before cycling (uncycled, solid black line) and after 5 cycles (dashed red line).[III]

When subjected to cycling at 190 °C, the degradation of NC60 during the cycling process becomes exceedingly evident. As the temperature exceeds the melting point of $NaAlH_4$ (183 °C), the kinetic barriers that impede its decomposition are surpassed. It is important to highlight that the profile of the H_2 release curve remains relatively unchanged, with H_2 evolving across a wide temperature range, despite a significant reduction in the overall quantity of stored H_2 (from 5.6 wt% to 2.7 wt%). Also, the results suggest that most, if not all, of the reversible H_2 was released from the material during the cycling experiment.

The diminished quantity of released H_2 comes from the principal dehydrogenation peak observed within the temperature range of 100–190 °C. This peak is attributed to the liberation of H_2 from sizable particulate or bulk $NaAlH_4$. The capacity for near-ambient dehydrogenation is preserved, signifying that the well-constrained scaffold-supported material retains its H_2 storage capabilities even following the cycling process.

Figure 13 presents PXRD diffractograms acquired prior to and after cycling. In addition to $NaAlH_4$ and Al, the intermediate phase Na_3AlH_6 appears after 10 dehydrogenation/hydrogenation cycles with NC50 at 150 °C. This phase is absent after the first cycle but becomes clearly detectable by the tenth, indicating the progressive crystallite growth of Na_3AlH_6 to sizes sufficient for producing distinct diffraction peaks. The latter observation signifies crystallite growth to such an extent that they yield clearly distinguishable diffraction peaks. This observation, along with the increased intensity of Al reflections, signifies substantial phase separation, particle aggregation, and irreversible decomposition. The resulting larger particles are too kinetically hindered and spatially segregated to be hydrogenated into $NaAlH_4$ under the applied cycling conditions.

Similarly, during cycling of NC60 at 190 °C, diffraction peaks for Na_3AlH_6 and Al intensify, while those for $NaAlH_4$ diminish, mirroring the trend seen in NC50. The elevated cycling temperature – above the melting point of $NaAlH_4$ – promotes irreversible decomposition, with Al segregating into sizeable distinct particles. The scaffolded (nano)particles facilitate the stable H_2 storage capacity ascertained throughout all applied cycles. The H_2 uptake and release observed over all cycles are predominantly attributed to the $Na_3AlH_6 \leftrightarrow NaH$ transition, as the formation of $NaAlH_4$ is obstructed under these cycling conditions.

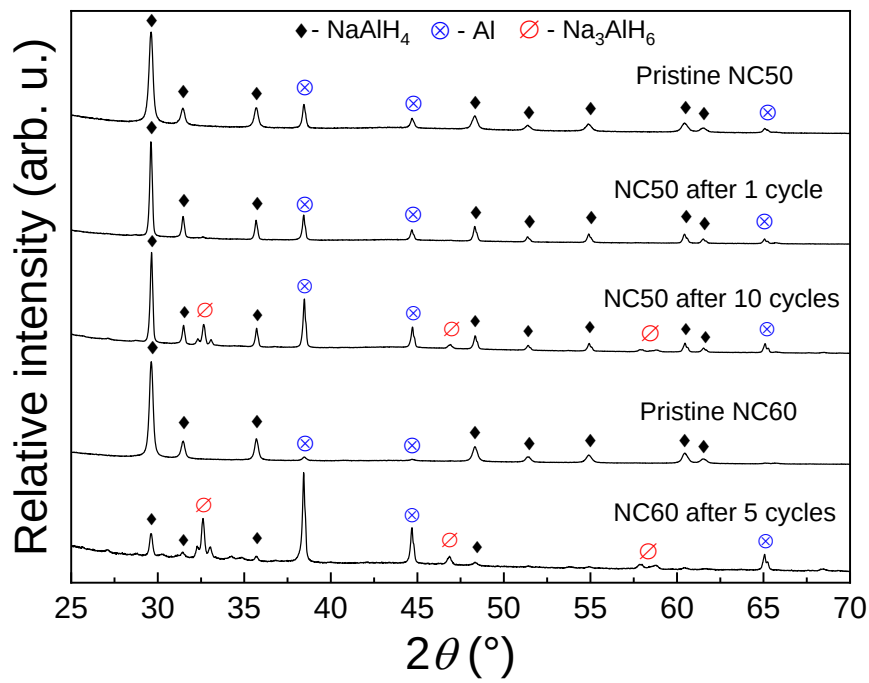

Figure 13. PXRD diffractograms of uncycled and cycled NC50 and NC60. $NaAlH_4$ diffraction peaks are marked with a black diamond, Al peaks are marked with a blue circle with a superimposed x, and Na_3AlH_6 peaks are marked with a red circle crossed by a diagonal slash.[III]

6.1.3. Studying the mechanism of dehydrogenation/hydrogenation of $NaAlH_4$/carbon black composites

The mechanism of dehydrogenation/hydrogenation of the composite materials was studied *in situ* using NPD and is featured in publication II.

Mass ratios of the carbon scaffold, $NaAlD_4$, Na_3AlD_6, NaD, and Al were determined from the refinement of NPD data. The carbon black scaffold consistently accounted for approximately 40% of the total mass throughout the experiment. Its relative contribution decreased during decomposition, as $NaAlD_4$ converted to Na_3AlD_6 and Al, and subsequently to NaD and additional Al. This trend suggests the presence of an amorphous or nanocrystalline deuterated alanate phase in the pristine material, which sintered into larger particles and crystallites at elevated temperatures, thereby reducing the relative scattering contribution from the carbon phase.

To facilitate a clearer comparison of $NaAlD_4$ and its decomposition products, the sum of mass contributions of all non-carbon phases was assumed to be unity at each experimental time point after subtracting the scaffold fraction. Figure 14 shows the results of these calculations. Up to 147 °C, the $NaAlD_4$ comprises over 90% of the crystalline phase. Approximately 20% of the $NaAlD_4$ decomposes in 30 min at 147 °C. The crystalline $NaAlD_4$ phase disappears completely upon heating to 177 °C – just below the melting point of bulk $NaAlH_4$ (183 °C) – and does not form again during subsequent deuteration cycles.

The known phase transitions or melting points of the decomposition products – Na_3AlD_6 (252 °C), NaH (632 °C), and Al (660 °C) – are significantly higher than the experimental temperature range, and therefore, do not influence the calculated mass ratios derived from NPD refinement.

With the disappearance of the $NaAlD_4$ crystalline phase beginning at 147 °C, the mass fractions of Na_3AlD_6 and Al increase, corresponding to the first decomposition step (R1). The subsequent rise in NaD and concurrent decline in Na_3AlD_6 occur only upon cooling to 157 °C from 177 °C, indicating that even with a carbon scaffold, R2 remains kinetically limited by the sluggish progression of R1. This is further supported by behavior observed in subsequent decomposition/deuteration cycles.

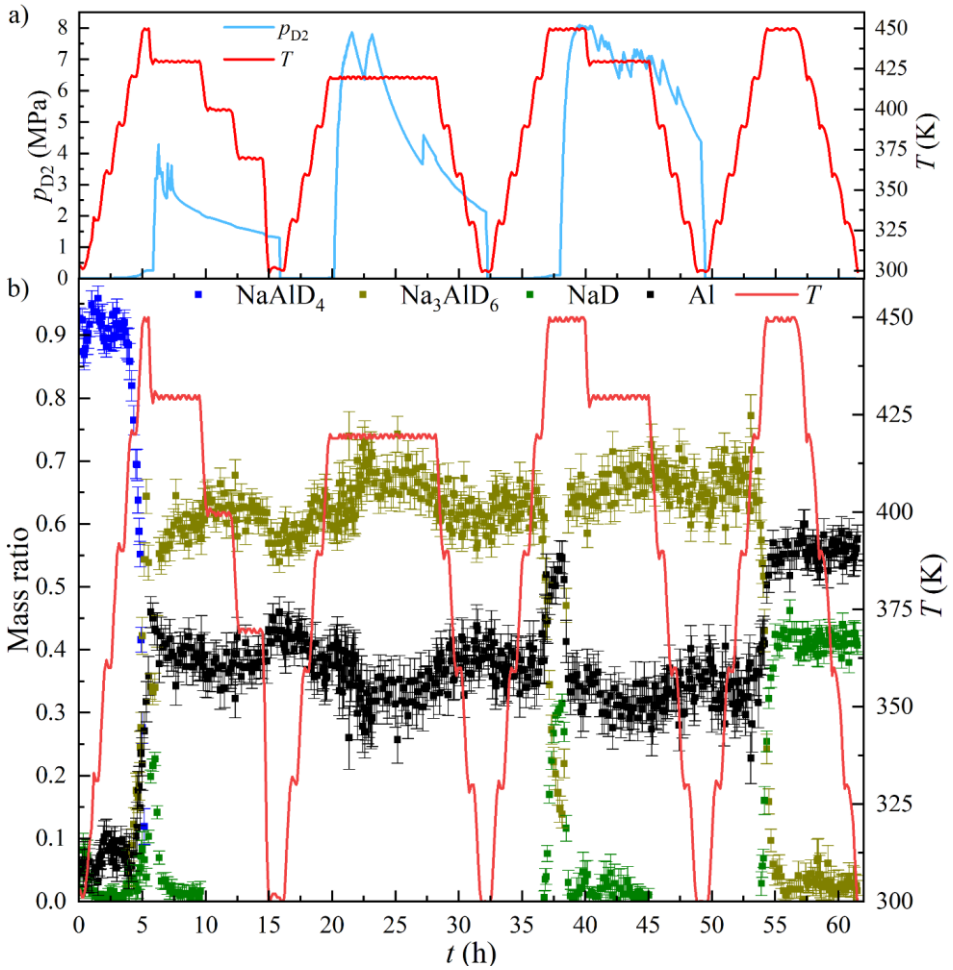

Figure 14. a) D_2 pressure (p_{D2}, light blue line) and sample temperature (T, red line) in the sample cell as functions of experimental time, and b) mass ratios of crystalline phases (blue squares for $NaAlH_4$, olive for Na_3AlH_6, green for NaH, and blue for Al) in the sample plotted versus experimental time. The initial mass ratio of the carbon had been subtracted, and the remaining mass ratios are normalized so that their sum equals unity. Temperature (red line, right y-axis) is overlayed on this panel for reference.[II]

Upon applying a D_2 pressure of > 20 bar at 157 °C, the NaD phase rapidly diminishes, as the majority of the phase disappears in ≤ 30 min, while the Na_3AlD_6 fraction increases. This reflects the reverse of R2, i.e., deuteration of NaD, and results in a stable Na_3AlD_6 mass fraction of approximately 0.61 under these mild hydrogenation conditions. Only crystalline Na_3AlD_6 and Al are detectable, affirming that R2 remains at least partially reversible under these mild conditions. Similar reversibility is observed during the third cycle: NaD forms upon heating to 177 °C and disappears upon subsequent D_2 pressurization. Figure 15 is provided to show the data, including D_2 release, for visual clarity.

Upon heating to 147 °C and dosing with 40 bar of D_2, no change was determined in the crystalline composition. Nevertheless, a pressure increase of 0.3 bar – corresponding to ~5.5 wt% D_2 released from the theoretical maximum – is detected. This suggests the carbon black facilitates the decomposition of $NaAlD_4$ without inducing significant changes in the detectable crystalline phase composition. This behavior is primarily attributed to the decomposition of amorphous or nanoscale $NaAlD_4$ and Na_3AlD_6 components within the composite, which remain undetectable with NPD. The formed Al is separated and largely confined, as no increase in the ratio of crystalline Al is determined during the second heating cycle. Identical release of D_2 at ≤ 147 °C, without a change in the crystalline phase composition, can be seen during the 3rd decomposition cycle. Furthermore, the crystalline phase composition remains consistent up to 147 °C during the 4th cycle, even when vacuum is applied. This consistency across cycles reinforces the stabilizing role of the carbon scaffold and the involvement of non-crystalline or nanophase materials in the hydrogen release process.

The presence of Al in the pristine composite likely originates from partial decomposition of $NaAlH_4$ or $NaAlD_4$ during ball milling and the initial deuteration steps in sample preparation. As neither Na_3AlD_6 nor NaD is detected in the pristine material, any decomposition products present must be amorphous or too small particulate to be detected by NPD.

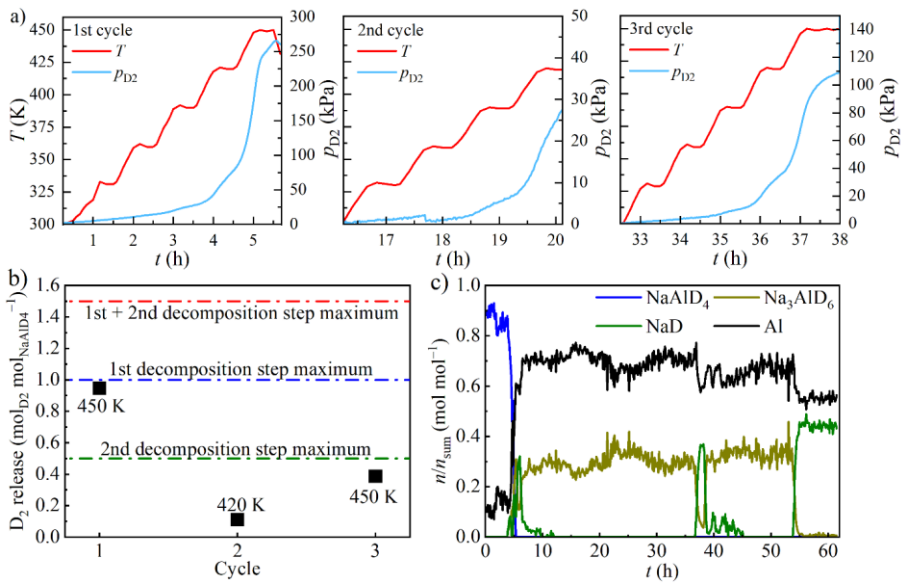

Figure 15. a) Temperature (T, red line, left axes) and D_2 pressure (p_{D2}, light blue line, right axes) profiles during the first three decomposition cycles. The temperature axis has equivalent values for all three cycles for direct comparison. b) Amount of D_2 released, calculated from the pressure increase, during the first three decomposition cycles. The applied decomposition temperatures and the theoretical maximum D_2 release from the initial decomposition reactions are indicated. c) Molar ratios of crystalline phases, determined from the refinement of NPD data. Panel c has the same color scheme as Figure 14b.[II]

During the 4th applied cycle, molar ratios of NaD and Al reached 0.45 and 0.55, respectively, with no additional crystalline phases detected. Based on the equivalent molar ratios of NaD and Al after R2 and Al content present in the pristine composite, full decomposition of $NaAlD_4$ into NaD at 177 °C is ascertained.

6.1.4 Conclusion

Having first understood the significant impact of nanoconfinement in a microporous carbon on the H_2 storage properties of $NaAlH_4$, a new composite was developed and synthesized. To enhance pore accessibility and surface contact with the alanate, a mesoporous carbon black was selected as the scaffold material. This, combined with an increased mass fraction of $NaAlH_4$ and a shift to ball milling as the synthesis method, advanced the system toward practical applicability. The resulting ball-milled $NaAlH_4$/carbon black composite demonstrated reduced dehydrogenation temperatures and improved kinetics, even at a carbon content as low as 10 wt%. These results suggest that, in addition to nanoconfinement, the $NaAlH_4$/carbon interface itself may play an active role in modifying the alanate's hydrogen storage behavior. Notably, dehydrogenation/hydrogenation cycling was achieved under conditions compatible with high-pressure polymer electrolyte membrane electrolyzers.[174]

Through NPD and complementary physical characterization techniques, the system has been thoroughly investigated. This analysis highlighted both strengths and limitations: on the one hand, the composite exhibits efficient lowering of (de)hydrogenation thresholds at high alanate loadings; on the other, it remains hindered by phase segregation and underutilization of R1 during cycling.

Future research targeting high-alanate or complex metal hydride systems at low temperatures and hydrogen pressures should place greater emphasis on the carbon scaffold material. Even small carbon mass fractions showed a significant impact when combined with ball milling. Tailoring the carbon structure – for instance, by synthesizing it from metal carbides such as TiC – offers a pathway to further optimize material performance and facilitate catalyst integration.

6.2. Li-ion pouch cells

6.2.1. Development of Li-ion pouch cells for accelerated testing at elevated temperatures

Firstly, the Li-ion pouch cells were optimized in terms of positive electrode, electrolyte solvent, salt, and additives. The negative electrode was always artificial graphite. The results of these experiments were analyzed in publications IV and VI.

Figure 16 shows long-term cycling results at 85 °C for Ni83, NMC640, and NMC532 cells with either EC:DEC (1:1) or DMOHC:DEC (1:4) as the solvent blend. This experiment evaluates the positive electrodes and principal solvent blend for the most optimal long-lifetime and high-temperature cells. Mid-nickel

cells have shown great promise in the past.[10,91,113] High Ni cells enable higher capacities and have also exhibited great lifetimes when operated at low voltages.[74] DMOHC:DEC is tested to mitigate the known gassing in Ni83 cells[115,120] and possible gassing in NMC640 and NMC532 cells.

NMC640 and NMC532 cells showed no gas production with either solvent blend after extended cycling. EC:DEC (1:1) exhibits clearly better capacity retention in NMC640 (panel e) and NMC532 cells (panel f) compared to Ni83 cells and cells with DMOHC:DEC (1:4). The increase in voltage polarization for NMC532 cells with DMOHC (panel i) is explained by electrolyte permeation from the pouch cell, as discussed in chapter 6.2.2.

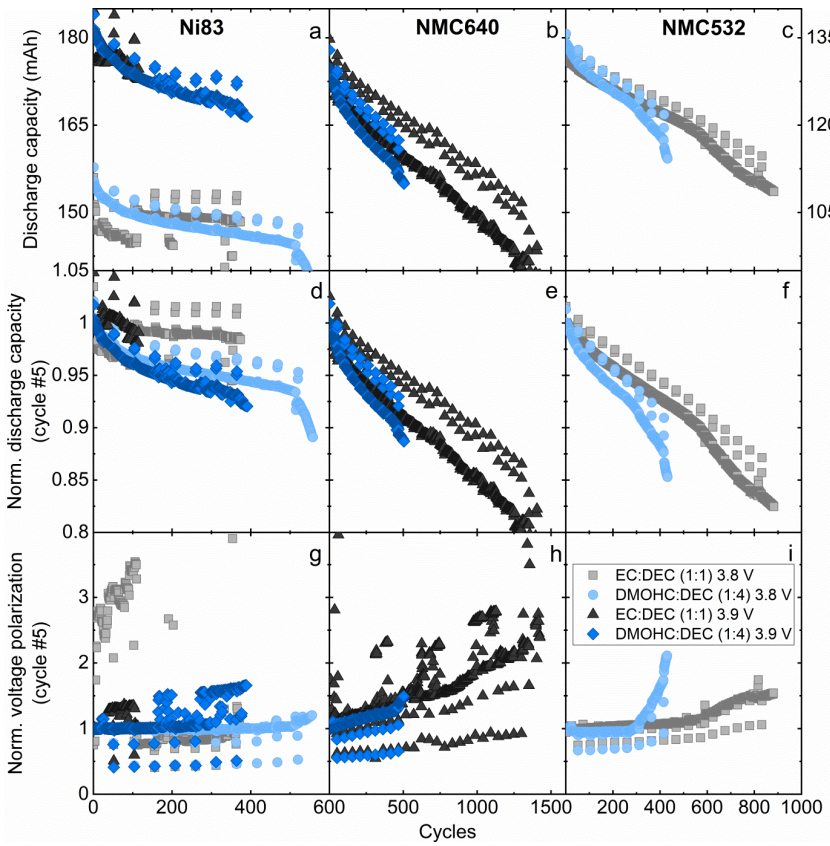

Figure 16. Discharge capacity (a-c), normalized discharge capacity (d-f), and normalized voltage polarization (g-i) for Ni83/AGC (a, d, g), SC NMC640/AGC (b, e, h), and SC NMC532/AGA (c, f, i) with EC:DEC (1:1) and DMOHC:DEC (1:4) cycling C/3 CCCV at 85 °C between 3.0 and 3.8 V (grey squares for EC:DEC and light blue circles for DMOHC:DEC) and 3.0 and 3.9 V (dark grey triangles for EC:DEC and dark blue diamonds for DMOHC:DEC). The electrolyte salt was 1 M LiFSI and the additives were 2 wt% VC and 1 wt% DTD. The second set of sparse data points is the C/20 check-up cycle data, which lies above the C/3 data points in the case of capacity and below the C/3 data points in the case of voltage polarization. Note that panel c has a different y-axis.[VI]

The significant noise in the Ni83 data (panels a, d, g) is from gas production in the cell. Stack pressure was slightly increased after ~100 cycles to more effectively push gas out from between the electrodes. Ni83 cells with DMOHC have an initial advantage, as they prolong gas production, delaying venting. However, gas production remained an issue that could not be managed with gas-limiting additives either.

It can be concluded that the choice of the positive electrode strongly influences cell lifetimes under the applied conditions, as the effects from potential and the negative electrode can be negated with the low voltage and graphite negative electrode used in all cells in Figure 16.

EC is suspected of being the main culprit for gas production in cells with high Ni content positive electrodes, as increased intensity of surface reconstruction and oxygen release may lead to gas-producing reactions with EC.[90,103,175–178] Therefore, the option of reducing gassing by reducing the EC concentration within the cell was explored. Figure 17 shows cycling data for Ni83 and NMC640 with EC:DEC (1:1), (1:2), and (1:4). In the case of NMC640, the performance is almost independent of EC concentration with increased voltage polarization growth and slightly decreased capacity retention, possibly resulting from increased electrolyte permeation rate (chapter 6.2.2.) or decreased conductivity due to the increased DEC mass fraction. This retains the option of reducing the viscosity of the electrolyte by reducing the EC concentration. However, in the case of Ni83, the cell lifetime is significantly improved by reducing EC content, as gas production is also reduced, delaying venting further. Cells with EC:DEC (1:2) and (1:4) perform comparably to DMOHC:DEC (1:4) cells in terms of capacity retention (panel f) and slightly outperform in terms of voltage polarization growth (panel i), while having slightly lower absolute capacity (panel c). Cells with EC:DEC (1:2) started rolling over at cycle 315 with 165 mAh and 93% capacity vs 170 mAh and 94% capacity at cycle 315 for DMOHC:DEC (1:4). This comparison also does not take into consideration that due to the high viscosity and low vapor pressure of DMOHC:DEC electrolyte, venting events may go unnoticed for longer durations, of time with it possibly occurring already at cycle 165, where noise in the data is noticeable. Cells with EC:DEC (1:4) exhibit even longer lifetimes at the cost of a slight decrease in absolute capacity.

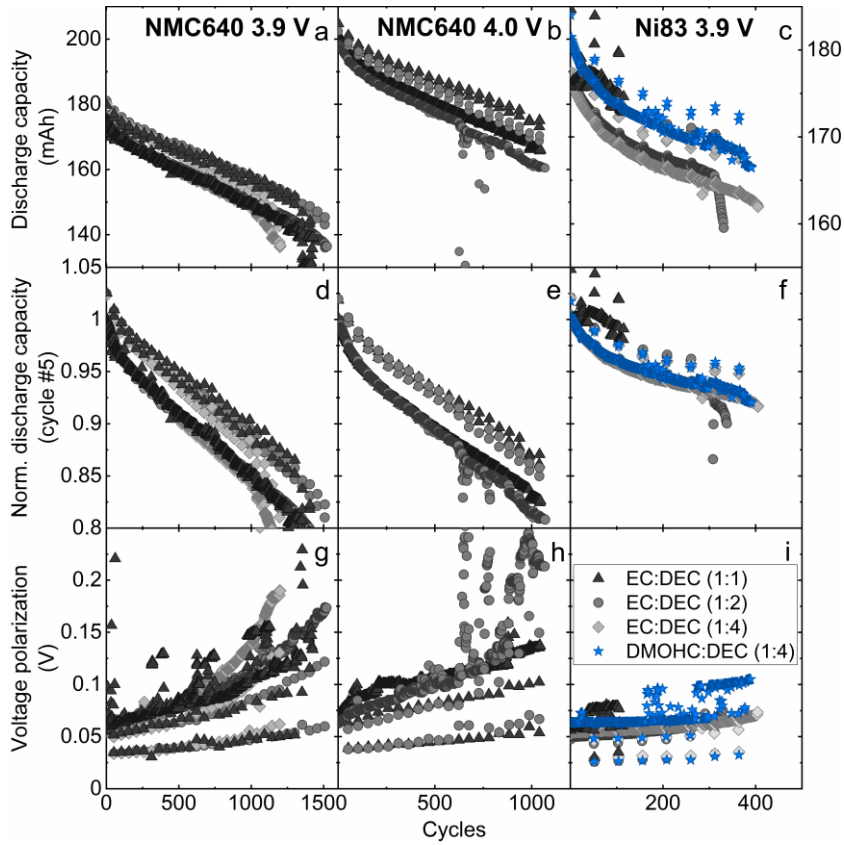

Figure 17. Discharge capacity (a-c), normalized discharge capacity (d-f), and normalized voltage polarization (g-i) for SC NMC640/AGC (a-b, d-e, g-h), and Ni83/AGC (c, f, i) with EC:DEC (1:1) (dark grey triangles), EC:DEC (1:2) (grey circles), EC:DEC (1:4) (light grey diamonds), and DMOHC:DEC (1:4) (dark blue stars) cycling C/3 CCCV at 85 °C between 3.0 and 3.9 V (a, c-d, f-g, i) and 3.0 and 4.0 V (b, e, h). The electrolyte salt was 1 M LiFSI and the additives were 2 wt% VC and 1 wt% DTD. The second set of sparse data points is the C/20 check-up cycle data, which lies above the C/3 data points in the case of capacity and below the C/3 data points in the case of voltage polarization. Note that panel c has a different y-axis.[VI]

Though NMC640 cells with EC:DEC based solvent blends show impressive cycling results at elevated temperatures, most commercial cells operate at temperatures far lower than 85 °C. Figure 18 shows overlayed voltage curves at 20 and 40 °C. The large difference in voltage polarization caused by only a 20 °C temperature increase is evident. This demonstrates that cells with EC:DEC (1:1) suffer a significant capacity penalty at 20 °C.

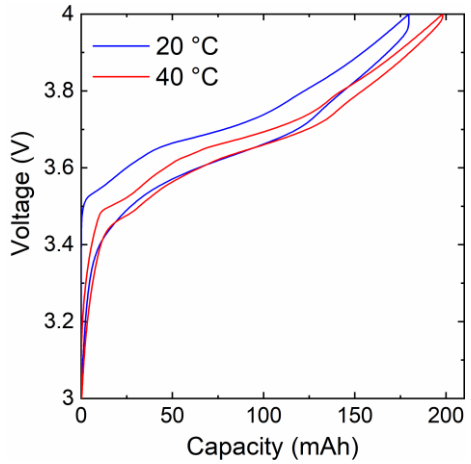

Figure 18. Voltage-capacity curves of single-crystal NMC640/AGC cells using EC:DEC (1:1), 1 M LiFSI, 2 wt% VC, 1 wt% DTD. These cells were cycled C/20 at 20 °C (blue) and 40 °C.[IV]

To mitigate this, other co-solvents, such as DMC and EMC, were considered for their lower viscosities to yield electrolytes with higher conductivities than DEC.[118] Figure 19 shows cycling results for NMC640 cells with EC:DEC (1:2), EC:EMC (3:7), and EC:DMC (3:7) at 85 °C. EC:DMC cells show far more rapid capacity fade and also exhibit intense gassing. However, cells with EC:EMC (3:7) showcase comparable cycling behaviour to cells with EC:DEC (1:2). Though EMC is challenging to use at 100 °C due to its close boiling point of ~107 °C,[179] it may come into consideration for cells designed for lower temperature performance.

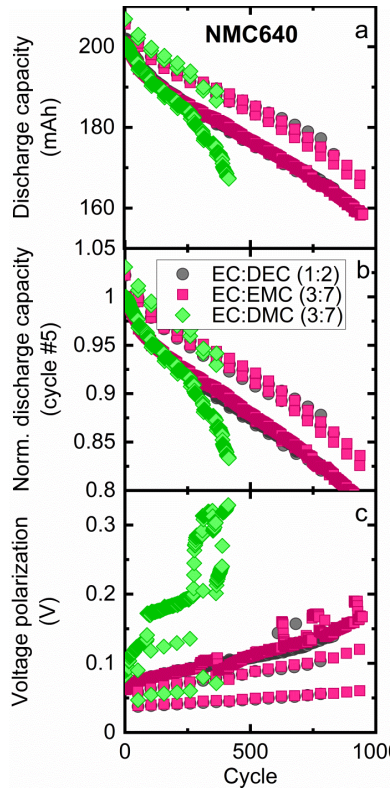

Figure 19. Discharge capacity (a), normalized discharge capacity (b), and normalized voltage polarization (c) for SC NMC640/AGC with EC:DEC (1:2) (grey circles), EC:EMC (3:7) (red squares), and EC:DMC (3:7) (green diamonds) cycling C/3 CCCV at 85 °C between 3.0 and 4.0 V. The electrolyte salt was 1 M LiFSI, the additives were 2 wt% VC and 1 wt% DTD. The second set of sparse data points is the C/20 check-up cycle data, which lies above the C/3 data points in the case of capacity and below the C/3 data points in the case of voltage polarization.[VI]

Figure 20 shows the absolute capacity (a–c), capacity normalized to the 5th cycle (d–f), and the voltage polarization (g–i) of cells cycled at 100 °C, plotted against cycling time. The cells were tested to three different UCVs: 3.9 V (a, d, g), 4.0 V (b, e, h), and 4.1 V (c, f, i). Notably, NMC640/AGC cells using EC:DEC (1:1) as the solvent blend, LiFSI and LiTFSI as salts, 2 wt% VC 1 wt% DTD as additives, achieved ~600 cycles (approximately six months) before reaching 80% capacity when cycled up to 4.0 V. Achieving such longevity at 100 °C with a liquid electrolyte is exceptionally difficult for conventional Li-ion batteries.[180]

The best salt composition is a 1:1 molar blend of LiFSI and LiTFSI, with pure LiFSI as the next best. The latter reached 80% capacity at just over 400 cycles at 100 °C and cycling to 4.0 V. Blending with $LiPF_6$ did not improve performance, except at 4.1 V, where it was comparable to the LiFSI + LiTFSI blend. Interestingly, despite pure LiTFSi causing severe aluminum corrosion on the positive

electrode current collector at such voltages and temperatures, blend with LiFSI still lead to the best-performing cells[123,125] Excessive gas production introduced noise in the pure LiFSI data and rapid cell venting at 4.1 V. For both pure LiFSI and its blends, no significant differences in capacity retention or voltage polarization were observed when cycling to 3.9 V or 4.0 V. However, when cycling to 4.1 V, the cells fail rapidly either due to venting (pure LiFSI) or due to rapid capacity fade (the salt blends). While capacity retention at elevated temperature is impressive, all configurations experienced notable impedance growth, including the 0.5 M LiFSI + 0.5 M LiTFSI blend at 3.9 and 4.0 V (g–h).

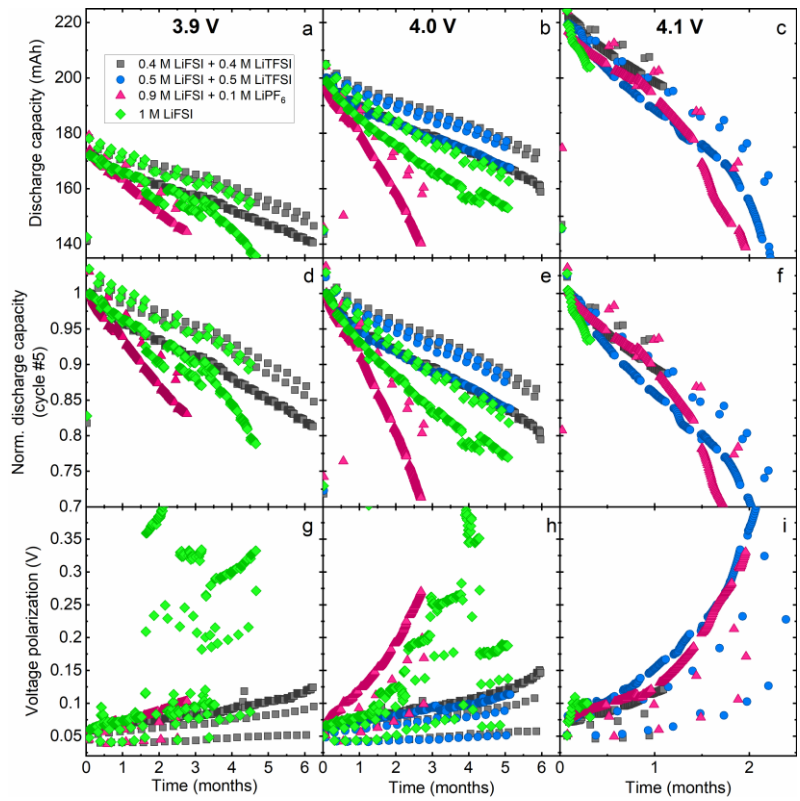

Figure 20. Discharge capacity (a-c), normalized discharge capacity (d-f), and voltage polarization (g-i) for single crystal NMC640/AGC cells cycling between 3.0−3.9 V (a, d, g), 3.0−4.0 V (b, e, h), or 3.0−4.1 V (c, f, i) at C/3 and 100 °C. These cells use EC:DEC (1:1) as the solvent blend and 2 wt% VC and 1 wt% DTD as additives. The salts used are 0.4 M LiFSI + 0.4 M LiTFSI (dark grey squares; 595 cycles at 3.9 V, 585 cycles at 4.0 V, 102 cycles at 4.1 V), 0.5 M LiFSI + 0.5 M LiTFSI (blue circles; 503 cycles at 4.0 V, 272 cycles at 4.1 V), 0.9 M LiFSI + 0.1 M $LiPF_6$ (red triangles; 297 cycles at 3.9 V, 314 cycles at 4.0 V, 224 cycles at 4.1 V) and 1 M LiFSI (green diamonds; 427 cycles at 3.9 V, 514 cycles at 4.0 V, 28 cycles at 4.1 V). The second set of sparse data points is the C/20 check-up cycle data, which lies above the C/3 data points in the case of capacity and below the C/3 data points in the case of voltage polarization.[IV]

Figure 21 shows *ex-situ* gas volume measurement results for UHPC cells. These cells exhibit minimal gassing over an extended period of time, even at 100 °C. NMC640 has no issues with gassing even at 4.0 V, whereas Ni83/AGC cells eventually vent at 3.8 V and 85 °C.

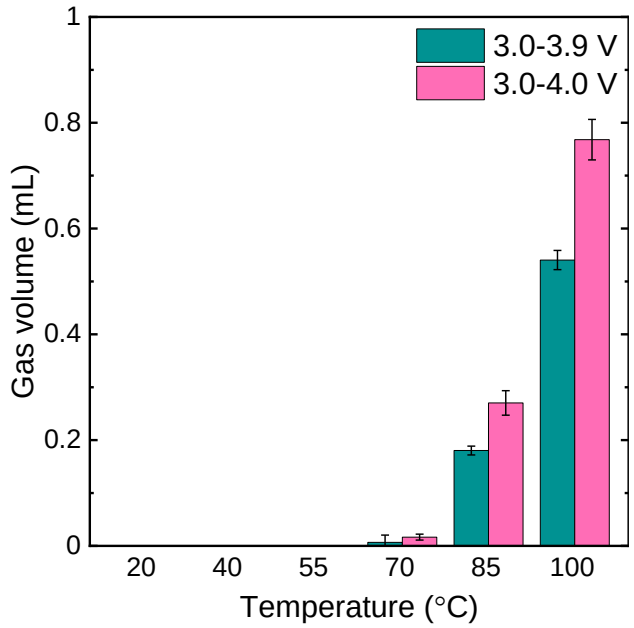

Figure 21. The volume of gas produced in SC NMC640/AGC pouch cells after 30 UHPC cycles (1200 h of testing) at C/20 and at various temperatures. No detectable gas was produced in the UHPC experiment between 20 to 55 °C.[IV]

Figure 22 presents quantified μXRF data from the negative electrodes of selected cells cycled under extreme conditions alongside comparator cells with 1 M LiTFSI that failed rapidly. Although LiFSI is typically associated with Al corrosion at elevated voltages, no Al corrosion was detected, even at high temperatures and a cutoff voltage of 4.1 V. In contrast, using pure LiTFSI under the same conditions led to severe Al corrosion, resulting in immediate cell failure. Expectedly,[181] no detectable Mn was found on the negative electrodes of low-voltage cells (≤ 4.0 V). However, cycling to 4.1 V induced Mn dissolution from the positive electrode and its subsequent deposition on the negative electrode. This suggests structural damage to the cathode and aligns with the observed decline in cycling performance at 4.1 V, including reduced capacity retention and increased voltage polarization, relative to cells cycled to 4.0 V. While cells using the LiFSI and LiTFSI blend significantly outperformed those using pure LiFSI, Mn dissolution was still present. This indicates that the underlying degradation mechanism is not fully suppressed. The full cause and effect of Mn dissolution remain unclear. However, it can be concluded that SC NMC640/AGC cells with EC:DEC (1:1) 1 M LiFSI 2 wt% VC and 1 wt% DTD cells exhibit no Al corrosion and

very limited gas production and Mn deposition even under the most extreme conditions.

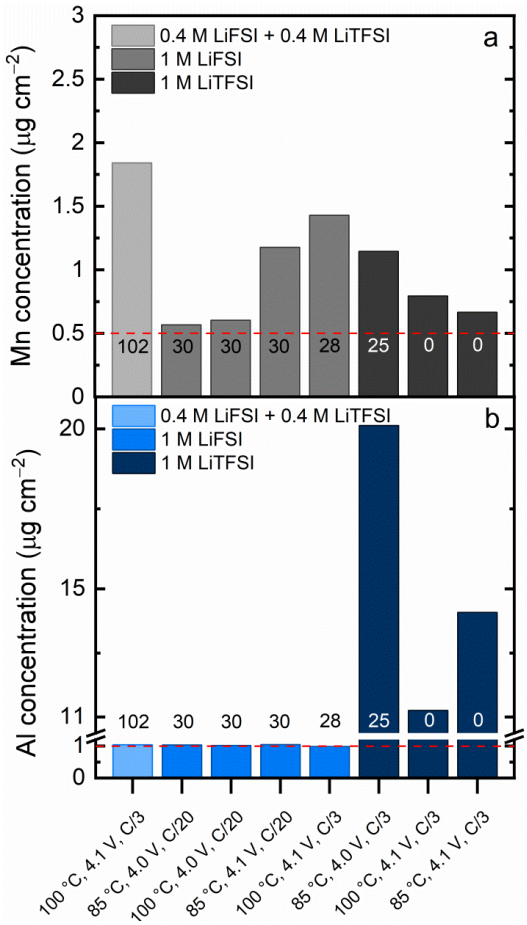

Figure 22. Post-mortem Mn (a, grey) and Al (b, blue) concentration on the negative electrode of NMC640/AGC cells cycled at C/3 or C/20 at 85 or 100 °C. The number overlayed or on top of bars is the number of cycles performed. Cells using 1 M LiTFSI as electrolyte salt that vented and failed rapidly when tested at the indicated conditions have been added for comparison. The dashed red line represents signal values obtained from measuring the negative electrode of a dry, uncycled cell.[IV]

6.2.2. Limitations of Li-ion pouch cells for accelerated testing and long-lifetime cells

The importance of the form factor was studied in publication VI.

Figure 23 shows the electrolyte loss rates for various solvent mixtures used in pouch cells subjected to wide-temperature UHPC experiments. In all cases, the electrolyte contained 1 M LiFSI as the salt with 2 wt% VC and 1 wt% DTD as

the additives. The data exhibits an Arrhenius-type dependence of the solvent loss rate, highlighting that solvent permeation is a relevant issue even at moderate temperatures. While reduced at lower temperatures, solvent loss over decades may still cause solvent depletion in long-lifetime cells leading to failure prior to their electrochemical end-of-life.

A correlation is observed between solvent composition and loss rate: blends with higher fractions of DEC or DMC exhibit greater solvent loss. This suggests that the more volatile solvents, DEC and DMC, are the primary components lost over time.

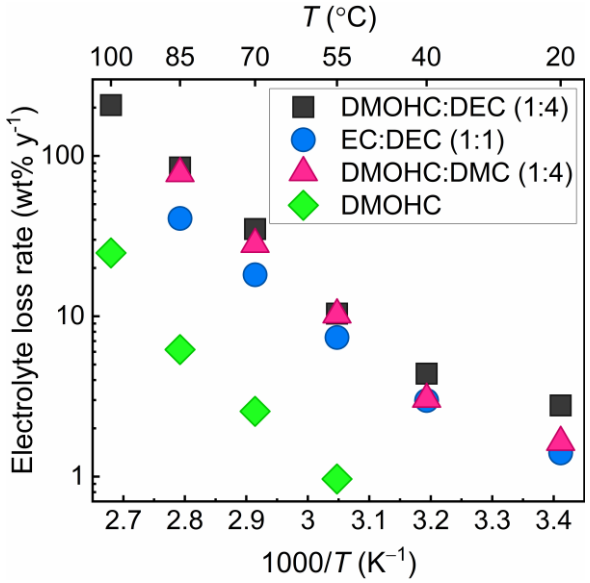

Figure 23. Electrolyte loss rate at different temperatures for polycrystalline Ni83/AGC 402035-size pouch cells cycled C/20 between 3.0–3.8 V and 3.0–3.9 V for ~1500 h. Solvent blends used were DMOHC:DEC (1:4) (black squares), EC:DEC (1:1) (blue circles), DMOHC:DMC (1:4) (red triangles), and DMOHC (green diamonds). The electrolyte salt was 1 M LiFSI, and additives were 2 wt% VC and 1 wt% DTD. The values were calculated by dividing the total cell mass loss by cycling time.[V]

Figure 24 shows the electrolyte loss rates for pouch cells, 18650 cans, and 18650 cells with and without Torr-seal under both storage and cycling conditions in a temperature-controlled environment. The electrolyte loss rate at 70–100 °C is substantial exceeding 10 wt% per year in most cases. Pouch cells particularly reach 60 wt% per annum. At such rates, even if a cell could maintain 80% capacity for one year, failure due to electrolyte depletion would likely occur before reaching electrochemical end-of-life.

It is evident that the 18650s have an inherent advantage as the solvent loss rate is reduced by a factor of 1.3 to 3 compared to pouch cells. The application of Torr-seal further reduces loss in both form factors, cutting it by approximately

half at 100 °C. However, this additional sealing appears most beneficial for 18650s only at the highest temperatures, as their loss rates at lower temperatures are relatively comparable. This is another advantage for the 18650s, as fewer additional resources and processes are required to achieve better retention and a more stable cell.

The discrepancy between electrolyte loss data of uncycled cells and cans vs cycled cells is most probably due to differences in test configuration. The "un-cycled" 18650s in panel a consist of empty cans without electrodes and contain roughly half the electrolyte volume of a real cell. Additionally, in the case of both the pouch cells and 18650s the uncycled cell data is averaged over 10 cells or cans vs 2 cycled cells. Pouch cells also show more variability due to their smaller mass and greater operator influence during filling and sealing. Therefore, the 18650s provide a more stable system over a long duration of time and in a wide temperature range, enabling more representative lifetime predictions.

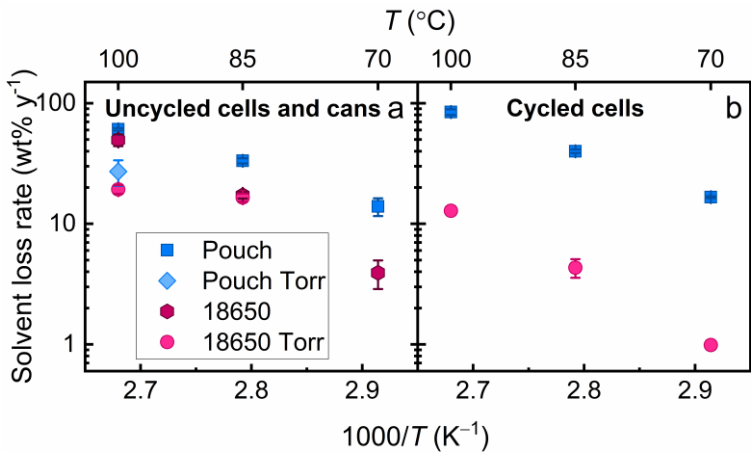

Figure 24. (a) The solvent loss rate of pouch (blue) with (diamonds) and without (squares) Torr Seal and 18650 cylindrical cans (red) with (circles) and without (hexagons) Torr Seal kept at constant temperatures indicated. (b) SC NMC640/AGC pouch cells (blue squares) and Torr-sealed 18650 cylindrical cells (red circles) cycled C/20 in a wide temperature range between 3.0–3.9 V for the pouch and 3.0–4.0 V for the 18650 cells. In panel a, all cells were filled with EC:DEC (1:1). In panel b, the solvent blend in pouch cells was EC:DEC (1:1), and in the 18650s, it was EC:DEC (1:2). The salt was 1 M LiFSI and the additives were 2 wt% VC 1 wt% DTD. The solvent loss values are calculated by dividing the fractional solvent mass loss by the total time spent in the temperature box. Error bars express (a) standard error or (b) standard deviation where multiple datapoints are available.[V]

Figure 25 shows normalized cycling and voltage polarization data for a pouch cell, Torr-sealed pouch cells, and a Torr-sealed 18650 cell using EC:DEC (1:2) 1 M LiFSI 2 wt% VC 1 wt% DTD as electrolyte and cycled at C/3 at 85 °C. Interestingly, pouch cells without Torr-seal outperform their Torr-sealed counterparts. The 18650 cell demonstrates superior performance, retaining approximately 91% capacity after 830 cycles (~7 months), compared to pouch cells retaining 85%, 82%, and 79% capacity for the unsealed pouch cell and two Torr-sealed pouch cells (A and B), respectively.

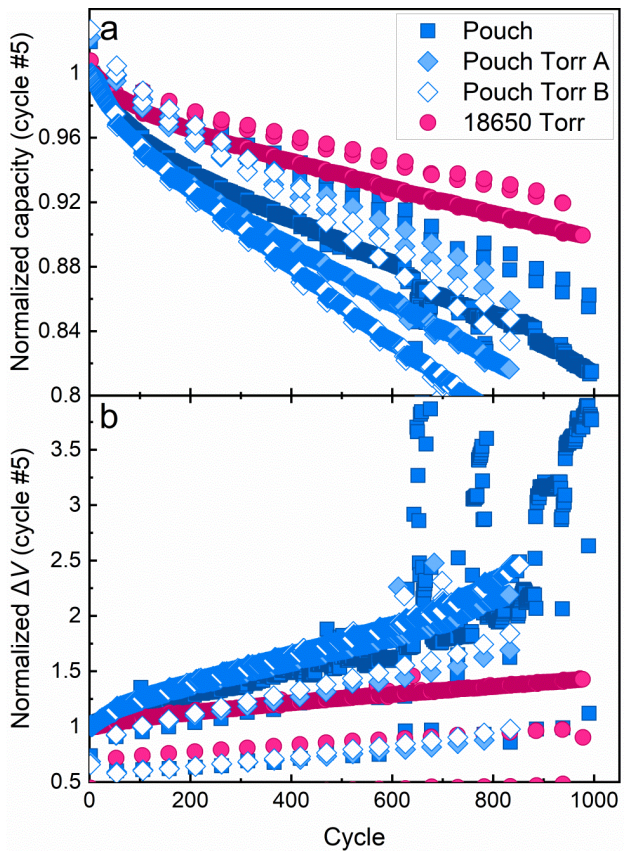

Figure 25. Normalized discharge capacity (a) and normalized voltage polarization (b) for SC NMC640/AGC pouch cells with (filled and unfilled light blue diamonds) and without (blue squares) Torr Seal and 18650 cylindrical cells with Torr Seal (red circles) cycling C/3 at 85 °C from 3.0 V to 4.0 V. These cells use EC:DEC (1:2) as the solvent blend, 1 M LiFSI as the salt, and 2 wt% VC 1 wt% DTD as additives. The second set of sparse data points is the C/20 check-up cycle data, which lies above the C/3 data points in the case of capacity and below the C/3 data points in the case of voltage polarization. The absolute capacities at cycle 800 are as follows: 169 mAh for "Pouch" (blue squares), 166 mAh for "Pouch Torr A" (filled blue diamonds) and 157 mAh for "Pouch Torr B" (unfilled blue diamonds), and 1753 mAh for "18650 Torr" (red circles).[V]

These differences in capacity retention likely stem from the Torr-sealing and the resulting differences in electrolyte loss. Assuming solvent loss only, the absolute amount of salt remaining in the cell remains constant. This has very recently been shown to be true, with salt consumption having a more minor effect compared to solvent loss.[182] Thus, the salt concentration is increasing. Cycle-hold experiments have demonstrated a positive correlation between increased LiFSI concentration and capacity retention, while impedance growth remains unaffected.[183]

Measured electrolyte loss was 23% for Torr-sealed cell A, 21% for Torr-sealed cell B, and 32% for the unsealed pouch cell. A back-of-the-envelope calculation suggests the salt molarity increased from 1 M to roughly 1.37 M for cell A, 1.33 M for cell B, and 1.60 M for the cell without Torr-seal. The cell that has lost the most electrolyte, and thus has the highest salt concentration, is the best-performing. This suggests the cell without Torr Seal will perform better until it dries out and ultimately fails. The Torr-sealed cells are expected to cycle well past that point due to reduced solvent loss.

The 18650 cell, demonstrates itself to be the superior form factor when it comes to both capacity retention and lower voltage polarization. Furthermore, the Torr-sealed 18650 cell has lost only 2% of its electrolyte. A head-to-head comparison of pouch to 18650 is unfair, considering the significant differences in geometry and capacity. These effects range from the testing aspects, e.g., lower uncertainties due to increased capacities, to the mechanics of the cell, e.g., the far smaller ratio of overhang to active negative electrode area in the case of 18650. Overall, it is important to note how strongly these uncontrolled and unwanted changes in electrolyte composition affect cell performance. This makes cells with changing electrolyte compositions unpredictable.

6.2.3. Development of a lifetime model

The development of an initial lifetime model was done on pouch cells using NMC640/AGC with EC:DEC (1:1) 1 M LiFSI 2 wt% VC 1 wt% DTD. Though pouch cells have their limitations (as per chapter 6.2.2.), this was deemed a simple, well-performing, and repeatable system to perform initial development work on. This initial work is featured in publication IV.

Figure 26 demonstrates the validity of Eq. 4. It is clear that the mathematical relation established there – CIE is the sum of fractional fade and fractional slippage – holds up with real data (panels c and d). Eq. 4 does not match well at the lowest temperatures (10 °C and 20 °C) due to the difficulty of maintaining those temperatures at the required temperature stability (± 0.1 °C), the low capacity values increasing the impact of relative uncertainty, and the cells taking longer to reach an equilibrium state at lower temperatures. On panels a and b, the effects of temperature on the discharge capacity are apparent, with low-temperature capacities significantly lower than capacity at 40 °C. Even though the current is very low (C/20), capacities increase with temperature. The cells running to 3.9 V at 100 °C and 4.0 V at 85 and 100 °C do not follow this trend, as degradation is noticeably accelerated at the most extreme conditions.

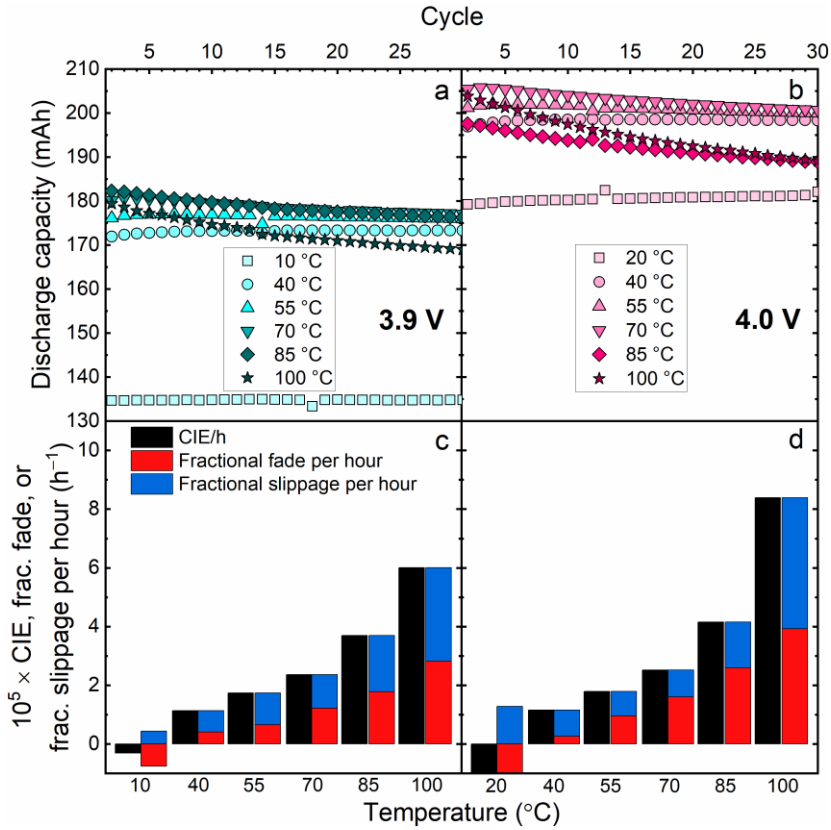

Figure 26. Discharge capacity (a-b) and coulombic inefficiency per hour, fractional capacity fade per hour, and fractional charge endpoint slippage per hour (c-d) for UHPC measurements done on SC NMC640/AGC pouch cells with EC:DEC (1:1) 1 M LiFSI 2 wt% VC 1 wt% DTD cycling C/20 between 3.0–3.9 V (a, c) and 3.0–4.0 V (b, d) at 20–100 °C. Bar heights in panels c and d represent the projected value at the 29th cycle based on a linear fit of cycles 26–29. The 30 cycles shown took 1200 hours to measure.[IV]

Figure 27 shows the same UHPC characteristics as Figure 26 as an Arrhenius (a, c, e) or linear (b, d, f) scatter plot. It is visible that although at temperatures up to 70 °C the fade and CIE seem to be increasing linearly (b and f), if the entire temperature range is observed, it follows more of an exponential trend, considering the linearity of the points on the logarithmic plot (a and e). This is consequential as studies have often limited themselves to 60 °C, due to technical challenges of operating Li-ion cells at ≥ 60 °C. Both slippage and fade increase with temperature, although the correlation is far stronger with fade. Though charge endpoint slippage (c-d) exists and is on the same order of magnitude as capacity fade at all temperatures, the exact cause of this is unknown. What is more, its relation to temperature is unclear, as it does not follow a linear or exponential trend.

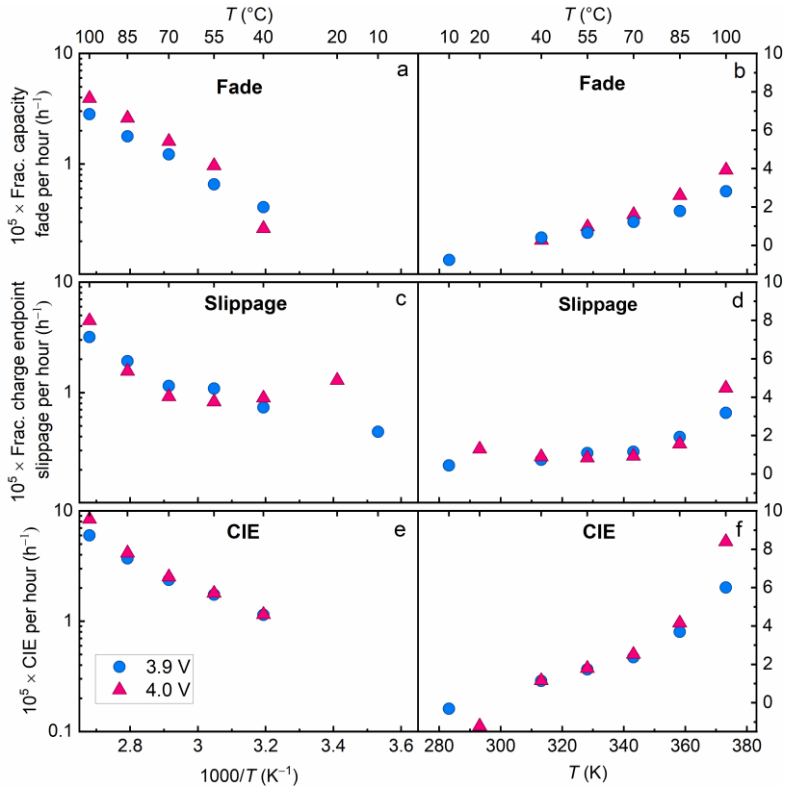

Figure 27. Fractional capacity fade per hour (a–b), fractional charge endpoint slippage per hour (c–d), and coulombic inefficiency per hour (e–f) for UHPC measurements done on SC NMC640/AGC pouch cells with EC:DEC (1:1) 1 M LiFSI 2 wt% VC 1 wt% DTD cycling at C/20 between 3.0−3.9 V or 3.0−4.0 V at 20–100 °C. On panels a, c, and e, the *y*-axis is logarithmic, and the *x*-axis is the inverse of absolute temperature, while on panels b, d, and f, both axes are linear. Fade and CIE were negative at 10 and 20 °C, so they are not visible on the logarithmic plots (a, e), and fade for 20 °C is out of scale in panel b.[IV]

In order to use the acquired metrics for lifetime predictions, A must be extracted from Eq. 6. That is most easily done by plotting, $\frac{Q(t)}{Q_0}$ vs $\sqrt[2]{t}$.* If the parabolic law applies, the resultant curve should be linear, and the A value can be extracted from the slope. This is done in Figure 28. What is also apparent in Figure 28 is that there are deviations from linearity that are caused mainly by power outages that occurred during the experiment and the limitations in data quality offered by small-capacity pouch cells.

* It is important to note that the analysis and its results in this thesis differ from those presented in publication IV. The A values (denoted B in the publication) were previously extracted incorrectly, with fractional capacity fade rates used. Thus, the analysis in this thesis has been further elaborated and corrected.

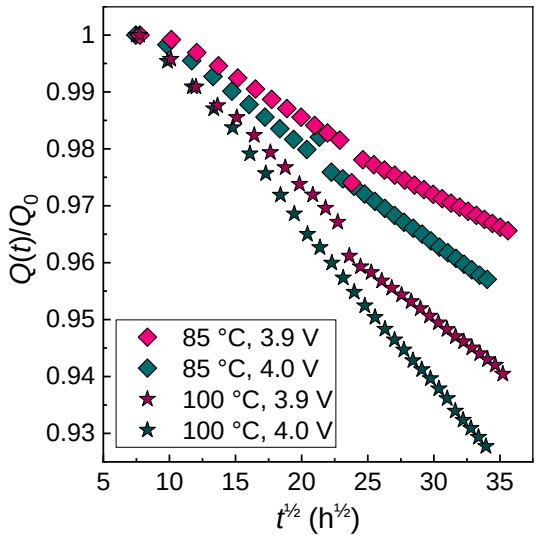

Figure 28. Fractional capacity vs square root time of SC NMC640/AGC pouch cells with EC:DEC (1:1) 1 M LiFSI 2 wt% VC 1 wt% DTD cycling at C/20 between 3.0−3.9 V or 3.0−4.0 V at 85 and 100 °C. From their slopes, *A* values are extracted.

Using the *A* parameters extracted from Figure 28, Eq. 8 can be applied to real long-term C/3 CCCV cycling data to check the validity of this simple model. Using the lifetimes acquired from 100 °C cycling data in Figure 20 and calculating projected lifetimes for similar cells cycling at 85 °C (as seen in, for example, Figure 17), the results can be compared to the lifetimes measured at 85 °C. Table 1 presents the results of these projections. It took 1240 h (~1.7 months) for a 1 M LiFSI cell cycling to 4.0 V at 100 °C (A_{100} = 0.002244) to reach ~89.7% capacity, it should take a cell cycling at 85 °C (A_{85} = 0.001318) about $(1.70)^2$ times longer or 3420 h (~4.8 months) to do the same, based on the Arrhenius-type relationship. The relative error of this projection is only an exceptional 1%. The cell cycling to 3.9 V at 85 °C reached ~82.2% capacity retention after 8325 h (~11.6 months) of cycling, compared to the predicted 8988 h (~12.5 months, 8% relative error). Although these two predictions are within reasonable error (≤ 10%), the prediction of the cell cycling to 3.9 V and 92.4% capacity is 20% off.

Table 1. Projected cycling times compared to actual measured cycling times necessary to reach specific fractional capacity values for NMC640/AGC cells using EC:DEC (1:1) 1 M LiFSI 2 wt% VC 1 wt% DTD cycling C/3 at the temperatures and to the UCVs indicated. The lower cut-off voltage was 3.0 V in all cases. The *A* values needed to apply Eq. 8 were obtained from the linear slopes of Figure 28.

UCV [V]	Fractional capacity	Cycling time at 100 °C [h]	Projected cycling time at 85 °C [h]	Cycling time at 85 °C [h]	Relative error of projection
3.9	0.924	1181	3420	2846	20%
3.9	0.822	3102	8988	8325	8%
4.0	0.897	1240	3420	3378	1%

There are three main causes of error.

1. The square root time model currently only considers Li inventory loss at low rates. When calculating lifetimes for cells cycling at C/3, other factors need to be considered, as, for example, cell impedance starts to grow and factor in, as visible in Figure 20g–20i. All three of the presented predictions overestimate the lifetimes of the cells. Therefore, the causes and effects of this should be included in future work.
2. Electrolyte permeation out of the pouch cells changes their properties and affects their performance.
3. The quality of data from the pouch cells may not be sufficient. This is due to the low capacity of the cells and the effects of power outages on the measurements. Furthermore, insufficient data is presented here for validation, with a single outlier cell possibly skewing the results.

However, the power of these kinds of predictions should not be underestimated, and there are easy steps to take that can already negate these issues, e.g., switching to 18650 cylindrical cells with Torr seal.

If one were to take the most accurate lifetime prediction – based on the cell cycling to 4.0 V at 100 °C – and project the lifetime of the same cell cycling to 40 °C, the cell would reach 89.7% capacity in 40 years, and 82.2% in an impressive 85 years. However, in addition to the lack of necessary additional validation of these predictions, we already know from chapter 6.2.2. that (without Torr seal) these cells would lose 30% of their electrolyte in 16 years, likely drying out and failing long before reaching these lifetimes.

6.2.4. Further development

There are many propositions for further improvement in this thesis that have already been applied. The work presented here was the forerunner of the results published in Claire Floras *et al* 2025 J. Electrochem. Soc. 172 020514.[184] They used cylindrical 18650 cells with NMC640, NMC631, or NMC60:35:10 as the positive electrode, artificial graphite as the negative, and EC:DEC 1:2 1 M LiFSI 2 wt% VC 1 wt% DTD as the electrolyte. All cells had also Torr seal applied to them and were cycled to 4.0 V. There are several key takeaways already available to researchers based on that work.

- The cells went through thorough physical and electrochemical characterisation, and it was confirmed that the primary degradation mechanism at C/20 was Li inventory loss due to SEI layer growth. The cells exhibited severely reduced solvent permeation, no transition metal deposition, no gas production, no electrolyte oxidation or unexpected degradation product, nor significant salt loss.
- The high quality of the data enabled further development and validation of the square root time model.
- At C/3, the necessity to either include impedance growth in the model or mitigate it in the cell became apparent and remains one of the directions for further development.

6.3. Benefits and efficacy of advanced techniques for energy storage

Advanced techniques such as neutron powder diffraction (NPD), ultra-high precision coulometry (UHPC), and elevated temperature testing provided critical insights into the performance and limitations of solid-state hydrogen storage in $NaAlH_4$/carbon composites and long-lifetime lithium-ion battery systems. These methods deepened our understanding of the fundamental behaviors of these technologies, supporting the development of more efficient H_2 storage solutions and robust predictive models for Li-ion batteries.

NPD enabled the *in-situ* study of the $NaAlH_4$/carbon black composites during dehydrogenation and hydrogenation cycling. This made it possible to observe structural and chemical changes in real time under operating conditions. The results demonstrated that dehydrogenation/hydrogenation cycling was possible at relatively mild conditions (150 °C, 20 bar H_2 pressure). Furthermore, they suggested that the inherent chemical nature of the carbon material, in addition to its mesoporous and nanoparticulate structure, likely contributed to improved performance. Most crucially, NPD revealed the composite's limitations. As an H_2 storage material, it remains hindered by the segregation of its decomposition products and does not fully rehydrogenate to $NaAlH_4$, returning mostly to the intermediate Na_3AlH_6. As a result, tailoring the carbon material's structure and including catalysts should be pursued in the future.

Wide-temperature range UHPC combined with accelerated testing at elevated temperatures enabled a detailed evaluation of the degradation behavior of Li-ion cells at elevated temperatures. With the degradation mechanisms in these well-optimized cells limited primarily to Li inventory loss, a straightforward lifetime model was developed using this high-precision data. While this initial model does not yet account for impedance growth, it demonstrates how decades of real-world aging can be predicted with moderate testing time. Furthermore, this has already enabled continued work further developing and validating the cells and model. This is a potentially transformative tool for warranty modeling, system design, and second-life battery applications.

Although NPD and UHPC were applied to different storage technologies in this work, the potential for integrated *operando* studies is compelling. For example, once a hypothesis is established regarding the root cause of impedance growth in these Li-ion cells, e.g., degradation of the positive electrode, combined NPD and electrochemical testing could be employed to directly confirm or refute it. This integrative approach represents a powerful future direction for diagnosing and optimizing advanced energy storage systems.

7. SUMMARY

The energy crisis following the Russian invasion of Ukraine has accelerated the EU's shift toward energy independence and clean energy adoption. Initiatives such as REPowerEU and Fit for 55 aim to reduce reliance on fossil fuels, energy imports, and cut emissions. Renewable energy sources are crucial to achieving these goals. However, sustainable energy storage solutions are critical to integrate renewables into the energy market. Lithium-ion batteries dominate short-term energy storage due to their energy density, efficiency, and maturity, but face limitations in sustainability, raw material sourcing, and long-duration storage capability. These issues could be mitigated by extending battery lifetimes and using them in second-life applications. Hydrogen, produced from renewables via electrolysis, offers a promising solution for long-term and seasonal storage, though current storage technologies struggle with safety, efficiency, and cost.

This thesis investigates solid-state H_2 storage in sodium alanate ($NaAlH_4$) and long-lifetime Li-ion batteries. They are characterized by standard lab-based techniques, such as PXRD, gas adsorption, CCCV cycling, etc. However, significant insights are gained through advanced techniques: neutron powder diffraction (NPD) that reveals *in-situ* phase transitions of $NaAlH_4$ composites, while ultra-high precision coulometry (UHPC) combined with accelerated aging tests at elevated temperatures is used to study Li-ion battery degradation.

To improve its hydrogen storage properties, $NaAlH_4$ was nanostructured via ball milling with mesoporous carbon black, enabling confinement within nanopores, between particles, and possibly as thin films on carbon surfaces. This significantly reduced dehydrogenation temperatures: hydrogen release began at 100 °C for 50 wt% $NaAlH_4$ composites, compared to 183 °C for bulk $NaAlH_4$. It also enabled partial rehydrogenation at 150 °C and 20 bar. However, full reversibility remains hindered by phase segregation, indicating that further optimization of the carbon scaffold and inclusion of catalysts could enhance performance.

Li-ion cells were optimized for high-temperature (60–100 °C) performance by carefully studying and choosing components such as positive electrode materials, electrolyte solvents, salts, additives, and cell form factors. 402035 pouch cells using NMC640/artificial graphite EC:DEC (1:1) 1 M LiFSI 2 wt% VC 1 wt% DTD showed promising results, but suffered from electrolyte loss through seals at elevated temperatures. Cylindrical 18650 cells combined with an epoxy sealant showed improved stability, which can be applied to future development. UHPC testing across a wide temperature range revealed Arrhenius-type degradation behavior, allowing application of a square-root time model to predict long-term capacity fade. Although this model does not yet account for all aspects affecting Li-ion cells and suffers from limited data quality, it offers a foundational approach to lifetime prediction, enabling extended battery warranties and second-life use.

8. REFERENCES

(1) IEA. *World Energy Outlook 2024*; IEA: Paris, 2024. https://www.iea.org/reports/world-energy-outlook-2024.

(2) *Fit for 55*. European Council, Council of the European Union. https://www.consilium.europa.eu/en/policies/fit-for-55/ (accessed 2025-05-21).

(3) Liu, J.; Huang, Z.; Fan, M.; Yang, J.; Xiao, J.; Wang, Y. Future Energy Infrastructure, Energy Platform and Energy Storage. *Nano Energy* **2022**, *104*, 107915. https://doi.org/10.1016/j.nanoen.2022.107915.

(4) Sharmili, N.; Nagi, R.; Wang, P. A Review of Research in the Li-Ion Battery Production and Reverse Supply Chains. *Journal of Energy Storage* **2023**, *68*, 107622. https://doi.org/10.1016/j.est.2023.107622.

(5) Koohi-Fayegh, S.; Rosen, M. A. A Review of Energy Storage Types, Applications and Recent Developments. *Journal of Energy Storage* **2020**, *27*, 101047. https://doi.org/10.1016/j.est.2019.101047.

(6) Luo, X.; Wang, J.; Dooner, M.; Clarke, J. Overview of Current Development in Electrical Energy Storage Technologies and the Application Potential in Power System Operation. *Applied Energy* **2015**, *137*, 511–536. https://doi.org/10.1016/j.apenergy.2014.09.081.

(7) Dowling, J. A.; and Lewis, N. S. Long-Duration Energy Storage for Reliable Renewable Electricity: The Realistic Possibilities. *Bulletin of the Atomic Scientists* **2021**, *77* (6), 281–284. https://doi.org/10.1080/00963402.2021.1989191.

(8) *Toward security in sustainable battery raw material supply | McKinsey*. https://www.mckinsey.com/industries/metals-and-mining/our-insights/toward-security-in-sustainable-battery-raw-material-supply (accessed 2025-05-22).

(9) Sovacool, B. K. The Precarious Political Economy of Cobalt: Balancing Prosperity, Poverty, and Brutality in Artisanal and Industrial Mining in the Democratic Republic of the Congo. *The Extractive Industries and Society* **2019**, *6* (3), 915–939. https://doi.org/10.1016/j.exis.2019.05.018.

(10) Aiken, C. P.; Taskovic, T.; Dahn, J. R. Improved Li-Ion Cell Construction and Usage Scheme for Achieving Operation Beyond End-of-Life. *J. Electrochem. Soc.* **2022**, *169* (9), 090523. https://doi.org/10.1149/1945-7111/ac91ac.

(11) *Fit for 55: shifting from fossil gas to renewable and low-carbon gases*. European Council, Council of the European Union. https://www.consilium.europa.eu/en/infographics/fit-for-55-hydrogen-and-decarbonised-gas-market-package-explained/ (accessed 2025-05-21).

(12) Bachlechner, P.; Hofer, R.; Jarru, T.; Kaendler, F.; Lorentz, A.; Signorini, M. *Can Green Hydrogen Meet the Needs for the EU Green Industrial Development?*. The European Chair for Sustainable Development and Climate Transition. https://webserver07.reims.sciences-po.fr/psia/chair-sustainable-development/2025/05/16/can-green-hydrogen-meet-the-needs-for-the-eu-green-industrial-development/ (accessed 2025-05-21).

(13) Widera, B. Renewable Hydrogen Implementations for Combined Energy Storage, Transportation and Stationary Applications. *Thermal Science and Engineering Progress* **2020**, *16*, 100460. https://doi.org/10.1016/j.tsep.2019.100460.

(14) *Tech descriptions*. Hydrogen Europe. https://hydrogeneurope.eu/tech-descriptions/ (accessed 2025-05-22).

(15) Mulky, L.; Srivastava, S.; Lakshmi, T.; Sandadi, E. R.; Gour, S.; Thomas, N. A.; Shanmuga Priya, S.; Sudhakar, K. An Overview of Hydrogen Storage Technologies – Key Challenges and Opportunities. *Materials Chemistry and Physics* **2024**, *325*, 129710. https://doi.org/10.1016/j.matchemphys.2024.129710.

(16) Hydrogen-Based Autonomous Energy Supply System H_2One^{TM} One Container Model. https://www.global.toshiba/content/dam/toshiba/migration/energysolution/ess/hydrogen/file/H2One_Leaflet_EN.pdf?utm_source=www&utm_medium=web&utm_campaign=since202202ess (accessed 2025-05-22).

(17) Kwon, K.; Lee, H.-B.; Kim, N.; Park, S.; Joshua, S. R. Integrated Battery and Hydrogen Energy Storage for Enhanced Grid Power Savings and Green Hydrogen Utilization. *Applied Sciences* **2024**, *14* (17), 7631. https://doi.org/10.3390/app14177631.

(18) Osman, A. I.; Ayati, A.; Farrokhi, M.; Khadempir, S.; Rajabzadeh, A. R.; Farghali, M.; Krivoshapkin, P.; Tanhaei, B.; Rooney, D. W.; Yap, P.-S. Innovations in Hydrogen Storage Materials: Synthesis, Applications, and Prospects. *Journal of Energy Storage* **2024**, *95*, 112376. https://doi.org/10.1016/j.est.2024.112376.

(19) Varin, R. A.; Czujko, T.; Wronski, Z. S. *Nanomaterials for Solid State Hydrogen Storage*; Fuel Cells and Hydrogen Energy; Springer US: Boston, MA, 2009. https://doi.org/10.1007/978-0-387-77712-2.

(20) Jepsen, L. H.; Paskevicius, M.; Jensen, T. R. Nanostructured and Complex Hydrides for Hydrogen Storage. In *Nanotechnology for Energy Sustainability*; WILEY-VCH Verlag GmbH & Co KGaA: Weinheim, Germany, 2017; Vol. 2, pp 415–432.

(21) Ren, J.; Musyoka, N. M.; Langmi, H. W.; Mathe, M.; Liao, S. Current Research Trends and Perspectives on Materials-Based Hydrogen Storage Solutions: A Critical Review. *Int. J. Hydrogen Energy* **2017**, *42* (1), 289–311. https://doi.org/10.1016/j.ijhydene.2016.11.195.

(22) Bellosta von Colbe, J.; Ares, J.-R.; Barale, J.; Baricco, M.; Buckley, C.; Capurso, G.; Gallandat, N.; Grant, D. M.; Guzik, M. N.; Jacob, I.; Jensen, E. H.; Jensen, T.; Jepsen, J.; Klassen, T.; Lototskyy, M. V.; Manickam, K.; Montone, A.; Puszkiel, J.; Sartori, S.; Sheppard, D. A.; Stuart, A.; Walker, G.; Webb, C. J.; Yang, H.; Yartys, V.; Züttel, A.; Dornheim, M. Application of Hydrides in Hydrogen Storage and Compression: Achievements, Outlook and Perspectives. *Int. J. Hydrogen Energy* **2019**, *44* (15), 7780–7808. https://doi.org/10.1016/j.ijhydene.2019.01.104.

(23) Fischer, M.; Werber, M.; Schwartz, P. V. Batteries: Higher Energy Density than Gasoline? *Energy Policy* **2009**, *37* (7), 2639–2641. https://doi.org/10.1016/j.enpol.2009.02.030.

(24) Weidenthaler, C.; Felderhoff, M. Complex Hydrides. In *Handbook of Hydrogen Storage*; John Wiley & Sons, Ltd, 2010; pp 117–157. https://doi.org/10.1002/9783527629800.ch5.

(25) Dematteis, E. M.; Amdisen, M. B.; Autrey, T.; Barale, J.; Bowden, M. E.; Buckley, C. E.; Cho, Y. W.; Deledda, S.; Dornheim, M.; de Jongh, P.; Grinderslev, J. B.; Gizer, G.; Gulino, V.; Hauback, B. C.; Heere, M.; Heo, T. W.; Humphries, T. D.; Jensen, T. R.; Kang, S. Y.; Lee, Y.-S.; Li, H.-W.; Li, S.; Møller, K. T.; Ngene, P.; Orimo, S.; Paskevicius, M.; Polanski, M.; Takagi, S.; Wan, L.; Wood, B. C.; Hirscher, M.; Baricco, M. Hydrogen Storage in Complex Hydrides: Past Activities and New Trends. *Prog. Energy* **2022**, *4* (3), 032009. https://doi.org/10.1088/2516-1083/ac7499.

(26) *CRC Handbook of Chemistry and Physics*, 97th ed.; Lide, D. R., Haynes, W. M. ., Bruno, T. J., Eds.; CRC Press: Boca Raton, London, New York, 2017.
(27) Milanese, C.; Garroni, S.; Gennari, F.; Marini, A.; Klassen, T.; Dornheim, M.; Pistidda, C. Solid State Hydrogen Storage in Alanates and Alanate-Based Compounds: A Review. *Metals* **2018**, *8* (8), 567. https://doi.org/10.3390/met8080567.
(28) Milanese, C.; Jensen, T. R.; Hauback, B. C.; Pistidda, C.; Dornheim, M.; Yang, H.; Lombardo, L.; Zuettel, A.; Filinchuk, Y.; Ngene, P.; de Jongh, P. E.; Buckley, C. E.; Dematteis, E. M.; Baricco, M. Complex Hydrides for Energy Storage. *Int. J. Hydrogen Energy* **2019**, *44* (15), 7860–7874. https://doi.org/10.1016/j.ijhydene.2018.11.208.
(29) Li, Y.; Zhou, G.; Fang, F.; Yu, X.; Zhang, Q.; Ouyang, L.; Zhu, M.; Sun, D. De-/Re-Hydrogenation Features of NaAlH4 Confined Exclusively in Nanopores. *Acta Mater.* **2011**, *59* (4), 1829–1838. https://doi.org/10.1016/j.actamat.2010.11.049.
(30) Zhao, L.; Xu, F.; Zhang, C.; Wang, Z.; Ju, H.; Gao, X.; Zhang, X.; Sun, L.; Liu, Z. Enhanced Hydrogen Storage of Alanates: Recent Progress and Future Perspectives. *Prog. Nat. Sci.* **2021**, *31* (2), 165–179. https://doi.org/10.1016/j.pnsc.2021.01.007.
(31) Palm, R.; Kurig, H.; Aruväli, J.; Lust, E. $NaAlH_4$/Microporous Carbon Composite Materials for Reversible Hydrogen Storage. *Microporous and Mesoporous Materials* **2018**, *264*, 8–12. https://doi.org/10.1016/J.MICROMESO.2017.12.027.
(32) Zheng, S.; Fang, F.; Zhou, G.; Chen, G.; Ouyang, L.; Zhu, M.; Sun, D. Hydrogen Storage Properties of Space-Confined $NaAlH_4$ Nanoparticles in Ordered Mesoporous Silica. *Chemistry of Materials* **2008**, *20* (12), 3954–3958. https://doi.org/10.1021/cm8002063.
(33) Baldé, C. P.; Hereijgers, B. P. C.; Bitter, J. H.; Jong, K. P. de. Sodium Alanate Nanoparticles − Linking Size to Hydrogen Storage Properties. *Journal of the American Chemical Society* **2008**, *130* (21), 6761–6765. https://doi.org/10.1021/ja710667v.
(34) Bhakta, R. K.; Maharrey, S.; Stavila, V.; Highley, A.; Alam, T.; Majzoub, E.; Allendorf, M. Thermodynamics and Kinetics of $NaAlH_4$ Nanocluster Decomposition. *Phys. Chem. Chem. Phys.* **2012**, *14* (22), 8160–8169. https://doi.org/10.1039/C2CP40196G.
(35) Adelhelm, P.; Gao, J.; Verkuijlen, M. H. W.; Rongeat, C.; Herrich, M.; van Bentum, P. J. M.; Gutfleisch, O.; Kentgens, A. P. M.; de Jong, K. P.; de Jongh, P. E. Comprehensive Study of Melt Infiltration for the Synthesis of $NaAlH_4$/C Nanocomposites. *Chem. Mater.* **2010**, *22* (7), 2233–2238. https://doi.org/10.1021/cm902681d.
(36) Gao, J.; Adelhelm, P.; Verkuijlen, M. H. W.; Rongeat, C.; Herrich, M.; Jan, P.; Van Bentum, M.; Gutfleisch, O.; Kentgens, A. P. M.; De Jong, K. P.; De Jongh, P. E. Confinement of $NaAlH_4$ in Nanoporous Carbon: Impact on H_2 Release, Reversibility, and Thermodynamics. https://doi.org/10.1021/jp910511g.
(37) Anton, D. L. Hydrogen Desorption Kinetics in Transition Metal Modified $NaAlH_4$. *J. Alloys Compd.* **2003**, *356–357*, 400–404. https://doi.org/10.1016/S0925-8388(03)00140-3.
(38) Ali, N. A.; Ismail, M. Modification of $NaAlH_4$ Properties Using Catalysts for Solid-State Hydrogen Storage: A Review. *Int. J. Hydrogen Energy* **2020**. https://doi.org/10.1016/j.ijhydene.2020.10.011.
(39) Sandrock, G.; Gross, K.; Thomas, G. Effect of Ti-Catalyst Content on the Reversible Hydrogen Storage Properties of the Sodium Alanates. *J. Alloys Compd.* **2002**, *339* (1–2), 299–308. https://doi.org/10.1016/S0925-8388(01)02014-X.

(40) Peinecke, K.; Meggouh, M.; Felderhoff, M. Mechanochemical Synthesis and Effect of Various Additives on the Hydrogen Absorption–Desorption Behavior of Na_3AlH_6. *J Mater Sci* **2018**, *53* (19), 13742–13750. https://doi.org/10.1007/s10853-018-2279-3.
(41) Ismail, M. Study on the Hydrogen Storage Properties and Reaction Mechanism of $NaAlH_4$–MgH_2–$LiBH_4$ Ternary-Hydride System. *Int. J. Hydrogen Energy* **2014**, *39* (16), 8340–8346. https://doi.org/10.1016/j.ijhydene.2014.03.166.
(42) Pinkerton, F. E. Comparison of Hydrogen Cycling Kinetics in $NaAlH_4$–Carbon Aerogel Composites Synthesized by Melt Infusion or Ball Milling. *Journal of Alloys and Compounds* **2011**, *509* (36), 8958–8964. https://doi.org/10.1016/j.jallcom.2011.06.097.
(43) Baldé, C. P.; Hereijgers, B. P. C.; Bitter, J. H.; de Jong, K. P. Facilitated Hydrogen Storage in $NaAlH_4$ Supported on Carbon Nanofibers. *Angew. Chem.* **2006**, *118* (21), 3581–3583. https://doi.org/10.1002/ange.200504202.
(44) Stephens, R. D.; Gross, A. F.; Atta, S. L. V.; Vajo, J. J.; Pinkerton, F. E. The Kinetic Enhancement of Hydrogen Cycling in $NaAlH_4$ by Melt Infusion into Nanoporous Carbon Aerogel. *Nanotechnology* **2009**, *20* (20), 204018. https://doi.org/10.1088/0957-4484/20/20/204018.
(45) Zaluska, A.; Zaluski, L.; Ström-Olsen, J. O. Sodium Alanates for Reversible Hydrogen Storage. *J. Alloys Compd.* **2000**, *298* (1), 125–134. https://doi.org/10.1016/S0925-8388(99)00666-0.
(46) Cento, C.; Gislon, P.; Bilgili, M.; Masci, A.; Zheng, Q.; Prosini, P. P. How Carbon Affects Hydrogen Desorption in $NaAlH_4$ and Ti-Doped $NaAlH_4$. *J. Alloys Compd.* **2007**, *437* (1), 360–366. https://doi.org/10.1016/j.jallcom.2006.09.025.
(47) Schneemann, A.; White, J. L.; Kang, S.; Jeong, S.; Wan, L. F.; Cho, E. S.; Heo, T. W.; Prendergast, D.; Urban, J. J.; Wood, B. C.; Allendorf, M. D.; Stavila, V. Nanostructured Metal Hydrides for Hydrogen Storage. *Chem. Rev.* **2018**, *118* (22), 10775–10839. https://doi.org/10.1021/acs.chemrev.8b00313.
(48) Varin, R.; Czujko, T.; Wronski, Z. s; Zaranski, Z. Nanomaterials for Hydrogen Storage Produced by Ball Milling. *Canadian Metallurgical Quarterly* **2009**, *48*, 11–25. https://doi.org/10.1179/000844309794239143.
(49) Sazelee, N.; Mustafa, N. S.; Yahya, M. S.; Ismail, M. Enhanced Dehydrogenation Performance of $NaAlH_4$ by the Addition of Spherical $SrTiO_3$. *International Journal of Energy Research* **2021**, *45* (6), 8648–8658. https://doi.org/10.1002/er.6401.
(50) Ismail, M.; Ali, N. A.; Sazelee, N. A.; Muhamad, S. U.; Suwarno, S.; Idris, N. H. $CoFe_2O_4$ Synthesized via a Solvothermal Method for Improved Dehydrogenation of $NaAlH_4$. *International Journal of Hydrogen Energy* **2022**, *47* (97), 41320–41328. https://doi.org/10.1016/j.ijhydene.2022.01.215.
(51) de Jongh, P. E.; Adelhelm, P. Nanoparticles and 3D Supported Nanomaterials. In *Handbook of Hydrogen Storage*; Hirscher, M., Ed.; Wiley-VCH Verlag GmbH & Co. KGaA: Weinheim, Germany, 2010; pp 279–340. https://doi.org/10.1002/9783527629800.ch10.
(52) Gao, J.; Adelhelm, P.; Verkuijlen, M. H. W.; Rongeat, C.; Herrich, M.; van Bentum, P. J. M.; Gutfleisch, O.; Kentgens, A. P. M.; de Jong, K. P.; de Jongh, P. E. Confinement of $NaAlH_4$ in Nanoporous Carbon: Impact on H_2 Release, Reversibility, and Thermodynamics. *J. Phys. Chem. C* **2010**, *114* (10), 4675–4682. https://doi.org/10.1021/jp910511g.

(53) Mathur, R. B.; Singh, B. P.; Pande, S. *Carbon Nanomaterials: Synthesis, Structure, Properties and Applications*; CRC Press, Taylor & Francis Group: Boca Raton, FL, USA, 2017.
(54) Klein, R. A.; Evans, H. A.; Trump, B. A.; Udovic, T. J.; Brown, C. M. 10.02 – Neutron Scattering Studies of Materials for Hydrogen Storage. In *Comprehensive Inorganic Chemistry III (Third Edition)*; Reedijk, J., Poeppelmeier, K. R., Eds.; Elsevier: Oxford, 2023; pp 3–50. https://doi.org/10.1016/B978-0-12-823144-9.00028-5.
(55) Yartys, V. A.; Webb, C. J.; Cuevas, F. In Situ Diffraction Studies of Phase-Structural Transformations in Hydrogen and Energy Storage Materials: An Overview. *Journal of Alloys and Compounds* **2023**, *953*, 170133. https://doi.org/10.1016/j.jallcom.2023.170133.
(56) Bellosta von Colbe, J. M.; Schmidt, W.; Felderhoff, M.; Bogdanović, B.; Schüth, F. Hydrogen-Isotope Scrambling on Doped Sodium Alanate. *Angewandte Chemie International Edition* **2006**, *45* (22), 3663–3665. https://doi.org/10.1002/anie.200504425.
(57) Borgschulte, A.; Züttel, A.; Hug, P.; Barkhordarian, G.; Eigen, N.; Dornheim, M.; Bormann, R.; Ramirez-Cuesta, A. J. Hydrogen–Deuterium Exchange Experiments to Probe the Decomposition Reaction of Sodium Alanate. *Phys. Chem. Chem. Phys.* **2008**, *10* (27), 4045–4055. https://doi.org/10.1039/B803147A.
(58) Xiong, R.; Sang, G.; Yan, X.; Zhang, G.; Li, P.; Qin, C.; Lü, J.; Song, J.; Chen, C.; Tang, T. Hydrogen and Deuterium Interaction of $NaAlH_xD_{4-x}$ ($0 \leq x \geq 4$) and Its Kinetics Isotope Effect. *International Journal of Hydrogen Energy* **2017**, *42* (9), 6160–6165. https://doi.org/10.1016/j.ijhydene.2016.11.086.
(59) Gross, K. J.; Guthrie, S.; Takara, S.; Thomas, G. In-Situ X-Ray Diffraction Study of the Decomposition of $NaAlH_4$. *Journal of Alloys and Compounds* **2000**, *297* (1–2), 270–281. https://doi.org/10.1016/S0925-8388(99)00598-8.
(60) Léon, A.; Wuttke, J. Hydrogen Release from Sodium Alanate Observed by Time-Resolved Neutron Backscattering. *J. Phys.: Condens. Matter* **2011**, *23* (25), 254214. https://doi.org/10.1088/0953-8984/23/25/254214.
(61) Walters, R. T.; Scogin, J. H. A Reversible Hydrogen Storage Mechanism for Sodium Alanate: The Role of Alanes and the Catalytic Effect of the Dopant. *J. Alloys Compd.* **2004**, *379* (1), 135–142. https://doi.org/10.1016/j.jallcom.2004.04.155.
(62) Brinks, H. W.; Jensen, C. M.; Srinivasan, S. S.; Hauback, B. C.; Blanchard, D.; Murphy, K. Synchrotron X-Ray and Neutron Diffraction Studies of $NaAlH_4$ Containing Ti Additives. *Journal of Alloys and Compounds* **2004**, *376* (1), 215–221. https://doi.org/10.1016/j.jallcom.2003.12.024.
(63) Humphries, T. D.; Makepeace, J. W.; Hino, S.; David, W. I. F.; Hauback, B. C. Regeneration of Sodium Alanate Studied by Powder in Situ Neutron and Synchrotron X-Ray Diffraction. *J. Mater. Chem. A* **2014**, *2* (39), 16594–16600. https://doi.org/10.1039/C4TA02886D.
(64) Balogh, M. P.; Tibbetts, G. G.; Pinkerton, F. E.; Meisner, G. P.; Olk, C. H. Phase Changes and Hydrogen Release during Decomposition of Sodium Alanates. *J. Alloys Compd.* **2003**, *350* (1), 136–144. https://doi.org/10.1016/S0925-8388(02)00996-9.
(65) Gross, K. J.; Sandrock, G.; Thomas, G. J. Dynamic in Situ X-Ray Diffraction of Catalyzed Alanates. *J. Alloys Compd.* **2002**, *330–332*, 691–695. https://doi.org/10.1016/S0925-8388(01)01463-3.
(66) Colognesi, D.; Ulivi, L.; Zoppi, M.; Ramirez-Cuesta, A. J.; Orecchini, A.; Karkamkar, A. J.; Fichtner, M.; Gil Bardají, E.; Zhao-Karger, Z. Hydrogen-Storage

Materials Dispersed into Nanoporous Substrates Studied through Incoherent Inelastic Neutron Scattering. *J. Alloys Compd.* **2012**, *538*, 91–99. https://doi.org/10.1016/j.jallcom.2012.05.081.
(67) Chen, T.-T.; Yang, C.-H.; Tsai, W.-T. In-Situ Synchrotron X-Ray Diffraction Study on the Dehydrogenation Behavior of $NaAlH_4$ Modified by Multi-Walled Carbon Nanotubes. *Int. J. Hydrogen Energy* **2012**, *37* (19), 14285–14291. https://doi.org/10.1016/j.ijhydene.2012.07.012.
(68) Chumphongphan, S.; Filsø, U.; Paskevicius, M.; Sheppard, D. A.; Jensen, T. R.; Buckley, C. E. Nanoconfinement Degradation in $NaAlH_4$/CMK-1. *Int. J. Hydrogen Energy* **2014**, *39* (21), 11103–11109. https://doi.org/10.1016/j.ijhydene.2014.05.087.
(69) *Role of Nuclear Based Techniques in Development and Characterization of Materials for Hydrogen Storage and Fuel Cells*; TECDOC Series; INTERNATIONAL ATOMIC ENERGY AGENCY: Vienna, 2012.
(70) Pearre, N. S.; Kempton, W.; Guensler, R. L.; Elango, V. V. Electric Vehicles: How Much Range Is Required for a Day's Driving? *Transportation Research Part C: Emerging Technologies* **2011**, *19* (6), 1171–1184. https://doi.org/10.1016/j.trc.2010.12.010.
(71) Zhang, S.; Li, S.; Tian, B.; Fu, X.; Chen, B.; Wu, X.; Wu, Y. Individual Electric Vehicle Range Evaluation and Optimization by Real-World Usage Data. *Energy* **2025**, *320*, 135414. https://doi.org/10.1016/j.energy.2025.135414.
(72) Gilbert, J. A.; Shkrob, I. A.; Abraham, D. P. Transition Metal Dissolution, Ion Migration, Electrocatalytic Reduction and Capacity Loss in Lithium-Ion Full Cells. *J. Electrochem. Soc.* **2017**, *164* (2), A389. https://doi.org/10.1149/2.1111702jes.
(73) Thompson, L. M.; Stone, W.; Eldesoky, A.; Smith, N. K.; McFarlane, C. R. M.; Kim, J. S.; Johnson, M. B.; Petibon, R.; Dahn, J. R. Quantifying Changes to the Electrolyte and Negative Electrode in Aged NMC532/Graphite Lithium-Ion Cells. *J. Electrochem. Soc.* **2018**, *165* (11), A2732. https://doi.org/10.1149/2.0721811jes.
(74) Eldesoky, A.; Kowalski, N.; Dahn, J. R. Highlighting the Advantages of Operating NMC811 Cells to Voltages below 4.20 V Compared to NMC Grades with Lower Ni Content. *J. Electrochem. Soc.* **2023**, *170* (8), 080515. https://doi.org/10.1149/1945-7111/aceffd.
(75) *BMW electric car battery and drive technology.* https://www.bmw-me.com/en/electric-cars/battery-technology.html (accessed 2025-05-20).
(76) *How do I maintain my electric vehicle battery?* https://www.ford.com/support/how-tos/electric-vehicles/electric-vehicle-maintenance/how-do-i-maintain-my-electric-vehicle-battery/ (accessed 2025-05-20).
(77) team, C. *How much should I charge my Tesla?*. California Learning Resource Network. https://www.clrn.org/how-much-should-i-charge-my-tesla/ (accessed 2025-05-20).
(78) Kostopoulos, E. D.; Spyropoulos, G. C.; Kaldellis, J. K. Real-World Study for the Optimal Charging of Electric Vehicles. *Energy Reports* **2020**, *6*, 418–426. https://doi.org/10.1016/j.egyr.2019.12.008.
(79) *BMW Certified Electric*. https://www.bmw.ca/en/topics/details/preowned/certified-electric.html (accessed 2025-05-10).
(80) *Vehicle Warranty | Tesla Support Canada*. Tesla. https://www.tesla.com/en_ca/support/vehicle-warranty (accessed 2025-05-10).
(81) Michelini, E.; Höschele, P.; Ratz, F.; Stadlbauer, M.; Rom, W.; Ellersdorfer, C.; Moser, J. Potential and Most Promising Second-Life Applications for Automotive

Lithium-Ion Batteries Considering Technical, Economic and Legal Aspects. *Energies* **2023**, *16* (6), 2830. https://doi.org/10.3390/en16062830.

(82) Kampker, A.; Heimes, H. H.; Offermanns, C.; Vienenkötter, J.; Frank, M.; Holz, D. Identification of Challenges for Second-Life Battery Systems—A Literature Review. *World Electric Vehicle Journal* **2023**, *14* (4), 80. https://doi.org/10.3390/wevj14040080.

(83) Misbrener, K. *Enphase launches new residential LFP battery with 15-year warranty*. Solar Power World. https://www.solarpowerworldonline.com/2023/05/enphase-launches-new-residential-lfp-battery-15-year-warranty/ (accessed 2024-07-23).

(84) Song, K. *Comparing Solar Battery Warranties: Enphase, Generac, Tesla*. Solar-Insure. https://www.solarinsure.com/solar-battery-warranties-compared-enphase-generac-tesla-solaredge (accessed 2024-07-23).

(85) Liu, C. *China LiFePO₄ Deep Cycle Rechargeable Battery 5000 Life Cycles With 15-Year Lifetime Manufacturers, Suppliers, Factory – Wholesale Price – BLUE CARBON*. Blue Carbon. https://www.bctvnergy.com/lithium-battery/lifepo4-deep-cycle-rechargeable-battery-5000.html (accessed 2024-07-23).

(86) Ahern, B. Optimizing the Integration of Renewable Energy – The Importance of Speed and Strategy. In *2019 IEEE Power & Energy Society General Meeting (PESGM)*; 2019; pp 1–5. https://doi.org/10.1109/PESGM40551.2019.8973950.

(87) Paarmann, S.; Schreiber, M.; Chahbaz, A.; Hildenbrand, F.; Stahl, G.; Rogge, M.; Dechent, P.; Queisser, O.; Frankl, S. D.; Morales Torricos, P.; Lu, Y.; Nikolov, N. I.; Kateri, M.; Sauer, D. U.; Danzer, M. A.; Wetzel, T.; Endisch, C.; Lienkamp, M.; Jossen, A.; Lewerenz, M. Short-Term Tests, Long-Term Predictions – Accelerating Ageing Characterisation of Lithium-Ion Batteries. *Batteries & Supercaps* **2024**, *7* (11), e202300594. https://doi.org/10.1002/batt.202300594.

(88) Lu, Z.; MacNeil, D. D.; Dahn, J. R. Layered Cathode Materials $Li[Ni_xLi_{[(1/3-2x/3)}Mn_{(2/3-x/3)}]O_2$ for Lithium-Ion Batteries. *Electrochem. Solid-State Lett.* **2001**, *4* (11), A191. https://doi.org/10.1149/1.1407994.

(89) Noh, H.-J.; Youn, S.; Yoon, C. S.; Sun, Y.-K. Comparison of the Structural and Electrochemical Properties of Layered $Li[Ni_xCo_yMn_z]O_2$ (x = 1/3, 0.5, 0.6, 0.7, 0.8 and 0.85) Cathode Material for Lithium-Ion Batteries. *Journal of Power Sources* **2013**, *233*, 121–130. https://doi.org/10.1016/j.jpowsour.2013.01.063.

(90) Jung, R.; Metzger, M.; Maglia, F.; Stinner, C.; Gasteiger, H. A. Chemical versus Electrochemical Electrolyte Oxidation on NMC111, NMC622, NMC811, LNMO, and Conductive Carbon. *J. Phys. Chem. Lett.* **2017**, *8* (19), 4820–4825. https://doi.org/10.1021/acs.jpclett.7b01927.

(91) Aiken, C. P.; Logan, E. R.; Eldesoky, A.; Hebecker, H.; Oxner, J. M.; Harlow, J. E.; Metzger, M.; Dahn, J. R. $Li[Ni_{0.5}Mn_{0.3}Co_{0.2}]O_2$ as a Superior Alternative to $LiFePO_4$ for Long-Lived Low Voltage Li-Ion Cells. *J. Electrochem. Soc.* **2022**, *169* (5), 050512. https://doi.org/10.1149/1945-7111/ac67b5.

(92) Jiang, J.; Dahn, J. R. ARC Studies of the Thermal Stability of Three Different Cathode Materials: $LiCoO_2$; $Li[Ni_{0.1}Co_{0.8}Mn_{0.1}]O_2$; and $LiFePO_4$, in $LiPF_6$ and LiBoB EC/DEC Electrolytes. *Electrochemistry Communications* **2004**, *6* (1), 39–43. https://doi.org/10.1016/j.elecom.2003.10.011.

(93) MacNeil, D. D.; Dahn, J. R. The Reaction of Charged Cathodes with Nonaqueous Solvents and Electrolytes: I. $Li_{0.5}CoO_2$. *J. Electrochem. Soc.* **2001**, *148* (11), A1205. https://doi.org/10.1149/1.1407245.

(94) Jhu, C.-Y.; Wang, Y.-W.; Wen, C.-Y.; Shu, C.-M. Thermal Runaway Potential of $LiCoO_2$ and $Li(Ni_{1/3}Co_{1/3}Mn_{1/3})O_2$ Batteries Determined with Adiabatic Calorimetry Methodology. *Applied Energy* **2012**, *100*, 127–131. https://doi.org/10.1016/j.apenergy.2012.05.064.
(95) Ma, L.; Nie, M.; Xia, J.; Dahn, J. R. A Systematic Study on the Reactivity of Different Grades of Charged $Li[Ni_xMn_yCo_z]O_2$ with Electrolyte at Elevated Temperatures Using Accelerating Rate Calorimetry. *Journal of Power Sources* **2016**, *327*, 145–150. https://doi.org/10.1016/j.jpowsour.2016.07.039.
(96) Rinkel, B. L. D.; Hall, D. S.; Temprano, I.; Grey, C. P. Electrolyte Oxidation Pathways in Lithium-Ion Batteries. *J. Am. Chem. Soc.* **2020**, *142* (35), 15058–15074. https://doi.org/10.1021/jacs.0c06363.
(97) Sun, X.; Hao, H.; Hartmann, P.; Liu, Z.; Zhao, F. Supply Risks of Lithium-Ion Battery Materials: An Entire Supply Chain Estimation. *Materials Today Energy* **2019**, *14*, 100347. https://doi.org/10.1016/j.mtener.2019.100347.
(98) *LFP batteries: The electric vehicle battery chemistry debate just got more complicated*. Fastmarkets. https://www.fastmarkets.com/insights/the-ev-battery-chemistry-debate-just-got-more-complicated/ (accessed 2024-03-10).
(99) Olivetti, E. A.; Ceder, G.; Gaustad, G. G.; Fu, X. Lithium-Ion Battery Supply Chain Considerations: Analysis of Potential Bottlenecks in Critical Metals. *Joule* **2017**, *1* (2), 229–243. https://doi.org/10.1016/j.joule.2017.08.019.
(100) Jaffe, S. Vulnerable Links in the Lithium-Ion Battery Supply Chain. *Joule* **2017**, *1* (2), 225–228. https://doi.org/10.1016/j.joule.2017.09.021.
(101) Reimers, J. N.; Dahn, J. R. Electrochemical and In Situ X-Ray Diffraction Studies of Lithium Intercalation in Li_xCoO_2. *J. Electrochem. Soc.* **1992**, *139* (8), 2091–2097. https://doi.org/10.1149/1.2221184.
(102) Li, J.; Liu, H.; Xia, J.; Cameron, A. R.; Nie, M.; Botton, G. A.; Dahn, J. R. The Impact of Electrolyte Additives and Upper Cut-off Voltage on the Formation of a Rocksalt Surface Layer in $LiNi_{0.8}Mn_{0.1}Co_{0.1}O_2$ Electrodes. *J. Electrochem. Soc.* **2017**, *164* (4), A655. https://doi.org/10.1149/2.0651704jes.
(103) Jung, R.; Metzger, M.; Maglia, F.; Stinner, C.; Gasteiger, H. A. Oxygen Release and Its Effect on the Cycling Stability of $LiNi_xMn_yCo_zO_2$ (NMC) Cathode Materials for Li-Ion Batteries. *J. Electrochem. Soc.* **2017**, *164* (7), A1361–A1377. https://doi.org/10.1149/2.0021707jes.
(104) Azam, S.; Aiken, C. P.; Meisner, Q.; MacLennan, H.; Song, W.; Liu, Q.; Yoo, D.-J.; Aftanas, S.; Oxner, J. M.; Liao, C.; Garayt, M. D. L.; Hamam, I.; Zhang, Z.; Dahn, J. R. Impact of Electrolyte Additives on the Lifetime of High Voltage NMC Lithium-Ion Pouch Cells. *J. Electrochem. Soc.* **2024**, *171* (11), 110510. https://doi.org/10.1149/1945-7111/ad8d0c.
(105) Zhang, Y.; Katayama, Y.; Tatara, R.; Giordano, L.; Yu, Y.; Fraggedakis, D.; Sun, J. G.; Maglia, F.; Jung, R.; Bazant, M. Z.; Shao-Horn, Y. Revealing Electrolyte Oxidation via Carbonate Dehydrogenation on Ni-Based Oxides in Li-Ion Batteries by in Situ Fourier Transform Infrared Spectroscopy. *Energy Environ. Sci.* **2020**, *13* (1), 183–199. https://doi.org/10.1039/C9EE02543J.
(106) Freiberg, A. T. S.; Sicklinger, J.; Solchenbach, S.; Gasteiger, H. A. Li_2CO_3 Decomposition in Li-Ion Batteries Induced by the Electrochemical Oxidation of the Electrolyte and of Electrolyte Impurities. *Electrochimica Acta* **2020**, *346*, 136271. https://doi.org/10.1016/j.electacta.2020.136271.

(107) Miller, D. J.; Proff, C.; Wen, J. G.; Abraham, D. P.; Bareño, J. Observation of Microstructural Evolution in Li Battery Cathode Oxide Particles by In Situ Electron Microscopy. *Advanced Energy Materials* **2013**, *3* (8), 1098–1103. https://doi.org/10.1002/aenm.201300015.
(108) Zhu, X.; Chen, Y.; Chen, H.; Luan, W. The Diffusion Induced Stress and Cracking Behaviour of Primary Particle for Li-Ion Battery Electrode. *International Journal of Mechanical Sciences* **2020**, *178*, 105608. https://doi.org/10.1016/j.ijmecsci.2020.105608.
(109) Yan, P.; Zheng, J.; Gu, M.; Xiao, J.; Zhang, J.-G.; Wang, C.-M. Intragranular Cracking as a Critical Barrier for High-Voltage Usage of Layer-Structured Cathode for Lithium-Ion Batteries. *Nat Commun* **2017**, *8* (1), 14101. https://doi.org/10.1038/ncomms14101.
(110) Bond, T.; Gauthier, R.; Gasilov, S.; Dahn, J. R. In-Situ Computed Tomography of Particle Microcracking and Electrode Damage in Cycled NMC622/Graphite Pouch Cell Batteries. *J. Electrochem. Soc.* **2022**, *169* (8), 080531. https://doi.org/10.1149/1945-7111/ac8a22.
(111) Bond, T.; Gauthier, R.; King, G.; Dressler, R.; Abraham, J. J.; Dahn, J. R. The Complex and Spatially Heterogeneous Nature of Degradation in Heavily Cycled Li-Ion Cells. *J. Electrochem. Soc.* **2024**, *171* (11), 110514. https://doi.org/10.1149/1945-7111/ad88a8.
(112) Li, H.; Liu, A.; Zhang, N.; Wang, Y.; Yin, S.; Wu, H.; Dahn, J. R. An Unavoidable Challenge for Ni-Rich Positive Electrode Materials for Lithium-Ion Batteries. *Chem. Mater.* **2019**, *31* (18), 7574–7583. https://doi.org/10.1021/acs.chemmater.9b02372.
(113) Harlow, J. E.; Ma, X.; Li, J.; Logan, E.; Liu, Y.; Zhang, N.; Ma, L.; Glazier, S. L.; Cormier, M. M. E.; Genovese, M.; Buteau, S.; Cameron, A.; Stark, J. E.; Dahn, J. R. A Wide Range of Testing Results on an Excellent Lithium-Ion Cell Chemistry to Be Used as Benchmarks for New Battery Technologies. *J. Electrochem. Soc.* **2019**, *166* (13), A3031. https://doi.org/10.1149/2.0981913jes.
(114) Li, J.; Cameron, A. R.; Li, H.; Glazier, S.; Xiong, D.; Chatzidakis, M.; Allen, J.; Botton, G. A.; Dahn, J. R. Comparison of Single Crystal and Polycrystalline $LiNi_{0.5}Mn_{0.3}Co_{0.2}O_2$ Positive Electrode Materials for High Voltage Li-Ion Cells. *J. Electrochem. Soc.* **2017**, *164* (7), A1534. https://doi.org/10.1149/2.0991707jes.
(115) Taskovic, T.; Eldesoky, A.; Aiken, C. P.; Dahn, J. R. Low-Voltage Operation and Lithium Bis(Fluorosulfonyl)Imide Electrolyte Salt Enable Long Li-Ion Cell Lifetimes at 85 °C. *J. Electrochem. Soc.* **2022**, *169* (10), 100547. https://doi.org/10.1149/1945-7111/ac9a81.
(116) Eldesoky, A.; Logan, E. R.; Louli, A. J.; Song, W.; Weber, R.; Hy, S.; Petibon, R.; Harlow, J. E.; Azam, S.; Zsoldos, E.; Dahn, J. R. Impact of Graphite Materials on the Lifetime of NMC811/Graphite Pouch Cells: Part II. Long-Term Cycling, Stack Pressure Growth, Isothermal Microcalorimetry, and Lifetime Projection. *J. Electrochem. Soc.* **2022**, *169* (1), 010501. https://doi.org/10.1149/1945-7111/ac42f1.
(117) Eldesoky, A.; Bauer, M.; Azam, S.; Zsoldos, E.; Song, W.; Weber, R.; Hy, S.; Johnson, M. B.; Metzger, M.; Dahn, J. R. Impact of Graphite Materials on the Lifetime of NMC811/Graphite Pouch Cells: Part I. Material Properties, ARC Safety Tests, Gas Generation, and Room Temperature Cycling. *J. Electrochem. Soc.* **2021**, *168* (11), 110543. https://doi.org/10.1149/1945-7111/ac39fc.
(118) Xu, K. *Electrolytes, Interfaces and Interphases*; The Royal Society of Chemistry, 2023. https://doi.org/10.1039/9781837671311.

(119) Xu, K. Li-Ion Battery Electrolytes. *Nat Energy* **2021**, *6* (7), 763–763. https://doi.org/10.1038/s41560-021-00841-6.
(120) Taskovic, T.; Adamson, A.; Clarke, A.; Alter, E. D.; Eldesoky, A.; Gering, K. L.; Tuul, K.; Dahn, J. R. Alkyl Dicarbonates, Common Electrolyte Degradation Products, Can Enable Long-Lived Li-Ion Cells at High Temperatures. *J. Electrochem. Soc.* **2023**, *170* (9), 090527. https://doi.org/10.1149/1945-7111/acf886.
(121) Xu, K. Nonaqueous Liquid Electrolytes for Lithium-Based Rechargeable Batteries. *Chem. Rev.* **2004**, *104* (10), 4303–4418. https://doi.org/10.1021/cr030203g.
(122) Campion, C. L.; Li, W.; Lucht, B. L. Thermal Decomposition of $LiPF_6$-Based Electrolytes for Lithium-Ion Batteries. *J. Electrochem. Soc.* **2005**, *152* (12), A2327. https://doi.org/10.1149/1.2083267.
(123) Logan, E. R.; Eldesoky, A.; Eastwood, E.; Hebecker, H.; Aiken, C. P.; Metzger, M.; Dahn, J. R. The Use of LiFSI and LiTFSI in $LiFePO_4$/Graphite Pouch Cells to Improve High-Temperature Lifetime. *J. Electrochem. Soc.* **2022**, *169* (4), 040560. https://doi.org/10.1149/1945-7111/ac67f9.
(124) Kerner, M.; Plylahan, N.; Scheers, J.; Johansson, P. Thermal Stability and Decomposition of Lithium Bis(Fluorosulfonyl)Imide (LiFSI) Salts. *RSC Adv.* **2016**, *6* (28), 23327–23334. https://doi.org/10.1039/C5RA25048J.
(125) Nyholm, L.; Ericson, T.; Etman, A. S. Revisiting the Stability of Aluminum Current Collectors in Carbonate Electrolytes for High-Voltage Li-Ion Batteries. *Chemical Engineering Science* **2023**, *282*, 119346. https://doi.org/10.1016/j.ces.2023.119346.
(126) Scheer, K. M.; Tulloch, M.; Hamam, I.; Abraham, J. J.; Johnson, M. B.; Metzger, M. Anodic Dissolution of the Aluminum Current Collector in Lithium-Ion Cells with LiFSI, $LiPF_6$, and $LiBF_4$. *J. Electrochem. Soc.* **2025**, *172* (1), 010511. https://doi.org/10.1149/1945-7111/ada641.
(127) Myung, S.-T.; Hitoshi, Y.; Sun, Y.-K. Electrochemical Behavior and Passivation of Current Collectors in Lithium-Ion Batteries. *J. Mater. Chem.* **2011**, *21* (27), 9891–9911. https://doi.org/10.1039/C0JM04353B.
(128) Taskovic, T.; Thompson, L. M.; Eldesoky, A.; Lumsden, M. D.; Dahn, J. R. Optimizing Electrolyte Additive Loadings in NMC532/Graphite Cells: Vinylene Carbonate and Ethylene Sulfate. *J. Electrochem. Soc.* **2021**, *168* (1), 010514. https://doi.org/10.1149/1945-7111/abd833.
(129) Burns, J. C.; Petibon, R.; Nelson, K. J.; Sinha, N. N.; Kassam, A.; Way, B. M.; Dahn, J. R. Studies of the Effect of Varying Vinylene Carbonate (VC) Content in Lithium Ion Cells on Cycling Performance and Cell Impedance. *J. Electrochem. Soc.* **2013**, *160* (10), A1668–A1674. https://doi.org/10.1149/2.031310jes.
(130) Xia, J.; Ma, L.; Aiken, C. P.; Nelson, K. J.; Chen, L. P.; Dahn, J. R. Comparative Study on Prop-1-Ene-1,3-Sultone and Vinylene Carbonate as Electrolyte Additives for $Li(Ni_{1/3}Mn_{13}Co_{1/3})O_2$/Graphite Pouch Cells. *J. Electrochem. Soc.* **2014**, *161* (10), A1634. https://doi.org/10.1149/2.0541410jes.
(131) Nelson, K. J.; Xia, J.; Dahn, J. R. Studies of the Effect of Varying Prop-1-Ene-1,3-Sultone Content in Lithium Ion Pouch Cells. *J. Electrochem. Soc.* **2014**, *161* (12), A1884. https://doi.org/10.1149/2.0791412jes.
(132) Madec, L.; Petibon, R.; Xia, J.; Sun, J.-P.; Hill, I. G.; Dahn, J. R. Understanding the Role of Prop-1-Ene-1,3-Sultone and Vinylene Carbonate in $LiNi_{1/3}Mn_{1/3}Co_{1/3}O_2$/Graphite Pouch Cells: Electrochemical, GC-MS and XPS Analysis. *J. Electrochem. Soc.* **2015**, *162* (14), A2635. https://doi.org/10.1149/2.0741512jes.

(133) Xia, J.; Ma, L.; Dahn, J. R. Improving the Long-Term Cycling Performance of Lithium-Ion Batteries at Elevated Temperature with Electrolyte Additives. *Journal of Power Sources* **2015**, *287*, 377–385. https://doi.org/10.1016/j.jpowsour.2015.04.070.
(134) *Development Perspectives for Lithium-Ion Battery Cell Formats*; Fraunhofer Institute for Systems and Innovation Research ISI: Karlsruhe, Germany, 2022; p 55.
(135) Bond, T. M.; Burns, J. C.; Stevens, D. A.; Dahn, H. M.; Dahn, J. R. Improving Precision and Accuracy in Coulombic Efficiency Measurements of Li-Ion Batteries. *J. Electrochem. Soc.* **2013**, *160* (3), A521. https://doi.org/10.1149/2.014304jes.
(136) Fathi, R.; Burns, J. C.; Stevens, D. A.; Ye, H.; Hu, C.; Jain, G.; Scott, E.; Schmidt, C.; Dahn, J. R. Ultra High-Precision Studies of Degradation Mechanisms in Aged $LiCoO_2$ /Graphite Li-Ion Cells. *J. Electrochem. Soc.* **2014**, *161* (10), A1572–A1579. https://doi.org/10.1149/2.0321410jes.
(137) Smith, A. J.; Burns, J. C.; Dahn, J. R. A High Precision Study of the Coulombic Efficiency of Li-Ion Batteries. *Electrochem. Solid-State Lett.* **2010**, *13* (12), A177–A179. https://doi.org/10.1149/1.3487637.
(138) Smith, A. J.; Burns, J. C.; Xiong, D.; Dahn, J. R. Interpreting High Precision Coulometry Results on Li-Ion Cells. *J. Electrochem. Soc.* **2011**, *158* (10), A1136–A1142. https://doi.org/10.1149/1.3625232.
(139) Floras, C. Minimizing Degradation Mechanisms in 18650 Li-Ion Cells Over a Wide Temperature Range to Predict Lifetime. Master's thesis, Dalhousie University, Halifax, Canada, 2025. https://hdl.handle.net/10222/85012 (accessed 2025-05-09).
(140) Peled, E.; Menkin, S. Review—SEI: Past, Present and Future. *Journal of The Electrochemical Society* **2017**, *164* (7), A1703–A1719.
(141) Horstmann, B.; Single, F.; Latz, A. Review on Multi-Scale Models of Solid-Electrolyte Interphase Formation. *Current Opinion in Electrochemistry* **2019**, *13*, 61–69. https://doi.org/10.1016/j.coelec.2018.10.013.
(142) Taskovic, T.; Eldesoky, A.; Song, W.; Bauer, M.; Dahn, J. R. High Temperature Testing of NMC/Graphite Cells for Rapid Cell Performance Screening and Studies of Electrolyte Degradation. *J. Electrochem. Soc.* **2022**, *169* (4), 040538. https://doi.org/10.1149/1945-7111/ac6453.
(143) Logan, S. R. The Origin and Status of the Arrhenius Equation. *J. Chem. Educ.* **1982**, *59* (4), 279. https://doi.org/10.1021/ed059p279.
(144) Laidler, K. J. The Development of the Arrhenius Equation. *J. Chem. Educ.* **1984**, *61* (6), 494. https://doi.org/10.1021/ed061p494.
(145) Beck, A. F.; Heine, M. A.; Caule, E. J.; Pryor, M. J. The Kinetics of the Oxidation of Al in Oxygen at High Temperature. *Corrosion Science* **1967**, *7* (1), 1–22. https://doi.org/10.1016/S0010-938X(67)80066-0.
(146) Lawless, K. R. The Oxidation of Metals. *Rep. Prog. Phys.* **1974**, *37* (2), 231. https://doi.org/10.1088/0034-4885/37/2/002.
(147) Smith, A. J.; Burns, J. C.; Zhao, X.; Xiong, D.; Dahn, J. R. A High Precision Coulometry Study of the SEI Growth in Li/Graphite Cells. *J. Electrochem. Soc.* **2011**, *158* (5), A447. https://doi.org/10.1149/1.3557892.
(148) Blomgren, G. E. Electrolytes for Advanced Batteries. *Journal of Power Sources* **1999**, *81–82*, 112–118. https://doi.org/10.1016/S0378-7753(99)00188-3.
(149) Bloom, I.; Cole, B. W.; Sohn, J. J.; Jones, S. A.; Polzin, E. G.; Battaglia, V. S.; Henriksen, G. L.; Motloch, C.; Richardson, R.; Unkelhaeuser, T.; Ingersoll, D.;

Case, H. L. An Accelerated Calendar and Cycle Life Study of Li-Ion Cells. *Journal of Power Sources* **2001**, *101* (2), 238–247. https://doi.org/10.1016/S0378-7753(01)00783-2.
(150) Spotnitz, R. Simulation of Capacity Fade in Lithium-Ion Batteries. *Journal of Power Sources* **2003**, *113* (1), 72–80. https://doi.org/10.1016/S0378-7753(02)00490-1.
(151) Ramadass, P.; Haran, B.; White, R.; Popov, B. N. Mathematical Modeling of the Capacity Fade of Li-Ion Cells. *Journal of Power Sources* **2003**, *123* (2), 230–240. https://doi.org/10.1016/S0378-7753(03)00531-7.
(152) Yoshida, T.; Takahashi, M.; Morikawa, S.; Ihara, C.; Katsukawa, H.; Shiratsuchi, T.; Yamaki, J. Degradation Mechanism and Life Prediction of Lithium-Ion Batteries. *J. Electrochem. Soc.* **2006**, *153* (3), A576. https://doi.org/10.1149/1.2162467.
(153) Keil, P.; Schuster, S. F.; Wilhelm, J.; Travi, J.; Hauser, A.; Karl, R. C.; Jossen, A. Calendar Aging of Lithium-Ion Batteries. *J. Electrochem. Soc.* **2016**, *163* (9), A1872. https://doi.org/10.1149/2.0411609jes.
(154) Ecker, M.; Gerschler, J. B.; Vogel, J.; Käbitz, S.; Hust, F.; Dechent, P.; Sauer, D. U. Development of a Lifetime Prediction Model for Lithium-Ion Batteries Based on Extended Accelerated Aging Test Data. *Journal of Power Sources* **2012**, *215*, 248–257. https://doi.org/10.1016/j.jpowsour.2012.05.012.
(155) Ecker, M.; Nieto, N.; Käbitz, S.; Schmalstieg, J.; Blanke, H.; Warnecke, A.; Sauer, D. U. Calendar and Cycle Life Study of Li(NiMnCo)O_2-Based 18650 Lithium-Ion Batteries. *Journal of Power Sources* **2014**, *248*, 839–851. https://doi.org/10.1016/j.jpowsour.2013.09.143.
(156) Schmalstieg, J.; Käbitz, S.; Ecker, M.; Sauer, D. U. From Accelerated Aging Tests to a Lifetime Prediction Model: Analyzing Lithium-Ion Batteries. In *2013 World Electric Vehicle Symposium and Exhibition (EVS27)*; 2013; pp 1–12. https://doi.org/10.1109/EVS.2013.6914753.
(157) Broussely, M.; Herreyre, S.; Biensan, P.; Kasztejna, P.; Nechev, K.; Staniewicz, R. J. Aging Mechanism in Li Ion Cells and Calendar Life Predictions. *Journal of Power Sources* **2001**, *97–98*, 13–21. https://doi.org/10.1016/S0378-7753(01)00722-4.
(158) Broussely, M.; Biensan, Ph.; Bonhomme, F.; Blanchard, Ph.; Herreyre, S.; Nechev, K.; Staniewicz, R. J. Main Aging Mechanisms in Li Ion Batteries. *Journal of Power Sources* **2005**, *146* (1), 90–96. https://doi.org/10.1016/j.jpowsour.2005.03.172.
(159) AutoChem 2950 HP Automated Catalyst Characterization System Operator's Manual, 2011.
(160) Huber, M. L.; Harvey, A. H. Thermal Conductivity of Gases. In *CRC Handbook of Chemistry and Physics*; CRC-Press, Boca Raton, FL, 2011; Vol. 92nd Ed., pp 240–241.
(161) Brunauer, S.; Emmett, P. H.; Teller, E. Adsorption of Gases in Multimolecular Layers. *J Am Chem Soc* **1938**, *60* (2), 309–319. https://doi.org/10.1021/ja01269a023.
(162) Gates-Rector, S.; Blanton, T. The Powder Diffraction File: A Quality Materials Characterization Database. *Powder Diffraction* **2019**, *34* (4), 352–360. https://doi.org/10.1017/S0885715619000812.
(163) Balzar, D. Voigt Function Model in Diffraction-Line Broadening Analysis. In *Defect and Microstructure Analysis by Diffraction*; Snyder, R. L., Fiala, J., Bunge, H. J., Eds.; Oxford University Press, 2000; p 0. https://doi.org/10.1093/oso/9780198501893.003.0007.

(164) Hansen, T. C.; Henry, P. F.; Fischer, H. E.; Torregrossa, J.; Convert, P. The D20 Instrument at the ILL: A Versatile High-Intensity Two-Axis Neutron Diffractometer. *Meas. Sci. Technol.* **2008**, *19* (3), 034001. https://doi.org/10.1088/0957-0233/19/3/034001.
(165) Palm, R.; Forslund, O. K.; Hansen, T. C.; Sebastian, J.; Månsson, M.; Nocerino, E. In Situ Neutron Powder Diffraction Investigation of Structural Changes in Confined $NaAlD_4$/Carbon Composites during Cycling, 2021. https://doi.org/10.5291/ILL-DATA.5-24-689.
(166) Coelho, A. A. TOPAS and TOPAS-Academic: An Optimization Program Integrating Computer Algebra and Crystallographic Objects Written in C++. *J Appl Cryst* **2018**, *51* (1), 210–218. https://doi.org/10.1107/S1600576718000183.
(167) Jain, A.; Ong, S. P.; Hautier, G.; Chen, W.; Richards, W. D.; Dacek, S.; Cholia, S.; Gunter, D.; Skinner, D.; Ceder, G.; Persson, K. A. Commentary: The Materials Project: A Materials Genome Approach to Accelerating Materials Innovation. *APL Materials* **2013**, *1* (1), 011002. https://doi.org/10.1063/1.4812323.
(168) Gross, K. J.; Guthrie, S.; Takara, S.; Thomas, G. In-Situ X-Ray Diffraction Study of the Decomposition of $NaAlH_4$. *J. Alloys Compd.* **2000**, *297* (1), 270–281. https://doi.org/10.1016/S0925-8388(99)00598-8.
(169) Ke, X.; Tanaka, I. Decomposition Reactions for $NaAlH_4$, Na_3AlH_6, and NaH: First-Principles Study. *Phys. Rev. B* **2005**, *71* (2), 024117. https://doi.org/10.1103/PhysRevB.71.024117.
(170) Aiken, C. P.; Xia, J.; Wang, D. Y.; Stevens, D. A.; Trussler, S.; Dahn, J. R. An Apparatus for the Study of In Situ Gas Evolution in Li-Ion Pouch Cells. *J. Electrochem. Soc.* **2014**, *161* (10), A1548–A1554. https://doi.org/10.1149/2.0151410jes.
(171) Eldesoky, A.; Logan, E. R.; Johnson, M. B.; McFarlane, C. R. M.; Dahn, J. R. Scanning Micro X-Ray Fluorescence (μXRF) as an Effective Tool in Quantifying Fe Dissolution in $LiFePO_4$ Cells: Towards a Mechanistic Understanding of Fe Dissolution. *J. Electrochem. Soc.* **2020**, *167* (13), 130539. https://doi.org/10.1149/1945-7111/abba62.
(172) Blaine, R. L.; Kissinger, H. E. Homer Kissinger and the Kissinger Equation. *Thermochim. Acta* **2012**, *540*, 1–6. https://doi.org/10.1016/j.tca.2012.04.008.
(173) Thommes, M.; Kaneko, K.; Neimark, A. V.; Olivier, J. P.; Rodriguez-Reinoso, F.; Rouquerol, J.; Sing, K. S. W. Physisorption of Gases, with Special Reference to the Evaluation of Surface Area and Pore Size Distribution (IUPAC Technical Report). *Pure Appl. Chem.* **2015**, *87* (9–10), 1051–1069. https://doi.org/10.1515/pac-2014-1117.
(174) Sartory, M.; Wallnöfer-Ogris, E.; Salman, P.; Fellinger, T.; Justl, M.; Trattner, A.; Klell, M. Theoretical and Experimental Analysis of an Asymmetric High Pressure PEM Water Electrolyser up to 155 Bar. *Int. J. Hydrogen Energy* **2017**, *42* (52), 30493–30508. https://doi.org/10.1016/j.ijhydene.2017.10.112.
(175) Jung, R.; Strobl, P.; Maglia, F.; Stinner, C.; Gasteiger, H. A. Temperature Dependence of Oxygen Release from $LiNi_{0.6}Mn_{0.2}Co_{0.2}O_2$ (NMC622) Cathode Materials for Li-Ion Batteries. *J. Electrochem. Soc.* **2018**, *165* (11), A2869. https://doi.org/10.1149/2.1261811jes.
(176) Freiberg, A. T. S.; Roos, M. K.; Wandt, J.; de Vivie-Riedle, R.; Gasteiger, H. A. Singlet Oxygen Reactivity with Carbonate Solvents Used for Li-Ion Battery Electrolytes. *J. Phys. Chem. A* **2018**, *122* (45), 8828–8839. https://doi.org/10.1021/acs.jpca.8b08079.

(177) Dixit, M.; Markovsky, B.; Schipper, F.; Aurbach, D.; Major, D. T. Origin of Structural Degradation During Cycling and Low Thermal Stability of Ni-Rich Layered Transition Metal-Based Electrode Materials. *J. Phys. Chem. C* **2017**, *121* (41), 22628–22636. https://doi.org/10.1021/acs.jpcc.7b06122.
(178) Streich, D.; Erk, C.; Guéguen, A.; Müller, P.; Chesneau, F.-F.; Berg, E. J. Operando Monitoring of Early Ni-Mediated Surface Reconstruction in Layered Lithiated Ni–Co–Mn Oxides. *J. Phys. Chem. C* **2017**, *121* (25), 13481–13486. https://doi.org/10.1021/acs.jpcc.7b02303.
(179) *Ethyl methyl carbonate | $C_4H_8O_3$*. ChemSpider. https://www.chemspider.com/Chemical-Structure.455390.html (accessed 2025-05-23).
(180) Rodrigues, M.-T. F.; Babu, G.; Gullapalli, H.; Kalaga, K.; Sayed, F. N.; Kato, K.; Joyner, J.; Ajayan, P. M. A Materials Perspective on Li-Ion Batteries at Extreme Temperatures. *Nat Energy* **2017**, *2* (8), 17108. https://doi.org/10.1038/nenergy.2017.108.
(181) Tang, B.; Zhang, N.; Alter, E.; Eldesoky, A.; Dahn, J. R. Transition Metal Dissolution from Single Crystal $Li[Ni_{1-x-y}MnxCoy]O_2$ and $Li[Ni_{1-x}Mn_x]O_2$ Positive Electrodes Subjected to Aggresive Conditions. *J. Electrochem. Soc.* **2024**, *171* (1), 010518. https://doi.org/10.1149/1945-7111/ad1d25.
(182) Martin Maher, S.; Floras, C.; Bauer, M.; Tuul, K.; Black, W.; Yue, M.; Azam, S.; Dahn, J. R. Changes to the Electrolyte in NMC640/Graphite Li-Ion Pouch Cells Tested for One Year at 85 °C. *J. Electrochem. Soc.* **2025**, *172* (5), 050521. https://doi.org/10.1149/1945-7111/add41a.
(183) Aiken, C. Achieving Lithium-Ion Cells with Improved Performance and Lifetime. PhD thesis, Dalhousie University, 2023. https://DalSpace.library.dal.ca//handle/10222/83319 (accessed 2024-08-19).
(184) Floras, C.; Martin Maher, S.; Tuul, K.; Harlow, J.; Bauer, M.; Dahn, J. R. Designing a Lithium-Ion Cell for Studies of a Single Degradation Mechanism Over a Wide Temperature Range. *J. Electrochem. Soc.* **2025**, *172* (2), 020514. https://doi.org/10.1149/1945-7111/adb184.

9. SUMMARY IN ESTONIAN

Liitiumioonakude ja vesinikuhoiustusmaterjalide karakteriseerimine ekstreemsetes keskkonnatingimustes kõrgtehnoloogiliste meetoditega

Energiakriis, mille tekitas Venemaa sissetung Ukrainasse, on sundinud Euroopa Liitu liikuma energiasõltumatuse ja taastuvenergeetika kasutuselevõtu suunas. Programmid nagu *REPowerEU* ja *Fit for 55* on suunatud fossiilkütustest ja energiaimpordist irdumisele ning kasvuhoonegaaside heitkoguste vähendamisele. Eesmärgiks on vähendada emissioone 55% võrra 2030. aastaks ning jõuda täieliku kliimaneutraalsuseni 2050. aastaks. Taastuvenergiaallikate kasutuselevõtt on nende eesmärkide saavutamise aluseks, kuid nende integreerimiseks energiaturule on tarvis jätkusuutlikke ning töökindlaid energiasalvestusmeetodeid.

Sekundaarsed liitiumioonpatareid ehk liitiumioonakud domineerivad energiasalvestuse turgu, eriti just lühiajalist salvestamist. See on eelkõige tänu nende suurele energiatihedusele, kõrgele kasutegurile ja pikaajaliselt väljakujunenud tehnoloogiale ning tarneahelatele. Siiski on väljakutseteks toorainete kättesaadavuse ning nende tarneahelate julgeolekuga, materjalide jätkusuutlikkusega ning sobimatusega pikaajaliseks ja sesoonseks energiasalvestuseks. Leevendust pakuks pikema elueaga akuehituse eelistamine ning kasutatud, kuid töövõimeliste akude järelturu (nn „teine elu“ või ingl *second life*) rakendamisega. Teisalt vesinik, mis on toodetud taastuvenergiast vee elektrolüüsi teel, on potentsiaalne lahendus just pikaajaliseks ja hooajaliseks energiasalvestuseks. Kahjuks vesiniku enda salvestustehnoloogiaid kimbutavad kõrged kulud, madal kasutegur ning probleemid ohutusega.

Käesolev doktoritöö käsitleb kaht energiasalvestustehnoloogiat: vesiniku salvestamist tahkel kujul keemiliselt seondatuna naatriumalanaadis ($NaAlH_4$) ning pika elueaga liitiumioonakusid. Neid süsteeme karakteriseeriti harilike laborimeetoditega nagu röntgendifraktsioonanalüüs, gaasi adsorptsioon ning elektrokeemilised testid. Võtmeteadmised saadi aga kõrgtehnoloogiliste meetoditega: neutrondifraktsioon võimaldas *in situ* jälgida $NaAlH_4$/süsiniktahm komposiitmaterjalide faasisiirdeid. Ülikõrglahutuskulonomeetria (UHPC) koostöös kiirendatud vanandamisega kõrgetel temperatuuridel võimaldas liitiumioonakude degradatsioonimehaanismide, s.o mahutavuse kao põhjuste, analüüsimist ning akude eluea ennustamist.

$NaAlH_4$ vesinikusalvestusomaduste parandamiseks vähendati osakese suurust nanoosakesteks. Seda saavutati koos mesopoorse süsiniktahmaga jahvatamisel kuulveskis. Sel moel õnnestus alanaat lõksustada süsinikmaterjali nanopooridesse, süsinikmaterjali osakeste vahele ja eeldatavasti ka õhukese kihina süsinikmaterjali osakeste pinnale. Selle tulemusena langes vesiniku eraldumise temperatuur märgatavalt: vesinik hakkas suurtes kogustes eralduma juba 100 °C juures, kui alanaadisisaldus komposiidis oli 50 massi%. Puhtas alanaadis hakkab vesinik

intensiivselt vabanema alles sulamispunkti, s.o 183 °C juures. Vesiniku seondamine materjalis saavutati 150 °C juures ja vesinikurõhul 20 bar. Need on väga mõõdukad tingimused arvestades, et puhta alanaadi lagunemine on sisuliselt pöördumatu. Siiski takistab lagunemise täielikku pöördumist faaside füüsiline lahusolek. Selle vastu võiks aidata süsinikmaterjali struktuuri peenhäälestamine metallkarbiidide abiga ning metalsete katalüsaatorite kaasamine.

Liitiumioonakud optimeeriti esmalt kõrgtemperatuurseks (60–100 °C) tööks ning pika eluea jaoks. Selleks valiti hoolikalt positiivse elektroodi materjali, elektrolüüdi solvente, soola, lisandeid ja aku formaati. Paljulubavaid tulemusi saavutati *pouch*-tüüpi akudega, kus oli $Li[Ni_{0.6}Mn_{0.4}Co_{0.0}]O_2$ positiivseks elektroodiks, sünteetiline grafiit negatiivseks elektroodiks, etüleenkarbonaadi ja dietüülkarbonaadi segu elektrolüüdi solventideks, liitiumbis(fluorosulfonüül)imiid soolaks ning vinüleenkarbonaat ja etüleensulfaat lisanditeks. Siiski ilmnes, et elektrolüüdi solvendid difundeeruvad läbi laminaatpakendi liitekohtade, mistõttu aku võib lõpetada töötamise kuivamise tõttu enne, kui ta jõuab oma elektrokeemilise eluea lõppu. Seetõttu testiti silindrilist metallpakendit ning täiendavat epoksiidhermeetikut kasutades, on tulevikus võimalik viia elektrolüüdikaod minimaalseks. UHPC testimisel laias temperatuurivahemikus ilmnes, et aku mahutavuse kadu järgis Arrheniuse-tüüpi sõltuvust temperatuurist. See võimaldas rakendada lihtsat aja ruutjuurest sõltuvat mudelit, mis võimaldab prognoosida aku mahutavuse vähenemist mitukümmend aastat. Kuigi see mudel ei arvesta veel kõikide võimalike degradatsioonimehhanismidega, mis turul olevaid akusid võivad mõjutada, siis see on oluline ja mõjus samm pikemate garantiiaegade määramisele ning akude järelturu planeerimise jaoks.

10. ACKNOWLEDGEMENTS

First and foremost, I would like to thank my supervisors, **Assoc. Prof. Rasmus Palm** and **Prof. Enn Lust** for all that they have taught me, and for all the guidance and support over the years. To **Prof. Emer. Jeff Dahn**, I am extremely grateful for the opportunity to gain an excellent battery education. I am very grateful to everyone in my personal life who has been there for me and enriched my life and work. Without them, there would be no PhD or many other things. I will refrain from further personal acknowledgements and remain within the confines of this thesis in a professional sense. Yet, I appreciate and recognize all of you, and pledge to demonstrate this the best I can.

I would like to thank the following contributors to this work.

- **MSc Jaan Aruväli** and **Prof. Kalle Kirsimäe** from the Geology Department at the University of Tartu for the XRD measurements.
- **MSc (and by now most likely Dr.) Miriam Koppel** for sharing the path in all of our degree programs and being an important pillar of support throughout.
- **MSc Egert Möller** for being an excellent first supervised student and for all the discussions we've had.
- **Dr. Heili Kasuk, Prof. Jaak Nerut, Dr. Ove Korjus, and MSc Annabel Olgo** for discussions and support.
- **Assoc. Prof. Karmen Lust** for being an excellent teacher of Physical Chemistry and for all the consultations on administrative questions.
- **MSc Rait Kanarbik** for making all the instruments work, and **MSc Urve Soonets and MSc Marju Rosenthal** for keeping the Institute of Chemistry running.
- **MSc Michel B. Johnson and BSc Jessie Harlow** for their invaluable help in all things batteries and Dahnlab.
- **BSc (and hopefully soon Dr.) Saad Azam and Dr. Tina Taskovic** for being my first mentors and teachers in the field of Li-ion cells.
- **BSc (and hopefully soon Dr.) Matthew Garayt** for the training and the great discussions he has provided.
- **MSc Kate Leslie and MSc Jeffin James Abraham** for being excellent colleagues for training and research.
- **MSc Ethan Alter and MSc Emily Butler** for their support in enabling my stay in Halifax.
- **Mr. Sasha Martin Maher and MSc Claire Floras** for being exemplary students, colleagues, co-authors, and friends. The joy from working with you can only be outshone by the joy in seeing you thrive in your future careers. Also, thank you to Claire Floras for preparing and allowing the reuse of Figure 2 in this work.
- **Prof. Michael Metzger** for discussions and comments on numerous publications.

– **BSc Alison Clarke, BSc William Black, and MSc Anu Adamson** as contributors and co-authors.

This research was funded by the EU through the European Regional Development Fund (project TK141 and the Dora Plus scholarship program). It was also supported by the Estonian Research Council (grants PUTJD957, PRG676, PSG935, TEM-TA81), the Estonian Ministry of Education and Research (TK210U1), the project „Increasing the knowledge intensity of Ida-Viru entrepreneurship“ (ÕÜF1) co-funded by the European Union, and the Graduate School of Functional Materials and Technologies. The author acknowledges financial support from the NSERC/Tesla Canada Industrial Research Chair program and wishes to express their gratitude for the beamtime as well as the great support offered by the staff of Institut Laue-Langevin (ILL).

Finally, I would like to quote the famous words of Calvin Cordozar Broadus Jr.
Last but not least, I want to thank me.
I want to thank me for believing in me.
I want to thank me for doing all this hard work.
I want to thank me for having no days off. [KT: admittedly exaggerated in my case]
I want to thank me for never quitting.
I want to thank me for always being a giver and trying to give more than I receive.
I want to thank me for trying to do more right than wrong.
I want to thank me for just being me at all times.

11. PUBLICATIONS

CURRICULUM VITAE

Name: Kenneth Tuul
Date of birth: June 5th, 1996
Citizenship: Estonian
E-mail: kennethtuul@hotmail.com

Education:

2021–…	University of Tartu, Chemistry (PhD)
2022–2023	Dalhousie University, Visiting Graduate Research Student
2019–2021	University of Tartu, Materials Science and Technology (MSc), *cum laude*
2016–2019	University of Tartu, Physics, Chemistry and Material Science (BSc), *cum laude*
2003–2015	Tallinn Secondary Science School, gold medal

Professional employment:

11.2021–…	Junior Research Fellow of Physical Chemistry, University of Tartu
10.2024–05.2025	Battery Scientist, Skeleton Technologies
01.2024–05.2024	Senior Specialist of Research Management, Tallinn University
10.2019–12.2021	Specialist, University of Tartu Institute of Physics
01.2019–10.2021	Chemist, University of Tartu, Institute of Chemistry
07.2015–05.2016	Estonian Defence Forces, national service

CERCS Research Fields:
T140 Energy research; P401 Electrochemistry; P400 Physical chemistry; T150 Material technology; P250 Condensed matter: structure, thermal and mechanical properties, crystallography, phase equilibria

Membership in professional organizations:

2023–...	The Electrochemical Society, student member
2022–...	International Society of Electrochemistry, member
2018–...	University of Tartu Chemistry Students' Society, alumnus
2016–...	Estonian Physics Students' Society, alumnus
2018–2019	University of Tartu Student Union, student representative in the Institute of Physics

List of publications:

1. S. Martin Maher, C. Floras, M. Bauer, **K. Tuul**, W. Black, M. Yue, S. Azam, J.R, Dahn, Changes to the Electrolyte in NMC640/Graphite Li-Ion Pouch Cells Tested for One Year at 85 °C, J. Electrochem. Soc. 172 (2025), 050521. https://doi.org/10.1149/1945-7111/add41a.

2. M. Koppel, R. Palm, R. Härmas, M.T.F. Telling, M.D. Le, T. Guidi, **K. Tuul**, M. Paalo, E. Lust, Restricted Dynamics and Para-Ortho Conversion of H_2 Adsorbed in Micro- and Mesoporous Carbide-Derived Carbon: A Quasi- and Inelastic Neutron Scattering Study, J. Phys. Chem. C 129 (2025) 4789–4799. https://doi.org/10.1021/acs.jpcc.4c08582.
3. **K. Tuul**, W. Black, C. Floras, T. Taskovic, S. Martin Maher, A. Adamson, J. Harlow, M.B. Johnson, D. Rathore, S. Chisholm, S. Azam, R. Palm, J.R. Dahn, Limitations of Li-Ion Pouch Cells for Accelerated Testing and Long-Lifetime Cells, J. Electrochem. Soc. 172 (2025) 020519. https://doi.org/10.1149/1945-7111/adb217.
4. C. Floras, S. Martin Maher, **K. Tuul**, J. Harlow, M. Bauer, J.R. Dahn, Designing a Lithium-Ion Cell for Studies of a Single Degradation Mechanism Over a Wide Temperature Range, J. Electrochem. Soc. 172 (2025) 020514. https://doi.org/10.1149/1945-7111/adb184.
5. T. Taskovic, A. Clarke, J. Harlow, S. Martin Maher, **K. Tuul**, E. Eastwood, M. Johnson, J.R. Dahn, An Investigation of Li-Ion Cell Degradation Caused by Simulated Autoclave Cycles, J. Electrochem. Soc. 171 (2024) 060520. https://doi.org/10.1149/1945-7111/ad5625.
6. M. Koppel, R. Palm, R. Härmas, M. Telling, M.D. Le, T. Guidi, **K. Tuul**, M. Paalo, L. Kalder, J. Jagiello, T. Romann, J. Aruväli, M. Månsson, E. Lust, Disentangling the self-diffusional dynamics of H_2 adsorbed in micro- and mesoporous carbide-derived carbon by wide temporal range quasi-elastic neutron scattering, Carbon 219 (2024) 118799. https://doi.org/10.1016/j.carbon.2024.118799.
7. **K. Tuul**, S. Martin Maher, C. Floras, W. Black, T. Taskovic, S. Chisholm, A. Clarke, E. Lust, J.R. Dahn, Exceptional Performance of Li-ion Battery Cells with Liquid Electrolyte at 100 °C, J. Electrochem. Soc. 171 (2024) 040510. https://doi.org/10.1149/1945-7111/ad36e7.
8. K. Leslie, J. Harlow, D. Rathore, **K. Tuul**, M. Metzger, Correlating Mn Dissolution and Capacity Fade in $LiMn_{0.8}Fe_{0.2}PO_4$/Graphite Cells During Cycling and Storage at Elevated Temperature, J. Electrochem. Soc. 171 (2024) 040520. https://doi.org/10.1149/1945-7111/ad3b77.
9. E. Möller, R. Palm, **K. Tuul**, M. Härmas, M. Koppel, J. Aruväli, M. Külaviir, E. Lust, Peat-Derived $ZnCl_2$-Activated Ultramicroporous Carbon Materials for Hydrogen Adsorption, Nanomaterials 13 (2023) 2883. https://doi.org/10.3390/nano13212883.
10. P. Ramah, R. Palm, **K. Tuul**, J. Aruväli, M. Månsson, E. Lust, Confinement of $LiAlH_4$ in a Mesoporous Carbon Black for Improved Near-Ambient Release of H_2, Reactions 4 (2023) 635–646. https://doi.org/10.3390/reactions4040035.
11. **K. Tuul**, R. Palm, J. Aruväli, E. Lust, Dehydrogenation and low-pressure hydrogenation properties of $NaAlH_4$ confined in mesoporous carbon black for hydrogen storage, International Journal of Hydrogen Energy 48 (2023) 19646–19656. https://doi.org/10.1016/j.ijhydene.2023.01.358.
12. A. Adamson, **K. Tuul**, T. Bötticher, S. Azam, M.D.L. Garayt, M. Metzger, Improving lithium-ion cells by replacing polyethylene terephthalate jellyroll

tape, Nat. Mater. 22 (2023) 1380–1386. https://doi.org/10.1038/s41563-023-01673-3.

13. T. Taskovic, A. Adamson, A. Clarke, E.D. Alter, A. Eldesoky, K.L. Gering, **K. Tuul**, J.R. Dahn, Alkyl Dicarbonates, Common Electrolyte Degradation Products, Can Enable Long-Lived Li-Ion Cells at High Temperatures, J. Electrochem. Soc. 170 (2023) 090527. https://doi.org/10.1149/1945-7111/acf886.
14. J. Nerut, P. Teppor, R. Palm, R. Jäger, T. Thomberg, **K. Tuul**, M. Koppel, J. Aruväli, A. Kikas, J. Mondal, V. Iakimov, E. Lust, Characterisation of Novel Nitrogen Doped Reduced Graphene Oxide, ECS Trans. 108 (2022) 99. https://doi.org/10.1149/10807.0099ecst.
15. R. Palm, **K. Tuul**, F. Elson, E. Nocerino, O.K. Forslund, T.C. Hansen, J. Aruväli, M. Månsson, In situ neutron diffraction of $NaAlD_4$/carbon black composites during decomposition/deuteration cycles and the effect of carbon on phase segregation, International Journal of Hydrogen Energy 47 (2022) 34195–34204. https://doi.org/10.1016/j.ijhydene.2022.08.019.
16. R. Palm, R. Härmas, E. Härk, B. Kent, H. Kurig, M. Koppel, M. Russina, I. Tallo, T. Romann, J. Mata, **K. Tuul**, E. Lust, Study of the structural curvature in Mo_2C derived carbons with contrast matched small-angle neutron scattering, Carbon 171 (2021) 695–703. https://doi.org/10.1016/j.carbon.2020.09.070.
17. **K. Tuul**, R. Palm, Influence of Nanoconfinement on the Hydrogen Release Processes from Sodium Alanate, Reactions 2 (2021) 1–9. https://doi.org/10.3390/reactions2010001.

Conferences, abstracts, and presentations

1. K. Tuul, "Impact of Longterm Cycling at 85 and 100 °C on Li-ion Battery Cells with Liquid Electrolyte," presented at the International Battery Materials Association Annual Meeting 2024, Halifax, Canada, Sep. 12, 2024. [Poster]
2. K. Tuul, "High-temperature challenges for Li-ion batteries in surgical instruments," presented at the International Summer School and Workshops on "Medical Physics" (poster Voore, Estonia, Jun. 30, 2024. [Oral]
3. K. Tuul, "Limitations of Li-ion Pouch Cells for Accelerated Testing and Long-Lifetime Cells," presented at the International Meeting on Lithium Batteries, Hong Kong, Jun. 18, 2024. [Poster]
4. K. Tuul, "In Situ Study of $NaAlH_4$ Confinement in Mesoporous Carbon Black for Hydrogen Storage," presented at the 8th Baltic Electrochemistry Conference, Tartu, Estonia, Apr. 14, 2024. [Poster]
5. K. Tuul, "Can One Project Cell Lifetime Using Wide Temperature Range Ultra-High Precision Coulometry?," presented at the 244th ECS Meeting, Gothenburg, Sweden, Oct. 12, 2023. [Oral]
6. K. Tuul, "Enhanced hydrogen storage properties of $NaAlH_4$ confined in carbon black," presented at the International Conference on Carbon Chemistry and Materials, Virtual, Nov. 15, 2021. [Oral]

ELULOOKIRJELDUS

Nimi: Kenneth Tuul
Sünniaeg: 5. juuni 1996
Kodakondsus: eesti
E-mail: kennethtuul@hotmail.com

Hariduskäik:

2021–...	Tartu Ülikool, keemia (PhD)
2022–2023	Dalhousie Ülikool, külaliskraadiõppur
2019–2021	Tartu Ülikool, materjaliteadus ja tehnoloogia (MSc), *cum laude*
2016–2019	Tartu Ülikool, füüsika, keemia ja materjaliteadus (BSc), *cum laude*
2003–2015	Tallinna Reaalkool, keskharidus, kuldmedal

Teenistuskäik:

11.2021–…	Tartu Ülikooli keemia instituut, füüsikalise keemia nooremteadur
10.2024–05.2025	Skeleton Technologies, akuteadlane
01.2024–05.2024	Tallinna Ülikool, teaduskorralduse peaspetsialist
10.2019–12.2021	Tartu Ülikooli füüsika instituut, spetsialist
01.2019–10.2021	Tartu Ülikooli keemia instituut, keemik
07.2015–05.2016	Eesti Kaitsevägi, ajateenistus

CERCS valdkonnad:
T140 Energeetika; P401 Elektrokeemia; P400 Füüsikaline keemia; T150 Materjalitehnoloogia; P250 Tahke aine: struktuur, termilised ja mehhaanilised omadused, kristallograafia, faasitasakaal

Kuulumine erialaorganisatsioonidesse:

2023–...	*The Electrochemical Society*, tudengiliige
2022–...	*International Society of Electrochemistry*, liige
2018–...	Tartu Ülikooli Keemiaüliõpilaste Selts, vilistlasliige
2016–...	Eesti Füüsikaüliõpilaste Selts, vilistlasliige
2018–2019	Tartu Ülikooli Üliõpilasesindus, füüsika instituudi üliõpilasesindaja

Publikatsioonid:

1. S. Martin Maher, C. Floras, M. Bauer, **K. Tuul**, W. Black, M. Yue, S. Azam, J.R, Dahn, Changes to the Electrolyte in NMC640/Graphite Li-Ion Pouch Cells Tested for One Year at 85 °C, J. Electrochem. Soc. 172 (2025), 050521. https://doi.org/10.1149/1945-7111/add41a.
2. M. Koppel, R. Palm, R. Härmas, M.T.F. Telling, M.D. Le, T. Guidi, **K. Tuul**, M. Paalo, E. Lust, Restricted Dynamics and Para-Ortho Conversion of H_2

Adsorbed in Micro- and Mesoporous Carbide-Derived Carbon: A Quasi- and Inelastic Neutron Scattering Study, J. Phys. Chem. C 129 (2025) 4789–4799. https://doi.org/10.1021/acs.jpcc.4c08582.
3. **K. Tuul**, W. Black, C. Floras, T. Taskovic, S. Martin Maher, A. Adamson, J. Harlow, M.B. Johnson, D. Rathore, S. Chisholm, S. Azam, R. Palm, J.R. Dahn, Limitations of Li-Ion Pouch Cells for Accelerated Testing and Long-Lifetime Cells, J. Electrochem. Soc. 172 (2025) 020519. https://doi.org/10.1149/1945-7111/adb217.
4. C. Floras, S. Martin Maher, **K. Tuul**, J. Harlow, M. Bauer, J.R. Dahn, Designing a Lithium-Ion Cell for Studies of a Single Degradation Mechanism Over a Wide Temperature Range, J. Electrochem. Soc. 172 (2025) 020514. https://doi.org/10.1149/1945-7111/adb184.
5. T. Taskovic, A. Clarke, J. Harlow, S. Martin Maher, **K. Tuul**, E. Eastwood, M. Johnson, J.R. Dahn, An Investigation of Li-Ion Cell Degradation Caused by Simulated Autoclave Cycles, J. Electrochem. Soc. 171 (2024) 060520. https://doi.org/10.1149/1945-7111/ad5625.
6. M. Koppel, R. Palm, R. Härmas, M. Telling, M.D. Le, T. Guidi, **K. Tuul**, M. Paalo, L. Kalder, J. Jagiello, T. Romann, J. Aruväli, M. Månsson, E. Lust, Disentangling the self-diffusional dynamics of H_2 adsorbed in micro- and mesoporous carbide-derived carbon by wide temporal range quasi-elastic neutron scattering, Carbon 219 (2024) 118799. https://doi.org/10.1016/j.carbon.2024.118799.
7. **K. Tuul**, S. Martin Maher, C. Floras, W. Black, T. Taskovic, S. Chisholm, A. Clarke, E. Lust, J.R. Dahn, Exceptional Performance of Li-ion Battery Cells with Liquid Electrolyte at 100 °C, J. Electrochem. Soc. 171 (2024) 040510. https://doi.org/10.1149/1945-7111/ad36e7.
8. K. Leslie, J. Harlow, D. Rathore, **K. Tuul**, M. Metzger, Correlating Mn Dissolution and Capacity Fade in $LiMn_{0.8}Fe_{0.2}PO_4$/Graphite Cells During Cycling and Storage at Elevated Temperature, J. Electrochem. Soc. 171 (2024) 040520. https://doi.org/10.1149/1945-7111/ad3b77.
9. E. Möller, R. Palm, **K. Tuul**, M. Härmas, M. Koppel, J. Aruväli, M. Külaviir, E. Lust, Peat-Derived $ZnCl_2$-Activated Ultramicroporous Carbon Materials for Hydrogen Adsorption, Nanomaterials 13 (2023) 2883. https://doi.org/10.3390/nano13212883.
10. P. Ramah, R. Palm, **K. Tuul**, J. Aruväli, M. Månsson, E. Lust, Confinement of $LiAlH_4$ in a Mesoporous Carbon Black for Improved Near-Ambient Release of H_2, Reactions 4 (2023) 635–646. https://doi.org/10.3390/reactions4040035.
11. **K. Tuul**, R. Palm, J. Aruväli, E. Lust, Dehydrogenation and low-pressure hydrogenation properties of $NaAlH_4$ confined in mesoporous carbon black for hydrogen storage, International Journal of Hydrogen Energy 48 (2023) 19646–19656. https://doi.org/10.1016/j.ijhydene.2023.01.358.
12. A. Adamson, **K. Tuul**, T. Bötticher, S. Azam, M.D.L. Garayt, M. Metzger, Improving lithium-ion cells by replacing polyethylene terephthalate jellyroll tape, Nat. Mater. 22 (2023) 1380–1386. https://doi.org/10.1038/s41563-023-01673-3.

13. T. Taskovic, A. Adamson, A. Clarke, E.D. Alter, A. Eldesoky, K.L. Gering, **K. Tuul**, J.R. Dahn, Alkyl Dicarbonates, Common Electrolyte Degradation Products, Can Enable Long-Lived Li-Ion Cells at High Temperatures, J. Electrochem. Soc. 170 (2023) 090527. https://doi.org/10.1149/1945-7111/acf886.
14. J. Nerut, P. Teppor, R. Palm, R. Jäger, T. Thomberg, **K. Tuul**, M. Koppel, J. Aruväli, A. Kikas, J. Mondal, V. Iakimov, E. Lust, Characterisation of Novel Nitrogen Doped Reduced Graphene Oxide, ECS Trans. 108 (2022) 99. https://doi.org/10.1149/10807.0099ecst.
15. R. Palm, **K. Tuul**, F. Elson, E. Nocerino, O.K. Forslund, T.C. Hansen, J. Aruväli, M. Månsson, In situ neutron diffraction of $NaAlD_4$/carbon black composites during decomposition/deuteration cycles and the effect of carbon on phase segregation, International Journal of Hydrogen Energy 47 (2022) 34195–34204. https://doi.org/10.1016/j.ijhydene.2022.08.019.
16. R. Palm, R. Härmas, E. Härk, B. Kent, H. Kurig, M. Koppel, M. Russina, I. Tallo, T. Romann, J. Mata, **K. Tuul**, E. Lust, Study of the structural curvature in Mo_2C derived carbons with contrast matched small-angle neutron scattering, Carbon 171 (2021) 695–703. https://doi.org/10.1016/j.carbon.2020.09.070.
17. **K. Tuul**, R. Palm, Influence of Nanoconfinement on the Hydrogen Release Processes from Sodium Alanate, Reactions 2 (2021) 1–9. https://doi.org/10.3390/reactions2010001.

Konverentsid, teesid ja ettekanded:

1. K. Tuul, "Impact of Longterm Cycling at 85 and 100 °C on Li-ion Battery Cells with Liquid Electrolyte," stendiettekanne konverentsil *International Battery Materials Association Annual Meeting 2024*, Halifax, Kanada, 12. septembril 2024.
2. K. Tuul, "High-temperature challenges for Li-ion batteries in surgical instruments," suuline ettekanne suvekoolis *International Summer School and Workshops on "Medical Physics,"* Voore, Eesti, 30. juunil, 2024.
3. K. Tuul, "Limitations of Li-ion Pouch Cells for Accelerated Testing and Long-Lifetime Cells," stendiettekanne konverentsil *International Meeting on Lithium Batteries*, Hong Kong, 18. juunil, 2024.
4. K. Tuul, "In Situ Study of $NaAlH_4$ Confinement in Mesoporous Carbon Black for Hydrogen Storage," stendiettekanne 8ndal Läänemere maade elektrokeemia konverentsil, Tartu, Eesti, 14. aprillil, 2024.
5. K. Tuul, "Can One Project Cell Lifetime Using Wide Temperature Range Ultra-High Precision Coulometry?," suuline ettekanne konverentsil *244th ECS Meeting*, Göteborg, Rootsi, 12. oktoobril, 2023.
6. K. Tuul, "Enhanced hydrogen storage properties of $NaAlH_4$ confined in carbon black," suuline ettekanne virtuaalkonverentsil *International Conference on Carbon Chemistry and Materials*, 15. novembril, 2021.

DISSERTATIONES CHIMICAE UNIVERSITATIS TARTUENSIS

1. **Toomas Tamm.** Quantum-chemical simulation of solvent effects. Tartu, 1993, 110 p.
2. **Peeter Burk.** Theoretical study of gas-phase acid-base equilibria. Tartu, 1994, 96 p.
3. **Victor Lobanov.** Quantitative structure-property relationships in large descriptor spaces. Tartu, 1995, 135 p.
4. **Vahur Mäemets.** The ^{17}O and ^{1}H nuclear magnetic resonance study of H_2O in individual solvents and its charged clusters in aqueous solutions of electrolytes. Tartu, 1997, 140 p.
5. **Andrus Metsala.** Microcanonical rate constant in nonequilibrium distribution of vibrational energy and in restricted intramolecular vibrational energy redistribution on the basis of slater's theory of unimolecular reactions. Tartu, 1997, 150 p.
6. **Uko Maran.** Quantum-mechanical study of potential energy surfaces in different environments. Tartu, 1997, 137 p.
7. **Alar Jänes.** Adsorption of organic compounds on antimony, bismuth and cadmium electrodes. Tartu, 1998, 219 p.
8. **Kaido Tammeveski.** Oxygen electroreduction on thin platinum films and the electrochemical detection of superoxide anion. Tartu, 1998, 139 p.
9. **Ivo Leito.** Studies of Brønsted acid-base equilibria in water and non-aqueous media. Tartu, 1998, 101 p.
10. **Jaan Leis.** Conformational dynamics and equilibria in amides. Tartu, 1998, 131 p.
11. **Toonika Rinken.** The modelling of amperometric biosensors based on oxidoreductases. Tartu, 2000, 108 p.
12. **Dmitri Panov.** Partially solvated Grignard reagents. Tartu, 2000, 64 p.
13. **Kaja Orupõld.** Treatment and analysis of phenolic wastewater with microorganisms. Tartu, 2000, 123 p.
14. **Jüri Ivask.** Ion Chromatographic determination of major anions and cations in polar ice core. Tartu, 2000, 85 p.
15. **Lauri Vares.** Stereoselective Synthesis of Tetrahydrofuran and Tetrahydropyran Derivatives by Use of Asymmetric Horner-Wadsworth-Emmons and Ring Closure Reactions. Tartu, 2000, 184 p.
16. **Martin Lepiku.** Kinetic aspects of dopamine D_2 receptor interactions with specific ligands. Tartu, 2000, 81 p.
17. **Katrin Sak.** Some aspects of ligand specificity of P2Y receptors. Tartu, 2000, 106 p.
18. **Vello Pällin.** The role of solvation in the formation of iotsitch complexes. Tartu, 2001, 95 p.
19. **Katrin Kollist.** Interactions between polycyclic aromatic compounds and humic substances. Tartu, 2001, 93 p.

20. **Ivar Koppel.** Quantum chemical study of acidity of strong and superstrong Brønsted acids. Tartu, 2001, 104 p.
21. **Viljar Pihl.** The study of the substituent and solvent effects on the acidity of OH and CH acids. Tartu, 2001, 132 p.
22. **Natalia Palm.** Specification of the minimum, sufficient and significant set of descriptors for general description of solvent effects. Tartu, 2001, 134 p.
23. **Sulev Sild.** QSPR/QSAR approaches for complex molecular systems. Tartu, 2001, 134 p.
24. **Ruslan Petrukhin.** Industrial applications of the quantitative structure-property relationships. Tartu, 2001, 162 p.
25. **Boris V. Rogovoy.** Synthesis of (benzotriazolyl)carboximidamides and their application in relations with *N*- and *S*-nucleophyles. Tartu, 2002, 84 p.
26. **Koit Herodes.** Solvent effects on UV-vis absorption spectra of some solvatochromic substances in binary solvent mixtures: the preferential solvation model. Tartu, 2002, 102 p.
27. **Anti Perkson.** Synthesis and characterisation of nanostructured carbon. Tartu, 2002, 152 p.
28. **Ivari Kaljurand.** Self-consistent acidity scales of neutral and cationic Brønsted acids in acetonitrile and tetrahydrofuran. Tartu, 2003, 108 p.
29. **Karmen Lust.** Adsorption of anions on bismuth single crystal electrodes. Tartu, 2003, 128 p.
30. **Mare Piirsalu.** Substituent, temperature and solvent effects on the alkaline hydrolysis of substituted phenyl and alkyl esters of benzoic acid. Tartu, 2003, 156 p.
31. **Meeri Sassian.** Reactions of partially solvated Grignard reagents. Tartu, 2003, 78 p.
32. **Tarmo Tamm.** Quantum chemical modelling of polypyrrole. Tartu, 2003. 100 p.
33. **Erik Teinemaa.** The environmental fate of the particulate matter and organic pollutants from an oil shale power plant. Tartu, 2003. 102 p.
34. **Jaana Tammiku-Taul.** Quantum chemical study of the properties of Grignard reagents. Tartu, 2003. 120 p.
35. **Andre Lomaka.** Biomedical applications of predictive computational chemistry. Tartu, 2003. 132 p.
36. **Kostyantyn Kirichenko.** Benzotriazole – Mediated Carbon–Carbon Bond Formation. Tartu, 2003. 132 p.
37. **Gunnar Nurk.** Adsorption kinetics of some organic compounds on bismuth single crystal electrodes. Tartu, 2003, 170 p.
38. **Mati Arulepp.** Electrochemical characteristics of porous carbon materials and electrical double layer capacitors. Tartu, 2003, 196 p.
39. **Dan Cornel Fara.** QSPR modeling of complexation and distribution of organic compounds. Tartu, 2004, 126 p.
40. **Riina Mahlapuu.** Signalling of galanin and amyloid precursor protein through adenylate cyclase. Tartu, 2004, 124 p.

41. **Mihkel Kerikmäe.** Some luminescent materials for dosimetric applications and physical research. Tartu, 2004, 143 p.
42. **Jaanus Kruusma.** Determination of some important trace metal ions in human blood. Tartu, 2004, 115 p.
43. **Urmas Johanson.** Investigations of the electrochemical properties of polypyrrole modified electrodes. Tartu, 2004, 91 p.
44. **Kaido Sillar.** Computational study of the acid sites in zeolite ZSM-5. Tartu, 2004, 80 p.
45. **Aldo Oras.** Kinetic aspects of dATPαS interaction with $P2Y_1$ receptor. Tartu, 2004, 75 p.
46. **Erik Mölder.** Measurement of the oxygen mass transfer through the air-water interface. Tartu, 2005, 73 p.
47. **Thomas Thomberg.** The kinetics of electroreduction of peroxodisulfate anion on cadmium (0001) single crystal electrode. Tartu, 2005, 95 p.
48. **Olavi Loog.** Aspects of condensations of carbonyl compounds and their imine analogues. Tartu, 2005, 83 p.
49. **Siim Salmar.** Effect of ultrasound on ester hydrolysis in aqueous ethanol. Tartu, 2006, 73 p.
50. **Ain Uustare.** Modulation of signal transduction of heptahelical receptors by other receptors and G proteins. Tartu, 2006, 121 p.
51. **Sergei Yurchenko.** Determination of some carcinogenic contaminants in food. Tartu, 2006, 143 p.
52. **Kaido Tämm.** QSPR modeling of some properties of organic compounds. Tartu, 2006, 67 p.
53. **Olga Tšubrik.** New methods in the synthesis of multisubstituted hydrazines. Tartu. 2006, 183 p.
54. **Lilli Sooväli.** Spectrophotometric measurements and their uncertainty in chemical analysis and dissociation constant measurements. Tartu, 2006, 125 p.
55. **Eve Koort.** Uncertainty estimation of potentiometrically measured ph and pK_a values. Tartu, 2006, 139 p.
56. **Sergei Kopanchuk.** Regulation of ligand binding to melanocortin receptor subtypes. Tartu, 2006, 119 p.
57. **Silvar Kallip.** Surface structure of some bismuth and antimony single crystal electrodes. Tartu, 2006, 107 p.
58. **Kristjan Saal.** Surface silanization and its application in biomolecule coupling. Tartu, 2006, 77 p.
59. **Tanel Tätte.** High viscosity $Sn(OBu)_4$ oligomeric concentrates and their applications in technology. Tartu, 2006, 91 p.
60. **Dimitar Atanasov Dobchev**. Robust QSAR methods for the prediction of properties from molecular structure. Tartu, 2006, 118 p.
61. **Hannes Hagu**. Impact of ultrasound on hydrophobic interactions in solutions. Tartu, 2007, 81 p.
62. **Rutha Jäger.** Electroreduction of peroxodisulfate anion on bismuth electrodes. Tartu, 2007, 142 p.

63. **Kaido Viht.** Immobilizable bisubstrate-analogue inhibitors of basophilic protein kinases: development and application in biosensors. Tartu, 2007, 88 p.
64. **Eva-Ingrid Rõõm.** Acid-base equilibria in nonpolar media. Tartu, 2007, 156 p.
65. **Sven Tamp.** DFT study of the cesium cation containing complexes relevant to the cesium cation binding by the humic acids. Tartu, 2007, 102 p.
66. **Jaak Nerut.** Electroreduction of hexacyanoferrate(III) anion on Cadmium (0001) single crystal electrode. Tartu, 2007, 180 p.
67. **Lauri Jalukse.** Measurement uncertainty estimation in amperometric dissolved oxygen concentration measurement. Tartu, 2007, 112 p.
68. **Aime Lust.** Charge state of dopants and ordered clusters formation in CaF_2:Mn and CaF_2:Eu luminophors. Tartu, 2007, 100 p.
69. **Iiris Kahn**. Quantitative Structure-Activity Relationships of environmentally relevant properties. Tartu, 2007, 98 p.
70. **Mari Reinik.** Nitrates, nitrites, N-nitrosamines and polycyclic aromatic hydrocarbons in food: analytical methods, occurrence and dietary intake. Tartu, 2007, 172 p.
71. **Heili Kasuk.** Thermodynamic parameters and adsorption kinetics of organic compounds forming the compact adsorption layer at Bi single crystal electrodes. Tartu, 2007, 212 p.
72. **Erki Enkvist.** Synthesis of adenosine-peptide conjugates for biological applications. Tartu, 2007, 114 p.
73. **Svetoslav Hristov Slavov**. Biomedical applications of the QSAR approach. Tartu, 2007, 146 p.
74. **Eneli Härk.** Electroreduction of complex cations on electrochemically polished Bi(*hkl*) single crystal electrodes. Tartu, 2008, 158 p.
75. **Priit Möller.** Electrochemical characteristics of some cathodes for medium temperature solid oxide fuel cells, synthesized by solid state reaction technique. Tartu, 2008, 90 p.
76. **Signe Viggor.** Impact of biochemical parameters of genetically different pseudomonads at the degradation of phenolic compounds. Tartu, 2008, 122 p.
77. **Ave Sarapuu.** Electrochemical reduction of oxygen on quinone-modified carbon electrodes and on thin films of platinum and gold. Tartu, 2008, 134 p.
78. **Agnes Kütt.** Studies of acid-base equilibria in non-aqueous media. Tartu, 2008, 198 p.
79. **Rouvim Kadis.** Evaluation of measurement uncertainty in analytical chemistry: related concepts and some points of misinterpretation. Tartu, 2008, 118 p.
80. **Valter Reedo.** Elaboration of IVB group metal oxide structures and their possible applications. Tartu, 2008, 98 p.
81. **Aleksei Kuznetsov.** Allosteric effects in reactions catalyzed by the cAMP-dependent protein kinase catalytic subunit. Tartu, 2009, 133 p.

82. **Aleksei Bredihhin.** Use of mono- and polyanions in the synthesis of multisubstituted hydrazine derivatives. Tartu, 2009, 105 p.
83. **Anu Ploom.** Quantitative structure-reactivity analysis in organosilicon chemistry. Tartu, 2009, 99 p.
84. **Argo Vonk.** Determination of adenosine A_{2A}- and dopamine D_1 receptor-specific modulation of adenylate cyclase activity in rat striatum. Tartu, 2009, 129 p.
85. **Indrek Kivi.** Synthesis and electrochemical characterization of porous cathode materials for intermediate temperature solid oxide fuel cells. Tartu, 2009, 177 p.
86. **Jaanus Eskusson.** Synthesis and characterisation of diamond-like carbon thin films prepared by pulsed laser deposition method. Tartu, 2009, 117 p.
87. **Marko Lätt.** Carbide derived microporous carbon and electrical double layer capacitors. Tartu, 2009, 107 p.
88. **Vladimir Stepanov.** Slow conformational changes in dopamine transporter interaction with its ligands. Tartu, 2009, 103 p.
89. **Aleksander Trummal.** Computational Study of Structural and Solvent Effects on Acidities of Some Brønsted Acids. Tartu, 2009, 103 p.
90. **Eerold Vellemäe.** Applications of mischmetal in organic synthesis. Tartu, 2009, 93 p.
91. **Sven Parkel.** Ligand binding to 5-HT_{1A} receptors and its regulation by Mg^{2+} and Mn^{2+}. Tartu, 2010, 99 p.
92. **Signe Vahur.** Expanding the possibilities of ATR-FT-IR spectroscopy in determination of inorganic pigments. Tartu, 2010, 184 p.
93. **Tavo Romann**. Preparation and surface modification of bismuth thin film, porous, and microelectrodes. Tartu, 2010, 155 p.
94. **Nadežda Aleksejeva.** Electrocatalytic reduction of oxygen on carbon nanotube-based nanocomposite materials. Tartu, 2010, 147 p.
95. **Marko Kullapere.** Electrochemical properties of glassy carbon, nickel and gold electrodes modified with aryl groups. Tartu, 2010, 233 p.
96. **Liis Siinor.** Adsorption kinetics of ions at Bi single crystal planes from aqueous electrolyte solutions and room-temperature ionic liquids. Tartu, 2010, 101 p.
97. **Angela Vaasa.** Development of fluorescence-based kinetic and binding assays for characterization of protein kinases and their inhibitors. Tartu 2010, 101 p.
98. **Indrek Tulp.** Multivariate analysis of chemical and biological properties. Tartu 2010, 105 p.
99. **Aare Selberg.** Evaluation of environmental quality in Northern Estonia by the analysis of leachate. Tartu 2010, 117 p.
100. **Darja Lavõgina.** Development of protein kinase inhibitors based on adenosine analogue-oligoarginine conjugates. Tartu 2010, 248 p.
101. **Laura Herm.** Biochemistry of dopamine D_2 receptors and its association with motivated behaviour. Tartu 2010, 156 p.

102. **Terje Raudsepp.** Influence of dopant anions on the electrochemical properties of polypyrrole films. Tartu 2010, 112 p.
103. **Margus Marandi.** Electroformation of Polypyrrole Films: *In-situ* AFM and STM Study. Tartu 2011, 116 p.
104. **Kairi Kivirand.** Diamine oxidase-based biosensors: construction and working principles. Tartu, 2011, 140 p.
105. **Anneli Kruve.** Matrix effects in liquid-chromatography electrospray mass-spectrometry. Tartu, 2011, 156 p.
106. **Gary Urb.** Assessment of environmental impact of oil shale fly ash from PF and CFB combustion. Tartu, 2011, 108 p.
107. **Nikita Oskolkov.** A novel strategy for peptide-mediated cellular delivery and induction of endosomal escape. Tartu, 2011, 106 p.
108. **Dana Martin.** The QSPR/QSAR approach for the prediction of properties of fullerene derivatives. Tartu, 2011, 98 p.
109. **Säde Viirlaid.** Novel glutathione analogues and their antioxidant activity. Tartu, 2011, 106 p.
110. **Ülis Sõukand.** Simultaneous adsorption of Cd^{2+}, Ni^{2+}, and Pb^{2+} on peat. Tartu, 2011, 124 p.
111. **Lauri Lipping.** The acidity of strong and superstrong Brønsted acids, an outreach for the "limits of growth": a quantum chemical study. Tartu, 2011, 124 p.
112. **Heisi Kurig.** Electrical double-layer capacitors based on ionic liquids as electrolytes. Tartu, 2011, 146 p.
113. **Marje Kasari.** Bisubstrate luminescent probes, optical sensors and affinity adsorbents for measurement of active protein kinases in biological samples. Tartu, 2012, 126 p.
114. **Kalev Takkis.** Virtual screening of chemical databases for bioactive molecules. Tartu, 2012, 122 p.
115. **Ksenija Kisseljova**. Synthesis of aza-β^3-amino acid containing peptides and kinetic study of their phosphorylation by protein kinase A. Tartu, 2012, 104 p.
116. **Riin Rebane.** Advanced method development strategy for derivatization LC/ESI/MS. Tartu, 2012, 184 p.
117. **Vladislav Ivaništšev.** Double layer structure and adsorption kinetics of ions at metal electrodes in room temperature ionic liquids. Tartu, 2012, 128 p.
118. **Irja Helm.** High accuracy gravimetric Winkler method for determination of dissolved oxygen. Tartu, 2012, 139 p.
119. **Karin Kipper.** Fluoroalcohols as Components of LC-ESI-MS Eluents: Usage and Applications. Tartu, 2012, 164 p.
120. **Arno Ratas.** Energy storage and transfer in dosimetric luminescent materials. Tartu, 2012, 163 p.
121. **Reet Reinart-Okugbeni**. Assay systems for characterisation of subtype-selective binding and functional activity of ligands on dopamine receptors. Tartu, 2012, 159 p.

122. **Lauri Sikk.** Computational study of the Sonogashira cross-coupling reaction. Tartu, 2012, 81 p.
123. **Karita Raudkivi.** Neurochemical studies on inter-individual differences in affect-related behaviour of the laboratory rat. Tartu, 2012, 161 p.
124. **Indrek Saar.** Design of GalR2 subtype specific ligands: their role in depression-like behavior and feeding regulation. Tartu, 2013, 126 p.
125. **Ann Laheäär.** Electrochemical characterization of alkali metal salt based non-aqueous electrolytes for supercapacitors. Tartu, 2013, 127 p.
126. **Kerli Tõnurist.** Influence of electrospun separator materials properties on electrochemical performance of electrical double-layer capacitors. Tartu, 2013, 147 p.
127. **Kaija Põhako-Esko.** Novel organic and inorganic ionogels: preparation and characterization. Tartu, 2013, 124 p.
128. **Ivar Kruusenberg.** Electroreduction of oxygen on carbon nanomaterial-based catalysts. Tartu, 2013, 191 p.
129. **Sander Piiskop.** Kinetic effects of ultrasound in aqueous acetonitrile solutions. Tartu, 2013, 95 p.
130. **Ilona Faustova**. Regulatory role of L-type pyruvate kinase N-terminal domain. Tartu, 2013, 109 p.
131. **Kadi Tamm.** Synthesis and characterization of the micro-mesoporous anode materials and testing of the medium temperature solid oxide fuel cell single cells. Tartu, 2013, 138 p.
132. **Iva Bozhidarova Stoyanova-Slavova.** Validation of QSAR/QSPR for regulatory purposes. Tartu, 2013, 109 p.
133. **Vitali Grozovski**. Adsorption of organic molecules at single crystal electrodes studied by *in situ* STM method. Tartu, 2014, 146 p.
134. **Santa Veikšina**. Development of assay systems for characterisation of ligand binding properties to melanocortin 4 receptors. Tartu, 2014, 151 p.
135. **Jüri Liiv.** PVDF (polyvinylidene difluoride) as material for active element of twisting-ball displays. Tartu, 2014, 111 p.
136. **Kersti Vaarmets.** Electrochemical and physical characterization of pristine and activated molybdenum carbide-derived carbon electrodes for the oxygen electroreduction reaction. Tartu, 2014, 131 p.
137. **Lauri Tõntson**. Regulation of G-protein subtypes by receptors, guanine nucleotides and Mn^{2+}. Tartu, 2014, 105 p.
138. **Aiko Adamson.** Properties of amine-boranes and phosphorus analogues in the gas phase. Tartu, 2014, 78 p.
139. **Elo Kibena**. Electrochemical grafting of glassy carbon, gold, highly oriented pyrolytic graphite and chemical vapour deposition-grown graphene electrodes by diazonium reduction method. Tartu, 2014, 184 p.
140. **Teemu Näykki.** Novel Tools for Water Quality Monitoring – From Field to Laboratory. Tartu, 2014, 202 p.
141. **Karl Kaupmees.** Acidity and basicity in non-aqueous media: importance of solvent properties and purity. Tartu, 2014, 128 p.

142. **Oleg Lebedev**. Hydrazine polyanions: different strategies in the synthesis of heterocycles. Tartu, 2015, 118 p.
143. **Geven Piir.** Environmental risk assessment of chemicals using QSAR methods. Tartu, 2015, 123 p.
144. **Olga Mazina.** Development and application of the biosensor assay for measurements of cyclic adenosine monophosphate in studies of G protein-coupled receptor signalinga. Tartu, 2015, 116 p.
145. **Sandip Ashokrao Kadam.** Anion receptors: synthesis and accurate binding measurements. Tartu, 2015, 116 p.
146. **Indrek Tallo.** Synthesis and characterization of new micro-mesoporous carbide derived carbon materials for high energy and power density electrical double layer capacitors. Tartu, 2015, 148 p.
147. **Heiki Erikson.** Electrochemical reduction of oxygen on nanostructured palladium and gold catalysts. Tartu, 2015, 204 p.
148. **Erik Anderson.** *In situ* Scanning Tunnelling Microscopy studies of the interfacial structure between Bi(111) electrode and a room temperature ionic liquid. Tartu, 2015, 118 p.
149. **Girinath G. Pillai.** Computational Modelling of Diverse Chemical, Biochemical and Biomedical Properties. Tartu, 2015, 140 p.
150. **Piret Pikma.** Interfacial structure and adsorption of organic compounds at Cd(0001) and Sb(111) electrodes from ionic liquid and aqueous electrolytes: an *in situ* STM study. Tartu, 2015, 126 p.
151. **Ganesh babu Manoharan.** Combining chemical and genetic approaches for photoluminescence assays of protein kinases. Tartu, 2016, 126 p.
152. **Carolin Siimenson**. Electrochemical characterization of halide ion adsorption from liquid mixtures at Bi(111) and pyrolytic graphite electrode surface. Tartu, 2016, 110 p.
153. **Asko Laaniste.** Comparison and optimisation of novel mass spectrometry ionisation sources. Tartu, 2016, 156 p.
154. **Hanno Evard.** Estimating limit of detection for mass spectrometric analysis methods. Tartu, 2016, 224 p.
155. **Kadri Ligi.** Characterization and application of protein kinase-responsive organic probes with triplet-singlet energy transfer. Tartu, 2016, 122 p.
156. **Margarita Kagan.** Biosensing penicillins' residues in milk flows. Tartu, 2016, 130 p.
157. **Marie Kriisa.** Development of protein kinase-responsive photoluminescent probes and cellular regulators of protein phosphorylation. Tartu, 2016, 106 p.
158. **Mihkel Vestli.** Ultrasonic spray pyrolysis deposited electrolyte layers for intermediate temperature solid oxide fuel cells. Tartu, 2016, 156 p.
159. **Silver Sepp**. Influence of porosity of the carbide-derived carbon on the properties of the composite electrocatalysts and characteristics of polymer electrolyte fuel cells. Tartu, 2016, 137 p.
160. **Kristjan Haav**. Quantitative relative equilibrium constant measurements in supramolecular chemistry. Tartu, 2017, 158 p.

161. **Anu Teearu**. Development of MALDI-FT-ICR-MS methodology for the analysis of resinous materials. Tartu, 2017, 205 p.
162. **Taavi Ivan**. Bifunctional inhibitors and photoluminescent probes for studies on protein complexes. Tartu, 2017, 140 p.
163. **Maarja-Liisa Oldekop**. Characterization of amino acid derivatization reagents for LC-MS analysis. Tartu, 2017, 147 p.
164. **Kristel Jukk**. Electrochemical reduction of oxygen on platinum- and palladium-based nanocatalysts. Tartu, 2017, 250 p.
165. **Siim Kukk**. Kinetic aspects of interaction between dopamine transporter and *N*-substituted nortropane derivatives. Tartu, 2017, 107 p.
166. **Birgit Viira**. Design and modelling in early drug development in targeting HIV-1 reverse transcriptase and Malaria. Tartu, 2017, 172 p.
167. **Rait Kivi**. Allostery in cAMP dependent protein kinase catalytic subunit. Tartu, 2017, 115 p.
168. **Agnes Heering**. Experimental realization and applications of the unified acidity scale. Tartu, 2017, 123 p.
169. **Delia Juronen**. Biosensing system for the rapid multiplex detection of mastitis-causing pathogens in milk. Tartu, 2018, 85 p.
170. **Hedi Rahnel.** ARC-inhibitors: from reliable biochemical assays to regulators of physiology of cells. Tartu, 2018, 176 p.
171. **Anton Ruzanov.** Computational investigation of the electrical double layer at metal–aqueous solution and metal–ionic liquid interfaces. Tartu, 2018, 129 p.
172. **Katrin Kestav.** Crystal Structure-Guided Development of Bisubstrate-Analogue Inhibitors of Mitotic Protein Kinase Haspin. Tartu, 2018, 166 p.
173. **Mihkel Ilisson.** Synthesis of novel heterocyclic hydrazine derivatives and their conjugates. Tartu, 2018, 101 p.
174. **Anni Allikalt.** Development of assay systems for studying ligand binding to dopamine receptors. Tartu, 2018, 160 p.
175. **Ove Oll.** Electrical double layer structure and energy storage characteristics of ionic liquid based capacitors. Tartu, 2018, 187 p.
176. **Rasmus Palm.** Carbon materials for energy storage applications. Tartu, 2018, 114 p.
177. **Jörgen Metsik.** Preparation and stability of poly(3,4-ethylenedioxythiophene) thin films for transparent electrode applications. Tartu, 2018, 111 p.
178. **Sofja Tšepelevitš.** Experimental studies and modeling of solute-solvent interactions. Tartu, 2018, 109 p.
179. **Märt Lõkov.** Basicity of some nitrogen, phosphorus and carbon bases in acetonitrile. Tartu, 2018, 104 p.
180. **Anton Mastitski**. Preparation of α-aza-amino acid precursors and related compounds by novel methods of reductive one-pot alkylation and direct alkylation. Tartu, 2018, 155 p.
181. **Jürgen Vahter**. Development of bisubstrate inhibitors for protein kinase CK2. Tartu, 2019, 186 p.

182. **Piia Liigand.** Expanding and improving methodology and applications of ionization efficiency measurements. Tartu, 2019, 189 p.
183. **Sigrid Selberg.** Synthesis and properties of lipophilic phosphazene-based indicator molecules. Tartu, 2019, 74 p.
184. **Jaanus Liigand.** Standard substance free quantification for LC/ESI/MS analysis based on the predicted ionization efficiencies. Tartu, 2019, 254 p.
185. **Marek Mooste.** Surface and electrochemical characterisation of aryl film and nanocomposite material modified carbon and metal-based electrodes. Tartu, 2019, 304 p.
186. **Mare Oja.** Experimental investigation and modelling of pH profiles for effective membrane permeability of drug substances. Tartu, 2019, 306 p.
187. **Sajid Hussain.** Electrochemical reduction of oxygen on supported Pt catalysts. Tartu, 2019, 220 p.
188. **Ronald Väli.** Glucose-derived hard carbon electrode materials for sodium-ion batteries. Tartu, 2019, 180 p.
189. **Ester Tee.** Analysis and development of selective synthesis methods of hierarchical micro- and mesoporous carbons. Tartu, 2019, 210 p.
190. **Martin Maide.** Influence of the microstructure and chemical composition of the fuel electrode on the electrochemical performance of reversible solid oxide fuel cell. Tartu, 2020, 144 p.
191. **Edith Viirlaid.** Biosensing Pesticides in Water Samples. Tartu, 2020, 102 p.
192. **Maike Käärik.** Nanoporous carbon: the controlled nanostructure, and structure-property relationships. Tartu, 2020, 162 p.
193. **Artur Gornischeff.** Study of ionization efficiencies for derivatized compounds in LC/ESI/MS and their application for targeted analysis. Tartu, 2020, 124 p.
194. **Reet Link.** Ligand binding, allosteric modulation and constitutive activity of melanocortin-4 receptors. Tartu, 2020, 108 p.
195. **Pilleriin Peets.** Development of instrumental methods for the analysis of textile fibres and dyes. Tartu, 2020, 150 p.
196. **Larisa Ivanova.** Design of active compounds against neurodegenerative diseases. Tartu, 2020, 152 p.
197. **Meelis Härmas.** Impact of activated carbon microstructure and porosity on electrochemical performance of electrical double-layer capacitors. Tartu, 2020, 122 p.
198. **Ruta Hecht.** Novel Eluent Additives for LC-MS Based Bioanalytical Methods. Tartu, 2020, 202 p.
199. **Max Hecht.** Advances in the Development of a Point-of-Care Mass Spectrometer Test. Tartu, 2020, 168 p.
200. **Ida Rahu.** Bromine formation in inorganic bromide/nitrate mixtures and its application for oxidative aromatic bromination. Tartu, 2020, 116 p.
201. **Sander Ratso**. Electrocatalysis of oxygen reduction on non-precious metal catalysts. Tartu, 2020, 371 p.
202. **Astrid Darnell.** Computational design of anion receptors and evaluation of host-guest binding. Tartu, 2021, 150 p.

203. **Ove Korjus.** The development of ceramic fuel electrode for solid oxide cells. Tartu, 2021, 150 p.
204. **Merit Oss.** Ionization efficiency in electrospray ionization source and its relations to compounds' physico-chemical properties. Tartu, 2021, 124 p.
205. **Madis Lüsi**. Electroreduction of oxygen on nanostructured palladium catalysts. Tartu, 2021, 180 p.
206. **Eliise Tammekivi.** Derivatization and quantitative gas-chromatographic analysis of oils. Tartu, 2021, 122 p.
207. **Simona Selberg.** Development of Small-Molecule Regulators of Epi-transcriptomic Processes. Tartu, 2021, 122 p.
208. **Olivier Etebe Nonga.** Inhibitors and photoluminescent probes for in vitro studies on protein kinases PKA and PIM. Tartu, 2021, 189 p.
209. **Riinu Härmas.** The structure and H2 diffusion in porous carbide-derived carbon particles. Tartu, 2022, 123 p.
210. **Maarja Paalo.** Synthesis and characterization of novel carbon electrodes for high power density electrochemical capacitors. Tartu, 2022, 144 p.
211. **Jinfeng Zhao.** Electrochemical characteristics of Bi(hkl) and micro-meso-porous carbon electrodes in ionic liquid based electrolytes. Tartu, 2022, 134 p.
212. **Alar Heinsaar.** Investigation of oxygen electrode materials for high-temperature solid oxide cells in natural conditions. Tartu, 2022, 120 p.
213. **Jaana Lilloja.** Transition metal and nitrogen doped nanocarbon cathode catalysts for anion exchange membrane fuel cells. Tartu, 2022, 202 p.
214. **Maris-Johanna Tahk.** Novel fluorescence-based methods for illuminating transmembrane signal transduction by G-protein coupled receptors. Tartu, 2022, 200 p.
215. **Eerik Jõgi.** Development and Applications of E. coli Immunosensor. Tartu, 2022, 103 p.
216. **Alo Rüütel.** Design principles of synthetic molecular receptors for anion-selective electrodes. Tartu, 2022, 109 p.
217. **Tanel Sõrmus.** Development of stimuli-responsive and covalent bisubstrate inhibitors of protein kinases. Tartu, 2022, 148 p.
218. **Oleg Artemchuk.** Autotrophic nitrogen removal processes for nutrient removal from sidestream and mainstream wastewater. Tartu, 2022, 115 p.
219. **Andre Leesment.** Quantitative studies of Brønsted acidity in biphasic systems and gas-phase. Tartu, 2023, 83 p.
220. **Meeli Arujõe-Sado.** Structural effects in aza-peptide bond formation reaction. Tartu, 2023, 83 p.
221. **Jonas Mart Linge.** Electrochemical reduction of oxygen on silver-based catalysts. Tartu, 2023, 269 p.
222. **Tõnis Laasfeld.** Integrating Image Analysis and Quantitative Modeling for a Holistic View of GPCR Ligand Binding Dynamics. Tartu, 2023, 226 p.
223. **Ernesto de Jesus Zapata Flores.** Derivatization Reagents used in negative mode electrospray LC-MS. Tartu, 2023, 107 p.

224. **Patrick Teppor.** Obtaining platinum-free oxygen reduction catalysts through biomass valorization: a case study of peat. Tartu, 2023, 161 p.
225. **Peeter Valk.** Methanol Oxidation on Platinum-Rare-Earth Metal Oxide Activated Catalysts. Tartu, 2023, 162 p.
226. **Shidong Chen.** Unravelling prehistoric plant exploitation in eastern Baltic: organic residue analysis of plant-based materials by multi-method approach. Tartu, 2023, 245 p.
227. **Yogesh Kumar.** M-N_4 macrocycle-based catalysts for electrocatalysis of oxygen reduction and oxygen evolution. Tartu, 2023, 224 p.
228. **Kerli Martin.** Recognition of carboxylates by synthetic receptors – from structure-affinity studies to solid-contact anion-selective electrode prototyping. Tartu, 2024, 130 p.
229. **Huy Quí Vinh Nguyen.** Development of Carbon Supported Pt–CeO_2 Catalysts for Proton Exchange Membrane Fuel Cells. Tartu, 2024, 198 p.
230. **Heigo Ers**. Adsorption and Structuring Processes at Single Crystal Electrode – Ionic Liquid Interface – Insights from Simulations and *in situ* Studies. Tartu, 2024, 137 p.
231. **Ritums Cepitis.** Modelling Structural and Geometrical Effects in Carbon Dioxide and Oxygen Electrocatalysis. Tartu, 2024, 99 p.
232. **Kaarel Kisand.** Resorcinol-derived carbon-based catalysts for polymer electrolyte fuel cell cathodes. Tartu, 2024, 205 p.
233. **Akmal Kosimov**. Template-assisted Mechanosynthesis (TAMS) for the production of bifunctional transition metal-based catalysts. Tartu, 2024, 123 p.
234. **Larissa Silva Macieli.** Derivatization-targeted LC-MS analysis of compounds containing amino group. Tartu, 2024, 157 p.
235. **Silvester Jürjo.** Separation of rare earth elements from Estonian phosphorite ore using liquid extraction followed by electrochemical reduction. Tartu, 2024, 99 p.
236. **Jan-Michael C. Cayme.** Organic-inorganic interactions in experimental and archaeological ceramics. Tartu, 2025, 156 p.
237. **Miriam Koppel.** The diffusion of H2 adsorbed in carbide-derived carbons: a quasi-elastic neutron scattering study. Tartu, 2025, 138 p.